Friedrich-Alexander-Universität
Faculty of Sciences

Master's Thesis

in Physics

Search for Periodic Neutrino Sources with KM3NeT

Hannes Warnhofer

Supervisor: PD Dr. Thomas Eberl
Erlangen Centre for Astroparticle Physics

Submission date: 29th of August 2025

Abstract

This thesis presents a search for astrophysical sources of periodic neutrino emission with the KM3NeT neutrino telescope. Periodic emission of high-energy neutrinos is expected from compact objects such as pulsars or X-ray binaries, where hadronic acceleration processes are expected to take place, fueled by the extreme conditions in the close environments of these objects. The search for periodic signals through epoch folding exploits the timing modulation to enhance the discovery potential of a possible signal and to reduce the background contamination. An analysis workflow for the usage with ARCA and ORCA data was developed, which applies an epoch folding search around a certain test frequency to events associated with a chosen source. Furthermore, an analysis framework was constructed, which allows us to evaluate the detection sensitivity by injecting simulated events that follow a periodic timing imitating the radio signal from pulsars. Two flux models were investigated: a classic power law flux for general comparison and a bounded power law flux that models the predicted fluxes from the Vela and Crab Pulsar presented in [41]. For a classical power law flux, the sensitivity strongly depends on the corresponding spectral index. For $\gamma = 2$, a sensitivity of $E^2\Phi_\nu(E_0 = 1\,\mathrm{TeV}) \approx 10^{-11}\,\mathrm{GeV\,cm^{-2}\,s^{-1}}$ was found at 1 TeV, for an analysis of events arriving from the direction of Vela over the course of 150 days, showing improvements of three orders of magnitude compared to time integrated point source analyses with KM3NeT. For the bounded flux we find that the sensitivities towards the detection of periodic signals from Crab and Vela are still much too low compared to the predicted fluxes. We estimate, that with the ARCA21 detector setup used in this analysis, observations of 25 years (71 years) are needed to achieve a 5σ detection of the predicted flux from Crab (Vela) under the assumption of the signal following the periodic emission pattern. The results show the promising improvements in signal to noise ratio, that can be expected from the analysis of a periodic signal, where the emission is confined to a narrow phase interval of the source object's rotation. If existent, the analysis of periodic neutrino signals might provide a valuable tool for studying the possible origins of high-energy cosmic neutrinos and probing the connection between compact objects and cosmic-ray production.

Contents

1 Introduction to Neutrino Astronomy

In the following chapter, the basics of neutrino astronomy are presented. Starting with a brief introduction into the description of neutrinos within the standard model of particle physics, we will explore the challenges and opportunities that neutrino astronomy offers to particle physicists and astronomers. The composition and origins of the neutrino flux measured on Earth will be discussed, highlighting the mechanisms behind the production of high-energy cosmic neutrinos. Finally, the detection mechanisms behind Cherenkov neutrino telescopes will be presented.

1.1 A Short History of Neutrino Astronomy

Neutrinos appeared first in the discussions of physicists when investigating the β-decay of nuclei back in 1914, where a continuous energy spectrum of the electron emitted in this decay was observed, which hinted towards a hidden particle being produced in this reaction together with the electron. The β-decay describes a type of nuclear decay in which a β-particle, a high-energy electron or positron, gets emitted. The underlying interaction would be described as follows:

$$\mathrm{n} \rightarrow \mathrm{p} + \mathrm{e}^- + \bar{\nu}_\mathrm{e} \tag{1.1}$$

With a proton p decaying into a neutron n, a positron e^+ and a third particle ν_e. In 1930 W. Pauli proposed the existence of a spin 1/2 particle that escapes observation. Due to the low interaction probability and the neutral electrical charge, E. Fermi gave the particle the name *neutrino*, which means "the little neutral one" in Italian, also because the neutron - how Pauli first called his hypothesized light particle - had already been discovered and named as such in the meantime by J. Chadwick in 1932 [47]. Fermi published his work about the nature of the β-decay in 1933, where he presents a theory about the electron emission from radioactive substances, built on the assumption that the electrons which are emitted from the nuclei during β-decay do not exist prior to the decay, but are created together with a neutrino, similarly to the creation of an emitted light quantum during a state change of an atom [27]. This groundbreaking approach set the basis for the development of the theory of the weak interaction and neutrino physics. In 1934 a paper was published by H. Bethe and R. Peierls, where they evaluated Fermi's theory and concluded a possible experimental detection of neutrinos through inverse β-decay. They estimated the cross section of the interaction to be so low that they concluded that it was impossible to observe neutrinos that originate from nuclear decays. Also Pauli is said to have struggled with his postulation of a seemingly non-detectable particle. However, the problem arising from the very low cross section could be solved by providing high enough neutrino fluxes and sufficiently large and massive detectors. The rise in reactor power and advancements regarding detector techniques set the path for F. Reines and C. Cowan, who were able to experimentally detect neutrinos for the first time in 1956, 26 years after Pauli first proposed its existence. The developments of high-energy particle accelerators in the late 1950s made it possible to design intense high-energy neutrino beams through the impact of a highly accelerated proton beam with a dense target and subsequent in-flight decay of pions produced in these interactions. This reaction chain was first proposed as a possible source of high-energy neutrinos in 1958. Investigations of the decay of cosmic muons showed that an electron and two neutrinos are produced in this decay:

$$\mu^- \rightarrow \mathrm{e}^- + \bar{\nu}_\mathrm{e} + \nu_\mu \tag{1.2}$$

Discussion remained whether the neutrinos produced in the beta decay (ν_e) and the muon decay (ν_μ) are the same particles or not. This was settled by an experiment conducted at the accelerator at Brookhaven National Lab in 1962, where the existence of the muon neutrino was experimentally discovered, distinguishable from the ν_e [7].

Another milestone in the history of neutrino physics was the first measurement of neutrinos emitted in fusion processes inside the Sun, named solar neutrinos, by J. Bahcall and R. Davis in 1968. However, the measurement showed a deficit compared to the predicted flux of solar neutrinos - the so-called solar neutrino problem - which was later confirmed by a number of other experiments such as SNO or Kamiokande. The setup of Kamiokande, which started operation in 1983, allowed for a directional measurement of the detected neutrinos, making it the first neutrino telescope in the sense of being able to measure astrophysical neutrino emission and reconstructing the source direction of the neutrinos. In 1987 it was among other neutrino detectors that measured an increased flux of neutrinos with energies between 10 and 50 MeV during the supernova event SN1987A, making it the first detection of neutrinos associated with an astrophysical source besides the Sun [62]. The so-called solar neutrino problem was later explained through the process of neutrino oscillation of the neutrinos on their way from the Sun to Earth. In 1998 this phenomenon was experimentally confirmed by the Super-K experiment looking at the directional dependence of the flux of neutrinos produced in cosmic-ray interactions in the atmosphere. The proof for neutrino oscillation accounting for the lack of detected solar neutrinos could finally be provided by experiments at the Sudbury Neutrino Observatory in 2002 [7].

We will now shift our focus more towards the recent history of neutrino astronomy, where developments in the field of high-volume Cherenkov detectors opened the door towards the study of high-energy cosmic neutrinos. A major breakthrough was the detection of the first cosmic neutrinos exceeding 1 PeV energies at the IceCube neutrino telescope in 2013. In the same year the observatory at the South Pole also found evidence for an extragalactic diffuse neutrino flux similar to the diffuse background that can be observed in gamma rays and later on managed to identify the first object associated with the origin of high-energy astrophysical neutrinos. In 2017 a neutrino with an estimated energy of 290 TeV was detected coming from the direction of the blazar TXS 0506+056, which was in a flaring state during this time producing also excessive emission of gamma rays. Analyses showed that this is most likely not a coincidence, connecting the neutrino event with the higher activity in the gamma rays, establishing neutrinos as a tool in multi-messenger astrophysics [34]. In parallel, the ANTARES detector in the Mediterranean Sea, operational from 2006 to 2022, offered complementary observations from the Northern Hemisphere and demonstrated the viability of deep-sea neutrino telescopes, setting the path for experiments such as KM3NeT [5]. Looking at the connection between high-energy neutrino astronomy and fundamental particle physics research we can see that the approach of investigating the nature of neutrino oscillations by looking at the flux distributions of atmospheric neutrinos after traversing Earth is also pursued by modern-day neutrino experiments such as ORCA, KM3NeT's detector dedicated to the study of neutrino oscillation and the neutrino mass ordering [18]. Most recently, in February 2023, KM3NeT's ARCA detector observed a neutrino interaction with the neutrino's energy estimated to be around 220 PeV, the highest-energy neutrino ever detected up to now (August 2025). The origin of the event called KM3-230312A could not yet be associated with a known cosmic source, but it demonstrates the ability of KM3NeT/ARCA to probe unprecedented energy scales already during the construction phase with only a small part of the planned detection units installed [19].

1.2 Neutrinos in the Standard Model

The subject of particle physics deals with the description, detection, and understanding of the fundamental particles of matter and the interactions between them. Basically, the idea is to reduce the question "What is stuff and what is it doing?" to the most elementary level. The framework in which most modern particle physics takes place is the Standard Model of Particle Physics, often simply called Standard Model, a theory that describes the fundamental particles and interactions with the mathematical formalisms of quantum field theory. The basic concept is the following. There are 24 fundamental particles making up the constituents of matter, the so-called fermions, which interact through the exchange of mediator particles called bosons. Although the theory fails to describe gravity in the context of elementary particles, it covers the other three known fundamental forces and allows for measurements and predictions with astonishing precision [44]. In the following, a short overview about the Standard Model will be given, laying the foundation of understanding how neutrinos are produced and detected. Figure 1.1 shows a summary of all particles involved in the model description.

The most familiar to human experience through its long range and macroscopic effects is the **electromagnetic force**. It acts on particles based on a property called electrical charge, which characterizes the interaction strength of the force. It is mediated through the photon, which we can not only detect with our eyes but is often the final mediator particle detected in experiments, highlighting the importance of a precise description of electromagnetic interactions at the elementary level for modern particle physics. The other two fundamental forces are limited to a much shorter range and are therefore restricted to interactions between particles on a much smaller length scale. They come into play when looking at processes inside atomic nuclei and high-energy interactions of particles. The **strong force** acts via the coupling of gluons, similar to the photon coupling in the electromagnetic force and depends on the color charge of a particle. The **weak force** acts through the exchange of W^+-, W^-- and Z-bosons that couple to a property called flavor, which all elementary particles inherit [44].

Fermions, the elementary constituents of matter, can be grouped together according to the forces they are interacting with, firstly separating them into quarks and leptons. Besides the electromagnetic and weak force, quarks also take part in strong force interactions. They can be grouped into three generations of two quark types each, where higher generational quarks have higher masses and tend to decay into lower generational ones. The two quarks within each generation have an electrical charge of $+2/3$ (up, charm and top quarks) and $-1/3$ (down, strange and bottom quarks). Besides up and down quarks binding into stable protons and neutrons that make up most of the matter in our universe, quarks can form other bound states of two ("mesons") or three ("baryons") particles that can be stable long enough to become important for interactions in the high-energy regime of neutrino astronomy, which we will see in section 1.4. Leptons on the other hand do not carry a color charge and only interact through electromagnetism or the weak force, which have been found to be two effects of the same theory that emerges to a single description of a unified electroweak force in high enough energy conditions. Leptons also appear in three generations, with each one consisting of one charged lepton with electrical charge of 1 and a corresponding neutrino with no electrical charge. The charged lepton of the first generation is the good old electron, which forms the universe's stable matter together with protons and neutrons in bound atomic states. Besides being bound in atoms, electrons can also exist freely and interact with other particles when doing so. The higher generational fermions are the muon and the tau, which subsequently decay into the lower generational charged fermions if they do not interact before that. The theory of the Standard

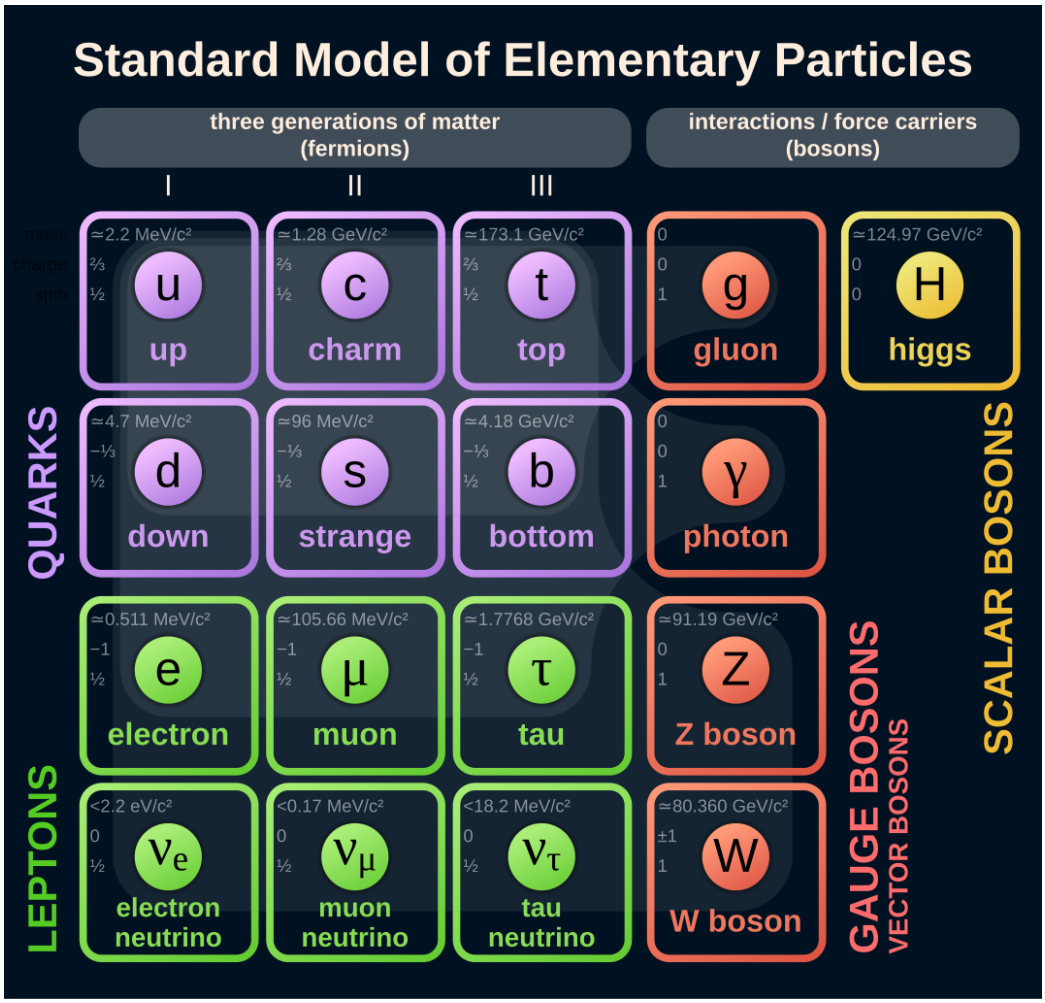

Figure 1.1: Overview about the elementary particles described within the Standard Model. The light shading in the background shows which fermions couple to which gauge bosons and therefore interact via the corresponding force these bosons mediate. Image taken from [21]

Model describes the weak interaction in such a way that the amount of leptons within a certain generation is conserved, meaning that the decay of a muon into an electron will for example leave a muon neutrino in the process to keep the muon number at 1 and also an electron antineutrino is created which leaves the overall number of electron leptons at 0. We have now seen, that there are 6 types of quarks, 3 charged leptons and 3 neutrinos. For the full picture we have to consider another important concept of particle physics, namely the existence of antiparticles. For each fermion f there exists a corresponding antiparticle $\bar{f}$ with inverted charge but otherwise unchanged properties [44]. Looking at neutrinos having no charge, one could think of where the difference between a neutrino ν and an antineutrino $\bar{\nu}$ actually lies and indeed this question is still subject of ongoing research [46].

In summary we can say that neutrinos are described as 1/2 spin particles with no electrical charge that interact with all other elementary particles via the weak force through the exchange of a W^+-, W^-- or Z-boson and do not interact through any other forces (besides gravity). They have very small interaction cross sections and very low masses, which were long thought to be zero. Neutrinos exist in three different flavor: the electron neutrino ν_e, the muon neutrino ν_μ and the tau neutrino ν_τ. For each one there exists a corresponding antiparticle $\bar{\nu}_e$, $\bar{\nu}_\mu$ or $\bar{\nu}_\tau$.

Neutrinos have the property that the mass state in which the neutrino is moving once being produced is not the same as the flavor state that takes part in the weak interaction processes, but each flavor state is a superposition of the three mass eigenstates and vice versa. While propagating through space and matter, the probability of the flavor in which an initially created electron neutrino will interact and be detected changes. After certain distances of traveling, an initially produced electron neutrino is more likely to be detected as a muon neutrino, depending on the matter it traversed [46]. This phenomenon is known as neutrino oscillation and is currently studied for example with KM3NeT's ORCA detector.

1.3 Neutrinos as Messenger Particles

The very special properties of neutrinos in the context of neutrino astronomy are their neutral electrical charge and their incredibly small mass and interaction cross sections. The cross section of 1 MeV electron antineutrinos interacting with atomic nuclei is around $\sigma \approx 10^{-44}\,\mathrm{cm}^2$, which means that on average only one out of 10^{11} of such neutrinos interacts at some point when traversing Earth's diameter. On the one hand, this makes the detection of neutrinos difficult, because the low interaction cross section means that one needs very high detection volumes to detect enough interactions from the low flux of cosmic neutrinos. However, on the other hand, this could provide detailed insights into cosmic processes, because neutrinos travel unhindered towards our detectors without experiencing scattering, possibly able to reveal mechanisms that are hidden for other messengers like photons or cosmic-rays [53]. Photons may be absorbed by interactions with matter and the charged cosmic-rays get deflected by galactic magnetic fields, removing directional information about where they were originating from. This is not the case for the uncharged neutrinos [31]. Figure 1.2 shows a simple visualization of this idea.

In addition, neutrinos of all energy ranges can in principle arrive at Earth without attenuation, contrary to high energetic electromagnetic radiation or accelerated charged particles, which for high enough energies scatter with background photons from the cosmic microwave background or other low-energy background photons produced by blackbody radiation. These properties make neutrinos excellent messenger particles for astronomy, making it possible to provide deep insights into the mechanisms at the core of astrophysical objects. Furthermore, cosmic processes could provide high-energy neutrinos for studying the Standard Model and physics beyond, if one is able to detect them efficiently enough [31].

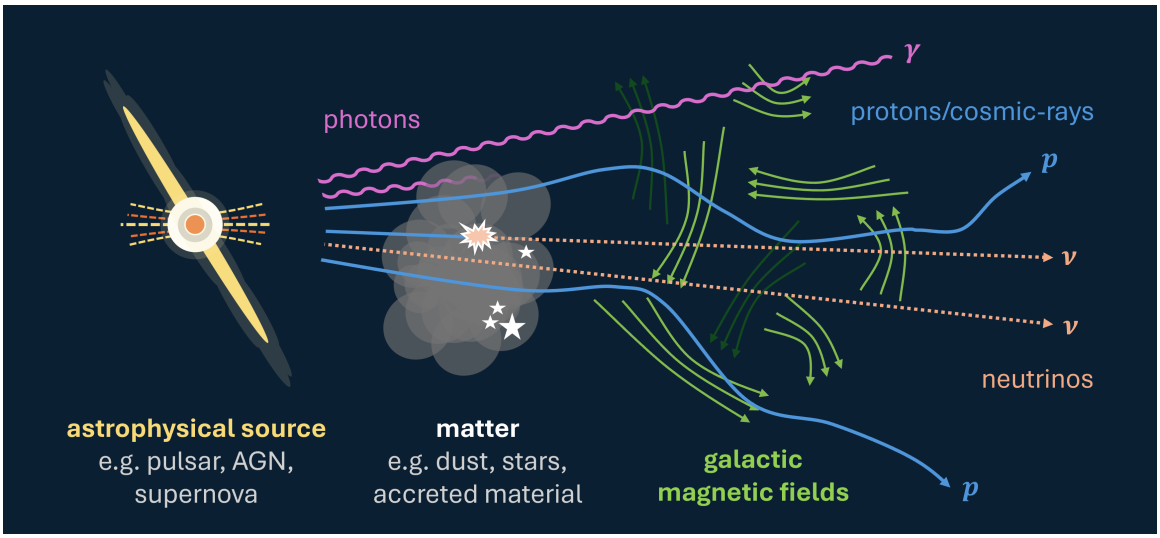

Figure 1.2: Schematic illustration of how different cosmic messengers (neutrinos ν, photons γ, and protons/cosmic-rays p) propagate from an astrophysical source through surrounding matter and galactic magnetic fields. While photons can be absorbed or scattered by intervening dust and gas, and charged particles are deflected by magnetic fields, neutrinos travel in straight lines without interaction, preserving information about their origin.

1.4 Astrophysical Neutrino Flux

Now that an introduction into the fundamental framework in which neutrinos are treated was presented, we will dive deeper into the astrophysical neutrino emissions and the underlying interactions. When aiming for the study of neutrinos from astrophysical objects, one has to be aware of all the possible contributions to the overall flux of neutrinos that arrive at the detector. The most dominant constituents are neutrinos originating from the Sun, neutrinos coming from distant supernova events and neutrinos produced in cosmic-ray interactions in the atmosphere, which in combination present a high background rate of neutrinos for the comparably low expected flux of high energetic cosmic neutrinos. In the following, the origin and characteristics of each of the flux constituents will be presented.

1.4.1 Solar Neutrinos

The neutrinos emitted from the Sun (and obviously in a similar manner by all other stars) are somewhat byproducts of the nuclear reactions that fuel the energy production in their interior. The hydrogen burning subsequently transforms four protons into helium under the emission of photons that ultimately radiate energy away from the Sun. The end products of this reaction chain are the following:

$$4\mathrm{p} \rightarrow {}^{4}\mathrm{He} + 2\mathrm{e}^{+} + 2\nu_{\mathrm{e}} + Q \tag{1.3}$$

One can see that with each new helium atom being formed, two positrons and two electron neutrinos are produced. In addition, the energy $Q = 26.73\,\mathrm{MeV}$ is released in the form of photons. Figure

1.3a shows the predicted spectrum of solar neutrinos from each underlying interaction and we will now have a short look at the individual components. According to the standard solar model, the most important reaction, contributing to around 92 % of the neutrinos produced in the Sun, is the pp-interaction chain. The first underlying interaction in hydrogen fusion of two ^{1}H atoms is the β^+-decay of a proton in the presence of another hydrogen atom, forming deuterium ^{2}H, hydrogen with an additional neutron in the nucleus [52].

$$p + p \rightarrow {}^2\mathrm{H} + \mathrm{e}^+ + \nu_\mathrm{e} \tag{1.4}$$

The second reaction providing deuterium for further interactions is the so-called pep-reaction, which again creates a deuterium atom and an electron neutrino, but with the capture of an electron instead of the emission of a positron:

$$\mathrm{p} + \mathrm{e}^- + \mathrm{p} \rightarrow {}^2\mathrm{H} + \nu_\mathrm{e} \tag{1.5}$$

Notice that this reaction is much more unlikely due to the three-particle interaction and also because the energy of the produced neutrino is much higher than for the pp-interaction. Due to the final two-particle state of this interaction, the so-called pep-neutrinos are monoenergetic, since the interacting particles are basically at rest and the dominant part of energy comes from the rest mass of the particles. Since the final deuterium atom has very little recoil nearly all of the energy difference between the initial masses and the mass of the deuterium nucleus is carried away by the produced neutrino, which therefore has a narrow energy distribution centered at 1.441 MeV.

The second largest contribution to the solar neutrino flux comes from beryllium ^{7}Be produced in $^3\mathrm{He} + {}^4\mathrm{He}$ interactions that capture a free electron:

$${}^7\mathrm{Be} + \mathrm{e}^- \rightarrow {}^7\mathrm{Li} + \nu_\mathrm{e} \tag{1.6}$$

Analogously to the pep-neutrinos, this produces a two-particle final state and therefore a more or less monoenergetic neutrino spectrum. However, the interaction can also occur with the lithium atom ending up in an exited state, which takes more energy of the reaction, leaving the emitted neutrino with less energy in around 10 % of the cases. This explains the prediction of two lines from ^{7}Be-neutrinos in the solar neutrino spectrum. If the beryllium atoms capture a proton instead of an electron, the produced boron ^{8}B atoms undergo β^+-decay, producing a positron and an electron neutrino [52]:

$${}^8\mathrm{B} \rightarrow {}^8\mathrm{Be}^* + \mathrm{e}^+ + \nu_\mathrm{e} \tag{1.7}$$

These ^{8}B-neutrinos reach much higher energies than the dominantly produced pp-, pep- and ^{7}Be-neutrinos which are only surpassed by the so-called hep-neutrinos, that are created in the proton capture of an ^{3}He isotope:

$${}^3\mathrm{He} + \mathrm{p} \rightarrow {}^4\mathrm{He} + \mathrm{e}^+ + \nu_\mathrm{e} \tag{1.8}$$

Besides the neutrinos being emitted in the pp-chain, a small part of the solar neutrino flux is provided by reactions within the CNO cycle taking place in the Sun. This reaction cycle produces a small fraction of the Sun's overall energy output through fusion processes including heavier nuclei, which contains the following three interactions that result in the production of a neutrino [52]:

$${}^{13}\mathrm{N} \rightarrow {}^{13}\mathrm{C} + \mathrm{e}^+ + \nu_\mathrm{e} \tag{1.9}$$

$${}^{15}\mathrm{O} \rightarrow {}^{15}\mathrm{N} + \mathrm{e}^+ + \nu_\mathrm{e} \tag{1.10}$$

$${}^{17}\mathrm{F} \rightarrow {}^{17}\mathrm{O} + \mathrm{e}^+ + \nu_\mathrm{e} \tag{1.11}$$

Overall, the by far dominant emission takes place in the form of pp- and ^{7}Be-neutrinos, as can also be seen in the predicted flux spectrum of the solar neutrinos shown in figure 1.3a. The ^{7}Be-neutrino flux can be estimated to be at around 0.081 times the flux of pp-neutrinos. The relative flux of pep- to pp-neutrinos is around 2.4×10^{-3}, and the hep-neutrino flux is equal to only 1.33×10^{-7} of the pp-neutrino flux. Notice that all neutrinos being produced here are electron neutrinos, but through neutrino flavor oscillations and matter effects during their propagation to the Sun's surface and then towards Earth, a relevant number of solar neutrinos will be detected at the Earth in the form of muon neutrinos [52]. Figure 1.3b shows the distribution of neutrino events coming from the Sun as measured by Borexino in 2016 together with the fitted subspectra for the neutrino components produced from the interactions presented above. Notice that the flux is partly dominated by background events from nuclear decays. When comparing figures 1.3a and 1.3b one might ask why the monoenergetic pep- and ^{7}Be-neutrinos are not measured as such and rather show broad flat spectra that fall off towards the expected monoenergetic energies. This is because the energy measured here is the one transferred to electrons in weak elastic neutrino-electron scattering, where only a fraction of the neutrino's energy is picked up and the spectrum therefore spreads out towards lower energies [4].

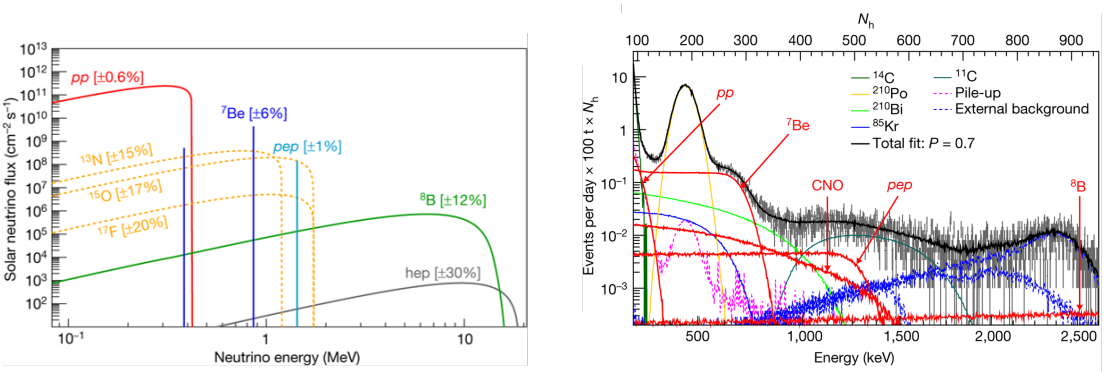

(a) (b)

Figure 1.3: Predicted spectrum of neutrinos produced inside the Sun for each process of the pp-chain and the SNO-cycle (a) and measured energy spectrum of neutrino-electron elastic scattering interactions from solar neutrinos (b); both images from [4]

In summary, we can say that the solar neutrinos can cause a high background in the energy range of a few MeV and below that in principle has to be considered when investigating astrophysical neutrino sources. However, for the analysis conducted in this work, this background will not be of importance, since the Cherenkov emission produced from the solar neutrinos with maximum energies of 15 MeV is too faint to be effectively detected by KM3NeT's detectors. Nevertheless, this highlights an important part of neutrino astronomy and shows how a better understanding of the neutrino's nature can help deepening the understanding of fusion processes inside the Sun.

1.4.2 Supernova Neutrinos

After motivating the origin and energy spectra of the neutrinos produced in the Sun, we can briefly have a look at another type of astrophysical neutrinos that have comparably low energies. For the

standard detection processes in KM3NeT's telescopes, the energies are still too low for the neutrino to be effectively measured, as is also the case for solar neutrinos. However, new approaches of instrumentalizing the telescope's detection modules might make these energy ranges accessible for possible studies in the future [20] and for completeness we will have a short look at the production mechanisms and flux characteristics of these so-called supernova neutrinos.

A core-collapse supernova is the violent end following the burning phase of a sufficiently massive star, when the remaining iron core is no longer able to provide enough outwards pressure counteracting gravity. This causes the core to further compress into a neutron star, resulting in a shock wave that causes a big part of the star's material to be ejected. More on the processes behind the formation of neutron stars will be explained in section 2.1. This generates photon luminosities comparable to that of whole galaxies for a brief period of time [51]. Even though such supernovae can produce so much light that they are visible to the human eye as newly appearing bright objects in the night sky, the photon emission makes up only 0.01 % of the total released energy. Around 99 % of it is carried away by neutrinos, mainly through the following interactions.

The main part of neutrinos from core collapse supernovae is generated in thermal processes including pair production (eq. 1.12), photo-annihilation (eq. 1.13) and nucleon-nucleon bremsstrahlung (eq. 1.14).

$$\mathrm{e}^- + \mathrm{e}^+ \rightarrow \nu + \bar{\nu} \tag{1.12}$$

$$\mathrm{e}^- + \gamma \rightarrow \mathrm{e}^- + \nu + \bar{\nu} \tag{1.13}$$

$$N + N \rightarrow N + N + \nu + \bar{\nu} \tag{1.14}$$

These processes are also thought to be present in the core of stars like the Sun, but at a much smaller scale. In addition to that, neutrinos are also produced during neutron formation through electron capture by nucleons or free protons at the early stages of core collapse [51]:

$$\mathrm{p} + \mathrm{e}^- \rightarrow n + \nu_\mathrm{e} \tag{1.15}$$

Neutrinos from supernova events are expected with energies between 1 and 50 GeV and have been detected during the supernova SN1987A by multiple experiments. As neutrino production is taking place through multiple processes that are partly bound to certain phases of the core-collapse the direct time resolution carried by neutrinos could provide extremely valuable insight for the study of supernovae in the future [51].

1.4.3 Atmospheric Neutrinos

Now that we have covered how the comparably low-energetic solar neutrinos ($E_\mathrm{max} \approx 10\,\mathrm{MeV}$) and supernova neutrinos ($E_\mathrm{max} \approx 50\,\mathrm{MeV}$) are produced, we can now enter the realm of emission that we will mostly be dealing with when it comes to the study of cosmic high-energy neutrinos. Atmospheric neutrinos provide the most abundant source of GeV neutrinos and have been and are studied extensively, lately especially due to their possibilities in revealing information about the effect of neutrino oscillation and fundamental properties of the neutrino's nature [47]. Their origin lies in the interactions of cosmic-rays with particles in the atmosphere of the Earth. cosmic-rays are high-energy particles such as protons or nuclei that have been created in extreme astrophysical environments and the nature of their accelerators is still an unsolved problem.

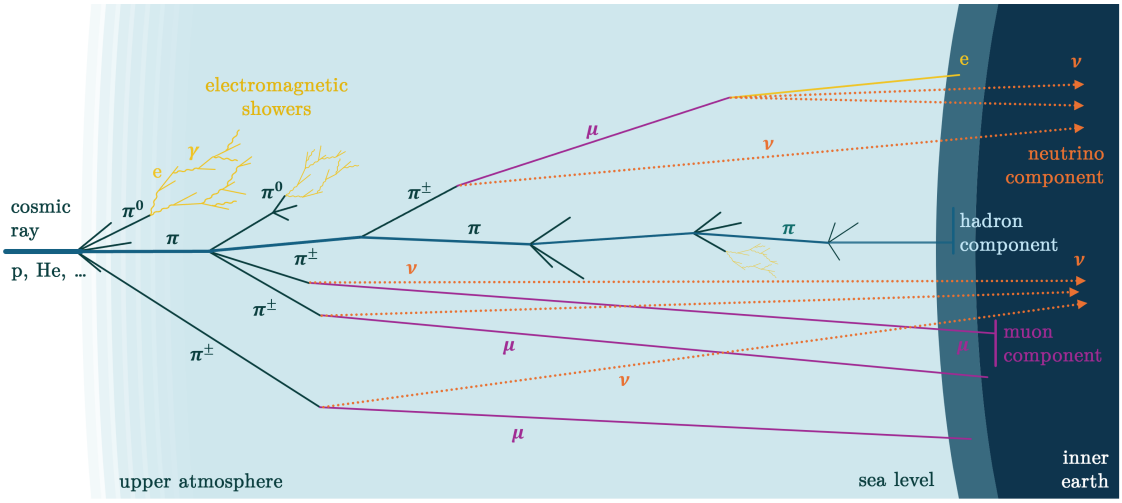

Figure 1.4: Schematic illustration of how an air shower of secondary particles forms from a cosmic-ray interaction in the upper atmosphere. Mesons created from the primary cosmic-ray interaction decay into muons and neutrinos with muons possibly further decaying into electrons and neutrinos. A part of the muons survives long enough to penetrate into the Earth up to a few tens of kilometers providing a background for many neutrino detectors. The created neutrinos travel further through the Earth. Illustration made based on [31]

Figure 1.4 illustrates an air shower of secondary particles that forms from a cosmic-ray interaction. The particles produced in the primary cosmic-ray interactions are mostly pions, kaons or free protons or neutrons [53].

$$p + N \rightarrow \pi^{\pm}, \pi^{0}, K^{\pm}, K^{0}, p, n \tag{1.16}$$

The short-lived mesons either decay or again interact with nuclei in the atmosphere, creating further mesons, cascading to lower energies. The neutral mesons dominantly decay into high-energy photons causing an electromagnetic shower. Responsible for the production of atmospheric neutrinos is mostly the charged pion, a state of bound quark-antiquark pairs of up and down quarks, and to a minor part also the charged kaon that consists of up-strange quark-antiquark pairs.

$$\begin{aligned} |\pi^{+}\rangle &= |u\bar{d}\rangle\,, & |\pi^{-}\rangle &= |\bar{u}d\rangle \\ |K^{+}\rangle &= |u\bar{s}\rangle\,, & |K^{-}\rangle &= |\bar{u}s\rangle \end{aligned} \tag{1.17}$$

They decay through the following interactions into a combination of muon μ^{-} and a muon antineutrino $\bar{\nu}_{\mu}$ or an antimuon μ^{+} and a muon neutrino ν_{μ}:

$$\begin{aligned} \pi^{+} &\rightarrow \mu^{+} + \nu_{\mu}, & \pi^{-} &\rightarrow \mu^{-} + \bar{\nu}_{\mu} \\ K^{+} &\rightarrow \mu^{+} + \nu_{\mu}, & K^{-} &\rightarrow \mu^{-} + \bar{\nu}_{\mu} \end{aligned} \tag{1.18}$$

The produced muons then further decay into electrons or positrons and a neutrino component as follows:

$$\begin{aligned} \mu^{-} &\rightarrow \mathrm{e}^{-} + \bar{\nu}_{\mathrm{e}} + \nu_{\mu} \\ \mu^{+} &\rightarrow \mathrm{e}^{+} + \nu_{\mathrm{e}} + \bar{\nu}_{\mu} \end{aligned} \tag{1.19}$$

We can see that from each decaying meson a muon-type neutrino is produced and if the charged lepton decays another muon-type and one electron-type neutrino is produced. This allows to set up a simple estimate for the expected ratio of $\nu_\mu/\nu_e \approx 2$ and to predict a high flux of muons strongly connected to the neutrino flux.

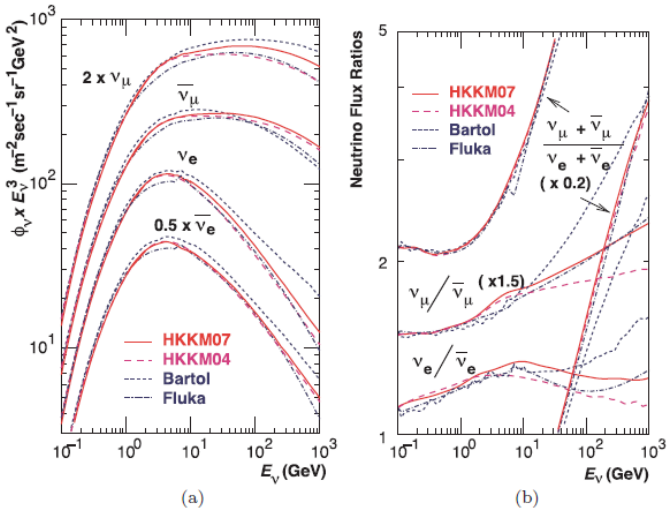

Figure 1.5: Expected fluxes of the atmospheric muons for the energy range of 100 MeV to 1 TeV (a) and expected ratios between the different particle types over energy (b) according to calculations with different models. Images taken from [47], calculations and plots done by [35]

The flux of atmospheric neutrinos with energies below 1 TeV shows a maximum around 1 GeV and approximately follows a power-law spectrum. The typical energy spectrum first follows the cosmic-ray spectrum with $\sim E^{-2.7}$ and above 100 GeV steepens to $\sim E^{-3.7}$. This is because the high-energy hadrons produced in the primary cosmic-ray interactions are more likely to further interact than to decay and by doing so they are ultimately producing neutrinos with lower energies instead, causing the steeper flux drop off compared to cosmic-rays [34]. Figure 1.5 shows the calculated flux of ν_μ, $\bar{\nu}_\mu$, ν_e and $\bar{\nu}_e$, as well as the expected ratios of $\nu/\bar{\nu}$ and μ-flavor/e-flavor.

The combination of different detection techniques allows to show a broad picture of the measured atmospheric neutrino flux. high-volume Cherenkov neutrino telescopes allow for the study of neutrinos with energies of more than 100 TeV, where the atmospheric neutrino flux is measured to lay between around 10^{-8} and 3×10^{-7} as shown in figure 1.6. Atmospheric neutrinos are arriving from all points in the Earth's atmosphere towards our detectors and provide a strong background when searching for neutrinos of cosmic origin. The flux is more dominant for directions closer to the horizon, along which the path of flight through the atmosphere for the pions produced in cosmic-ray interactions is longer, so the particle shower has more time to develop, resulting in a higher flux of neutrinos [47].

In addition to the conventional atmospheric neutrino flux just described, neutrinos might also get

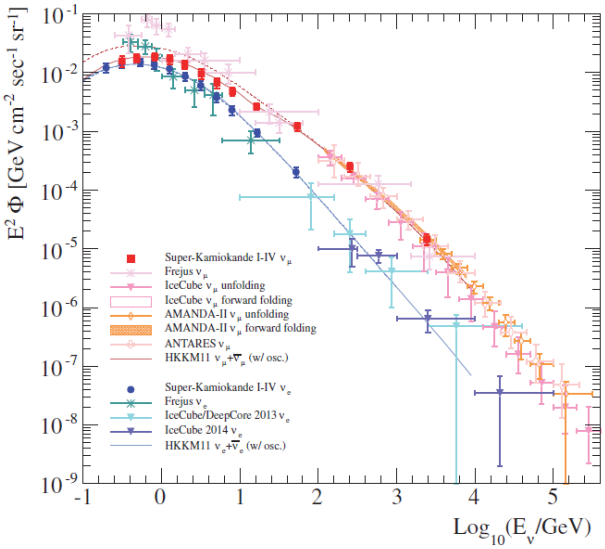

Figure 1.6: Measured ν_μ and ν_e energy spectra of atmospheric neutrinos from 100 keV to a few 100 TeV, combining measurements from Super-K, Frejus, AMANDA-II, IceCube and ANTARES. Images taken from [47], calculations and plots done by [49]

created through the decay of even shorter-lived $D^\pm$ and D^0 hadrons. This effect starts to become dominant over the pion and kaon decay at energies above a few 10 TeV for ν_e and a few 100 TeV for ν_μ [33]. Figure 1.7 shows the fluxes for energies above 50 GeV calculated by [26]. The neutrinos from these decays are called prompt neutrinos and their existence has yet to be experimentally confirmed. Advances in the detection of high-energy neutrinos might soon reveal more.

Looking at figure 1.7 we see that the largest background against high-energy neutrinos from cosmic objects is given by muon neutrinos consisting of a mixture of conventional and promt neutrinos at 10^5 GeV with the prompt neutrinos quickly starting to dominate the expected spectrum at energies above 10^6 GeV $= 1$ PeV. Even higher is the expected flux of atmospheric muons, which are also able to reach underwater neutrino detectors, providing the largest background in the event rate of produced Cherenkov emission. While those muons are able to penetrate significant amounts of matter up to a few 100 km, they are shielded by the Earth when looking down at events coming from below the horizon. Those can only be interactions from neutrinos that have traversed Earth. Most studies narrow their included data down to upwards traveling events in order to minimize the influence of the dominant atmospheric muon flux.

1.4.4 High-Energy Cosmic Neutrinos

Finally arriving at the subject of this work, we will now have a look at neutrinos with TeV to PeV energies possibly produced in cosmic accelerators from similar interactions as the ones that are happening in our atmosphere, but in the local environments of those astrophysical objects at very high energies. cosmic-rays accelerated in such objects can interact with matter and radiation of all

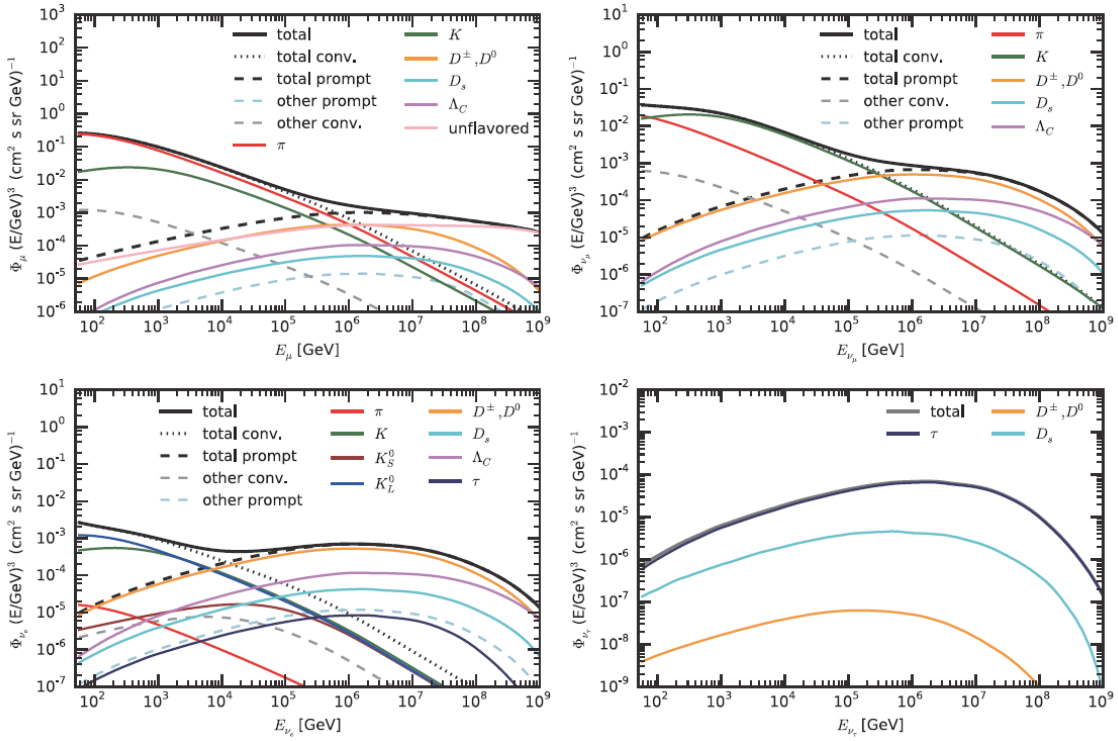

Figure 1.7: Fluxes of the atmospheric muons ($\mu^- + \mu^+$: upper left) and neutrinos ($\nu_\mu + \bar{\nu}_\mu$: upper right, $\nu_e + \bar{\nu}_e$: lower left and $\nu_\tau + \bar{\nu}_\tau$: lower right) at energies above 50 GeV. Image taken from [47], plots done by [26]

kinds close to where they were produced and consequently decay into hadrons, prominently pions $\pi^\pm$ or π^0, which further decay into ν_e, $\bar{\nu}_e$, ν_μ and $\bar{\nu}_\mu$. As already briefly discussed in section 1.3, the created neutrinos can then travel unhindered through space towards our detector, making neutrinos excellent messenger particles. The fact that neutrinos created in ultra high-energy cosmic-ray interactions close to the source of acceleration can escape all the electromagnetic interactions and be eventually detected here at Earth makes high-energy cosmic neutrinos the currently most promising candidates for revealing the unsolved mystery about the origin of cosmic-rays. If high-energy neutrinos from a possible cosmic-ray accelerator were detected, this would be very clear evidence for hadron acceleration processes actually take place and these neutrinos would provide a valuable source of probing the underlying mechanisms [53]. We will now have look at some cosmic objects from which the emission of high-energy neutrinos is expected.

In general, the neutrino flux originating from hadronic mechanisms can be estimated from a possible gamma ray flux that might already be studied. Evaluating the hadronic interactions that are thought to be responsible for neutrino and gamma ray production, one can roughly say that for each interaction a resulting emission of two γ-rays and six neutrinos is expected. Assuming that the region of emission is large enough, the flavor oscillation of the produced neutrinos over large astronomical distances causes full neutrino mixing, with an expected ratio of $\nu_e : \nu_\mu : \nu_\tau$ of $1 : 1 : 1$. The

expected ratio of neutrinos to antineutrinos is $\nu : \bar{\nu} = 1 : 1$ and due to the inability to differentiate them in detections ν and $\bar{\nu}$ are normally not differentiated in high-energy neutrino astronomy. This means that for each gamma ray one neutrino of each flavor would be expected in this simple picture. However, there are kinematic differences in the production of the outgoing neutrinos compared to the situation of the two gamma rays that are produced in the π^0-decay. This causes the expected flux of neutrinos per flavor to be around half of the gamma ray flux [53].

Naturally, the objects used for point source neutrino astronomy studies are those thought to be responsible for cosmic-ray acceleration, where one is able to set upper limits on the expected neutrino flux based on cosmic-ray and gamma ray experiments. In addition to searching for single sources, one can also use these ideas for estimates of a diffuse cosmic neutrino flux that is expected to originate from extragalactic cosmic-ray accelerators. This upper limit is predicted to exceed the atmospheric neutrino flux above energies of a few 100 TeV and is in the order of the following [53]:

$$[E^2 \Phi_{\nu_\mu}(E)]_{\max} \approx 10^{-8} \, \frac{\mathrm{GeV}}{\mathrm{cm}^2 \, \mathrm{s} \, \mathrm{sr}} \tag{1.20}$$

Latest results from IceCube using over 10 years of data taken show the following diffuse neutrino flux per flavor [1]:

$$\Phi_\nu(E_\nu)_{\mathrm{IceCube}} = \left(\frac{E_\nu}{100 \, \mathrm{TeV}} \right)^{-2.58} \cdot 1.68 \times 10^{-18} \, \frac{1}{\mathrm{GeV} \, \mathrm{cm}^2 \, \mathrm{s} \, \mathrm{sr}} \tag{1.21}$$

This allows us to compare the predicted flux to the IceCube result at the reference energy of 100 TeV by multiplying the presented differential flux by $(100 \, \mathrm{TeV})^2$, showing it in the same order of magnitude as the simplified prediction:

$$E^2 \Phi_\nu(E_\nu = 100 \, \mathrm{TeV})_{\mathrm{IceCube}} = 1.86 \times 10^{-8} \, \frac{\mathrm{GeV}}{\mathrm{cm}^2 \, \mathrm{s} \, \mathrm{sr}} \tag{1.22}$$

1.5 Detection of Astrophysical Neutrinos

We will now have a short look at the detection principle of high-volume neutrino detectors. First, an overview about the involved interactions by which neutrinos produce detectable particles will be given, before the detection mechanism of Cherenkov neutrino telescopes will be presented.

1.5.1 Interaction Processes

As we have seen in section 1.2, neutrinos interact only via the weak force through the exchange of $W^\pm$ and Z^0 bosons. The interactions can be separated into two types: charged current (CC) interactions, where a charged W^+ or W^- boson is exchanged and the neutrino is transformed to a charged lepton or vice versa ($\nu_l \leftrightarrow l$ with $l = \mathrm{e}, \mu, \tau$) and neutral current (NC) interactions, where a Z^0 boson is exchanged and the neutrino state is unchanged [46]. With neutrinos spanning over a huge energy range, there are multiple effects involved when it comes to actual interactions between neutrinos and nuclei in the detector. In the high-energy regime of comic neutrinos the dominant interaction process is the so-called deep inelastic neutrino-nucleus scattering, which happens both through CC and NC interactions. In both cases the neutrinos interact with a quark inside the nucleon, resulting

in the break up of the bound nucleon stat N and the emission of a free quark and a lepton. The quark quickly recombines and forms a hadronic shower X, consisting of multiple interactions with nucleons in the surrounding matter, cascading down the energy, as it was described for the case of a cosmic-ray interaction in the production mechanism of atmospheric neutrinos. Overall, we can summarize the following deep inelastic scattering processes [28]:

$$\nu_l + N \rightarrow l^- + X \quad \text{(CC)} \tag{1.23}$$

$$\bar{\nu}_l + N \rightarrow l^+ + X \quad \text{(CC)} \tag{1.24}$$

$$\nu_l + N \rightarrow \nu_l + X \quad \text{(NC)} \tag{1.25}$$

$$\bar{\nu}_l + N \rightarrow \bar{\nu}_l + X \quad \text{(NC)} \tag{1.26}$$

So the expected possible outcomes of the neutrino-nucleus interaction are neutrinos, charged leptons and hadronic showers. The charged leptons possibly leaving this interaction can then further interact with the surrounding matter or decay into a lower-generation lepton if possible. Due to the presence of electrons in the atoms inside the detector,emitted electrons or positrons instantly reinteract and form an electromagnetic shower. The differences in interaction signatures can be used to distinguish particle types in large-volume neutrino detectors [28]. Figure 1.8 shows an overview of the most common signature topologies. Note that these illustrate the "outside" view of these interactions, only showing the actual effects that one would be able to observe. The inner reactions between neutrino and nucleus occur through the exchange of a $W^{\pm}$- or Z^0-boson coupling to the neutrino and one of the quarks inside a nucleon. This results in an accelerated quark or meson $(\pi, K, ...)$ leaving the interaction but very shortly afterwards reinteracting and forming a particle shower. The same is the case for the electron produced in a ν_e CC interaction, which immediately starts interacting again and forms an electromagnetic shower.

While neutrino-nucleon scattering forms by far the most dominant interaction mechanism through which neutrinos are interacting with matter and are possibly detected, the neutrinos can also interact with the electrons in the target material. While this depends a lot on the energy range and the particle type of the interacting neutrino, the neutrino-nucleus cross section is in general so much higher that the influence from neutrino-electron scattering can be neglected in most cases. It gets important however, when we look at $\bar{\nu}_e$-e^--interactions around the energy of 6.3 PeV, where the following interaction causes the resonant production of a W^--boson, when the centre of mass energy of the neutrino-electron interaction is exactly M_W. In this energy region, the cross section of the neutrino-electron scattering becomes very high and this process strongly dominates the neutrino interactions. It also plays a great role when dealing with neutrino oscillation in matter, where this discrepancy in the interactions that the different neutrino flavors take part in, sets the basis for studying the neutrino mass ordering, for example [5].

1.5.2 Cherenkov Neutrino Telescopes

As we just saw, the interaction of neutrinos with nuclei leads to the creation of hadronic showers, electromagnetic showers and muons that keep propagating through the detection volume. Now, how could we detect and characterize these interaction products to be able to tell something about the original neutrino interaction?

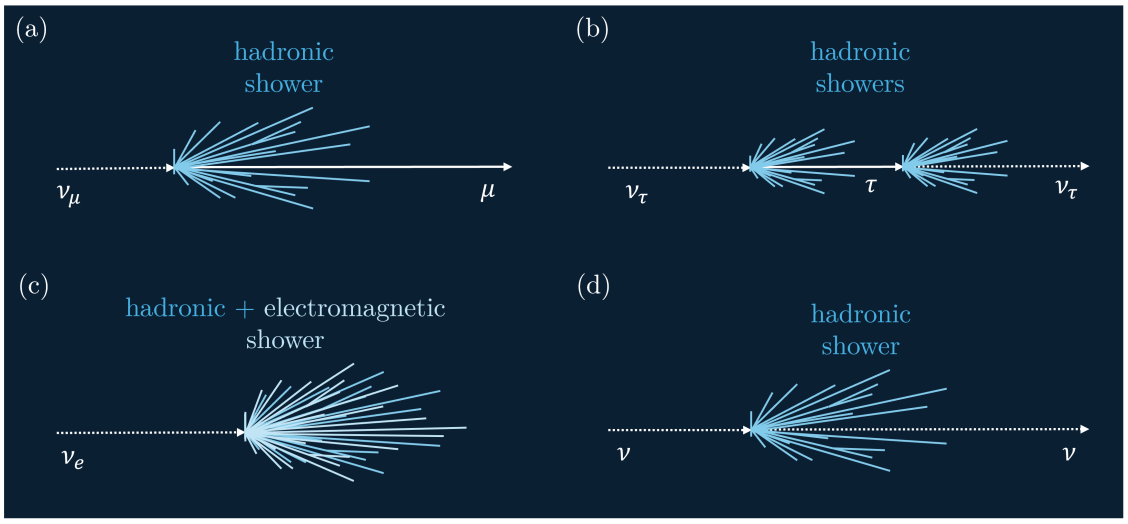

Figure 1.8: Schematic illustration of the most important event signature topologies for different flavors and interactions: CC interaction of a ν_μ resulkting in a hadronic shower and muon production (a), CC interaction of a ν_τ resulting in a double bang signature (b), CC interaction of ν_e resulting in an electromagnetic and hadronic shower (c) and NC interactions which only produces a hadronic shower independently of the neutrino flavor. Illustration made based on an image by [53]

The clue to how this is done lies in the so-called Cherenkov effect, which was experimentally discovered by Pavel Cherenkov in 1934. The effect describes the emission of light from the atoms inside a dielectric medium when a high-energy charged particle travels through it at a speed that is higher than the phase velocity of light in this medium. The mechanism behind this Cherenkov light is connected to how a moving charged particle alters the position of electrons bound in the matter which the particle is passing through. The moving particle's field induces a change in the dielectric polarization of an atom, which instead emits a disturbing field when the influenced atom moves back to its stable ground state. In the situation where the charged particle is moving slower than the speed of light in this medium, all the energy transferred to the medium through this interaction is deposited closely to the particle track and in the far field, the field disturbances are destructively interfering. If the particle's velocity exceeds the local speed of the photons however, the emission of photons into a certain direction is no longer prohibited, with the field disturbances constructively interfering in a cone around the particle's flight path. These photons can be seen as Cherenkov radiation, which is oriented in a characteristic way depending on the material's properties and the particle's velocity [37].

The important takeaway from this for understanding the principle used to detect high-energy neutrinos is that highly energetic charged particles produce the emission of light in the form of Cherenkov radiation in certain media. The orientation of this emission cone follows the particle trajectory and the opening angle depends on the material and the energy of the particle. In transparent media with sufficiently long optical attenuation lengths, this light can propagate far enough to be detected.

Returning to the neutrino interaction mechanisms presented earlier, we can now think about how the detection of Cherenkov radiation from the resulting charged particles can be used to reconstruct the properties of the neutrinos involved in these processes. Each charged particle produced in these interactions causes the emission of Cherenkov radiation in a cone along its flightpath as long as the particle's energy is high enough. Some of them exist only very quickly until they decay or reinteract again, causing a spread out distribution of light emission as a superposition of all the individual Cherenkov cones. We will now shortly examine the Cherenkov light signature that each interaction product creates:

- **muons:** Muons travel on a long straight track until they decay into electrons or interact. high-energy muons can travel for several kilometers, a 250 GeV muon in water for example around 1 km. This produces a well oriented emission cone, along which photons are uniformly produced throughout the track.
- **electrons:** Electrons leaving a neutrino interaction immediately induce a cascade of interactions in the form of an electromagnetic shower. The energy of the particles produced in this shower is deposited in small volume only extending up to 7 m along the initial trajectory for 1 TeV interactions.
- **tau:** The very short-lived tau leptons travel for only short distances (at 100 GeV: 5 mm), which at high enough energies can still be far enough to be detectable. The decay can produce an electron, a muon or a hadron, which causes a ν_τ interaction to form a broad spectrum regarding the resulting Cherenkov signature that overlap with that of ν_e and ν_μ interactions. For lower energies the tau interactions are hardly to differentiate from electron interactions and muons produced from tau interactions outside of a detector will produce muons that are not distinguishable from those produced from muon neutrinos.
- **hadrons:** The interaction cascade following a hadron resulting from a high-energy collision is similar to that of an electromagnetic shower, but shows a broader spatial distribution and a lower overall emission.

The idea behind Cherenkov neutrino telescopes is to detect the Cherenkov light produced from the particles produced in neutrino interactions in order to trace back the neutrino's energy, direction and flavor. From the signatures presented above one can see that this is only possible to a certain extent. The direction of muons can be reconstructed very well, but can originate from ν_μ and ν_τ interactions from far outside the detector volume, making it hard to estimate the initial neutrino energy. Electron neutrinos on the other hand are only detected when interacting inside the detection volume. However, since the produced electron deposits all the energy in a small region in the detector, the energy of these interactions is mostly well determined from the measurements of the produced Cherenkov light [5].

Today, the young field of neutrino astronomy is putting its hope into high-volume Cherenkov detectors that use a three-dimensional array of light detectors, which are embedded in a transparent detection medium such as ice or water. The timing and spatial correlation between photon detections can be used to reconstruct the interacting neutrinos' properties using sophisticated algorithms and simulation techniques. The huge dimensions of these detection arrays enable the detection of highly energetic neutrinos simply by increasing the probability for an interaction through their sheer size. While the physical scale and sensitivity of these detectors are essential, their ability to achieve the goal of experimentally detecting, identifying and analyzing high-energy neutrinos depends just as much on the computational power and the quality of the (reconstruction) algorithms. The design

of high-volume Cherenkov detectors is in principle the same for various detectors, e.g. IceCube in the deep ice at the south pole, the currently constructed Baikal-GVD in the waters of Lake Baikal or KM3NeT in the depths of the Mediterranean Sea. Photo-detectors are aligned on a string and multiple strings are put together to form a grid of optical detectors that can then be used to detect neutrino interactions taking place sufficiently close to the detector [53]. In figure 1.9 this principle is illustrated for an underwater detector on the sea floor, as is the case for KM3NeT. In section 1.6 we will have a closer look at the detector design and the simulation and signal processing chain within KM3NeT.

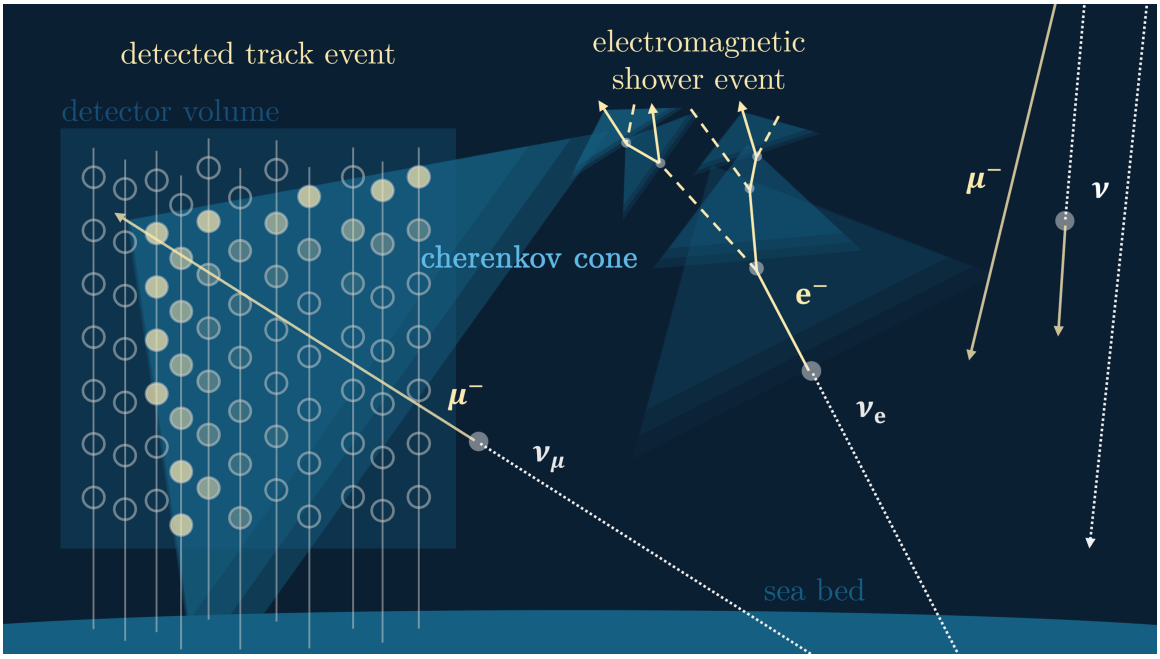

Figure 1.9: Schematic illustration of how neutrinos can be detected by measuring the Cherenkov light produced by secondary charged leptons created during a neutrino interaction close enough to the detector volume producing a characteristic Cherenkov signature.

1.6 The KM3NeT Neutrino Telescope

This chapter provides an overview of the KM3NeT Neutrino Telescope, highlighting its fundamental principles and objectives. The KM3NeT ("Cubic Kilometer (KM3) Neutrino Telescope") collaboration is currently building and operating two underwater Cherenkov neutrino telescopes in the Mediterranean Sea. The project builds on experience from previous underwater neutrino experiments in the Mediterranean, such as NEMO, NESTOR and especially ANTARES and involves numerous research institutions from Europe and around the world. Figure 1.10 shows the institutes currently involved and the selected sea cites, where the telescopes are or might be constructed. KM3NeT comprises two different detectors, which are generally based on the same technology regarding detector components and data analysis, however, both detectors are optimized for different energy ranges and science goals. ORCA ("Oscillation Research with Cosmics in the Abyss"), located

at the off-shore site near Toulon in France, is designed for the study of oscillation in atmospheric neutrinos, with the main goal of advancing the knowledge about the ordering of the masses of the neutrino mass states. The ARCA detector ("Astroparticle Research with Cosmics in the Abyss") is located at the off shore site near Capo Passeiro about 100 km south of the Sicilian coast. The detector is designed for the study of high-energy cosmic neutrinos with energies up to several PeV, providing a very good angular resolution, especially for track-like neutrino interactions. The offshore site in Greece, which is also shown on the map, might be used for deployments in the future [18].

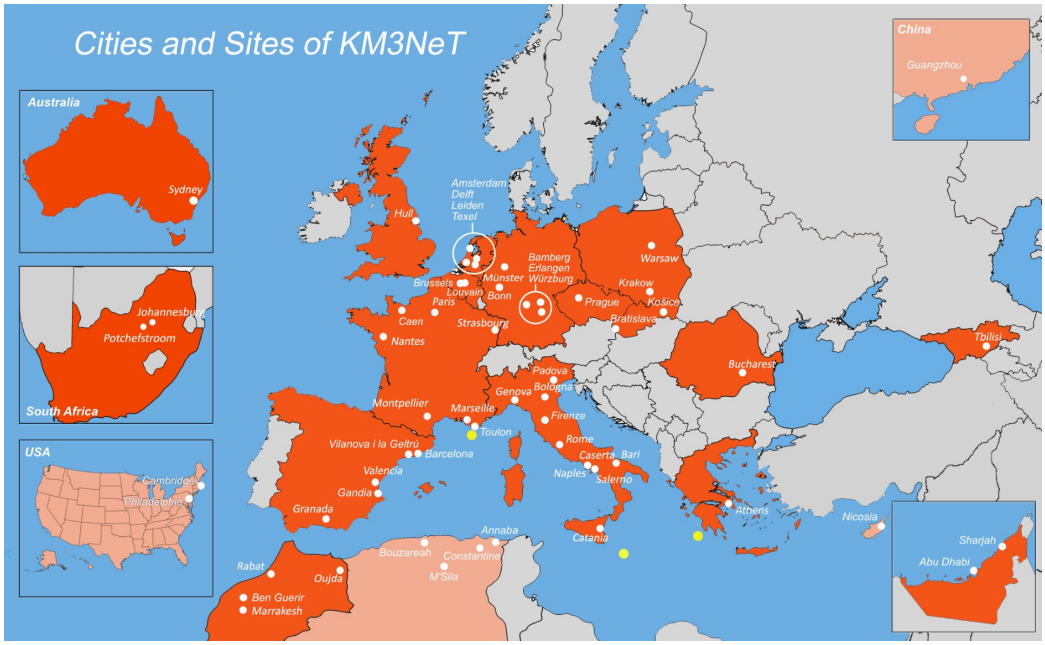

Figure 1.10: Cities and sites associated with KM3NeT. The locations marked in yellow indicate the (planned) detector sites [16]

Each KM3NeT building block comprises 115 uniformly spaced strings anchored to the seabed with each string housing 18 digital optical modules (DOMs) along its length. A submerged buoy at the string's top maintains its alignment. Each DOM contains 31 photo-multiplier-tubes (PMTs) arranged spherically, coupled with readout electronics and three calibration sensors: an LED beacon for positional calibration, a compass and tilt-meter for orientation, and an acoustic piezo for position calibration [18]. Figure 1.11 shows a schematic view of the setup. ORCA consists of one building block with the DOMs vertically spaced around 9 m along the strings, which reach an overall height of around 100 m. The vertical separation between the strings is around 40 m. ARCA on the other hand combined two building blocks with 115 strings each, where the DOMs are vertically 40 m apart and horizontally spaced at a distance of around 100 mm [18]. Notice, that this is the planned final detector configuration. Currently, there are 28 detection units in operation at ORCA and 51 at ARCA [17] and [15]. The detector is sequentially growing towards its final size, but already allows for promising neutrino research. A highlight was the detection of the highest neutrino ever recorded, with the results published in [19].

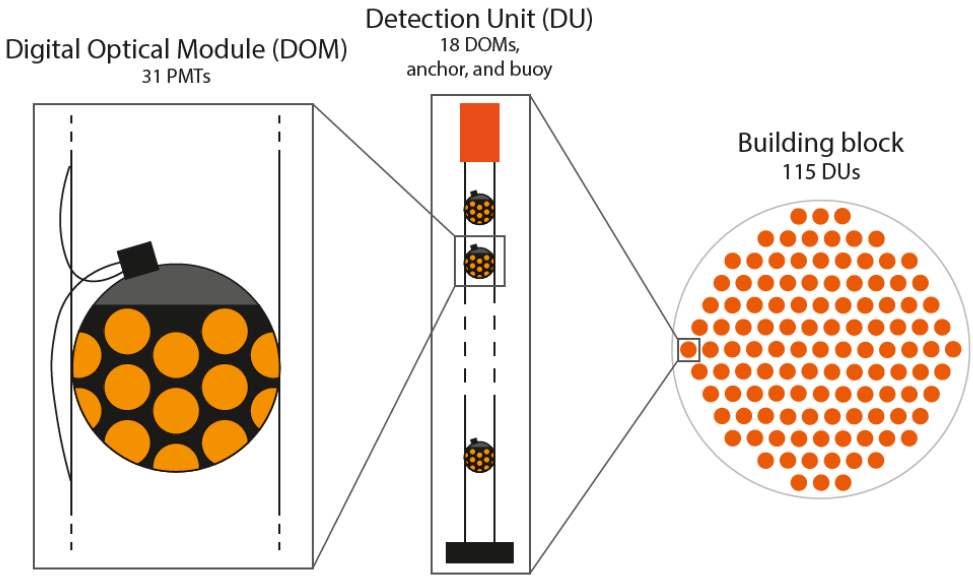

Figure 1.11: Illustration of the individual detector components, taken from [12]

As presented in the previous section, the detection principle of underwater Cherenkov neutrino telescopes is based on the detection of light signatures arising from the movement of high-energetic charged particles that are created in neutrino-nucleus interactions. Measuring the timing and spatial correlation of the emitted Cherenkov light allows for the reconstruction of the flavor, energy and direction of the underlying neutrino. This already indicates that such telescopes are heavily relying on high performance computation and high quality reconstruction and analysis algorithms. The general approach is the usage of sophisticated Monte Carlo simulations, which simulate the expected detection response to a huge number of initially simulated neutrino interactions. These simulations cover each part from the neutrino-nucleus interactions, the propagation of the particles leaving this primary interaction, the emission and propagation of Cherenkov light in the surrounding water and the trigger behavior of the PMTs. In order to trace back the initial neutrino's properties from the trigger signature, a number of different classical and machine-learning based algorithms are used and fine tuned with the Monte Carlo simulations. These reconstruction algorithms can then be applied to real events recorded with the corresponding detector, which allows to reconstruct information about the interacting neutrinos. For each KM3NeT detector, two different algorithms are used, which are fine tuned towards the reconstruction of either tracks or showers. Both algorithms are applied to detected events and a classifier will the be used to identify, which reconstruction is more likely to yield the correct information about the underlying neutrino. The track reconstruction is expected to precisely reconstruct the tracks of muons or anti muons produced from ν_μ or $\bar{\nu}_\mu$. The shower reconstruction works better for ν_e, $\bar{\nu}_\mathrm{e}$, ν_τ or $\bar{\nu}_\tau$ interactions [32]. However, the reconstruction quality depends strongly on how the resulting track or shower is produced in the detector and if all the light is actually measured by the PMTs or not and can also lead to strongly misreconstructed information in some cases.

2 Introduction to Pulsars and X-Ray Binaries

Since this analysis deals with the search for periodic neutrino sources, we will naturally look for objects that produce periodic emission in the form of other particles such as photons or accelerated protons, especially in the high-energy range. The idea behind this is that some of the mechanisms underlying the emission of light and possibly protons in the form of a pulsating signal could also lead to the generation of neutrinos in a similar manner when they interact with other particles. We will step by step get to know the objects suitable for this work's study and introduce the concepts necessary to understand the mechanisms that lead to periodic emission from pulsars and X-ray binaries. The characteristics of neutron stars will be presented and an effort is made to explain how extreme these objects are and how this leads to the behavior we can observe in pulsars. We will set up a basis for the discussion about why that makes them candidates for high-energy neutrino emission.

2.1 Neutron Stars

When the stable burning phase of a star ends, the thermal and radiation pressure can no longer overcome the star's own gravitational potential, leading to the collapse of the star. To give a simple picture, three main evolutionary outcomes can be distinguished on the basis of the star's mass. Note however, that the final phases of a star's evolution can be very complex and can differ greatly for stars that end up in a similar final state. Stars with initial main-sequence star masses of $M < 2.5 M_\odot$, where $M_\odot$ is the mass of the Sun do not have enough gravitational potential to overcome the free electrons' Fermi pressure, a degeneracy pressure originating from the Pauli exclusion principle, which prevents electrons from being compressed into the same quantum state and thereby provides an effective repulsive force counteracting gravity during their contraction. This causes the star to either enter a stable helium-rich end state or another helium-burning phase that ultimately causes the ejection of the star's outer layers, leaving only a carbon-oxygen core. In both cases they evolve into a *white dwarf*, the non-luminous core of a collapsed star where no significant fusion processes are taking place anymore. Such stellar remnants can exist with masses up to the Chandrasekhar mass limit of around $1.44\,M_\odot$ [22].

For stars with initial masses above the $2.5 M_\odot$ threshold, the resulting white dwarfs reach masses above the Chandrasekhar limit and the electron's Fermi energy increases up to a point where it overcomes the mass difference between neutrons and protons ($E_F > (m_n - n_p) \cdot c^2$), allowing the free electrons and the protons of the remaining helium to undergo inverse beta decay, leaving a neutron and an electron neutrino:

$$\mathrm{e}^- + \mathrm{p} \rightarrow \mathrm{n} + \nu_\mathrm{e} \tag{2.1}$$

This causes a decline of the electron density in the electron-nuclei-plasma that is present in the collapsed star, causing it to further compress. Through this further collapse, the density of the inner star rises above $\rho \approx 10^{16}\,\mathrm{kg/m^3}$, leading to a high increase of the neutron degeneracy pressure. Analogously to the electrons' Fermi pressure counteracting the compression in white dwarfs, this settles at a radius where the neutrons' degeneracy pressure balances out the gravitational potential

[22]. This object is known as a *neutron star*.

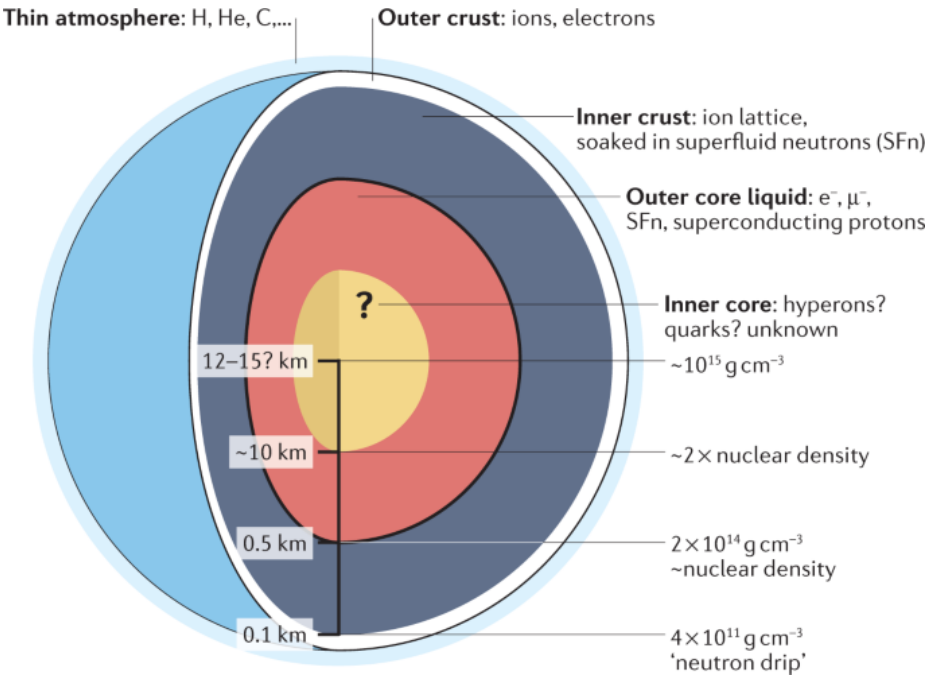

Figure 2.1: Schematic view of a neutron star's inner structure. Alongside with the suspected constituents an estimate for the density at the region boundaries is shown. Taken from [59]

The existence of neutron stars, being "stellar bodies made up mainly of neutrons" with "a very small radius and extremely high density", possibly surpassing the densities of atomic nuclei, was already proposed in 1934, just two years after the discovery of the neutron [6]. Modern day neutron star models allow to describe their evolution and properties in a more sophisticated way, presenting them as one of the most extreme objects in our universe. With remaining masses of $M \approx 1 - 3\,M_\odot$ and radii in the scale of $R \approx 10\,\mathrm{km}$, neutron stars provide such extreme conditions, that causes to form very special states of matter in their insides [22]. In the following, we will try to get a sense of how peculiar neutron stars actually are and how this creates the conditions for pulsars and X-ray binaries to produce (periodic) emissions that we can detect on Earth.

On a neutron star's surface the density and gravitational pressure are still low enough for ordinary nuclei to exist. This region contains heavy nuclei, probably mostly iron from the collapsing star's core, as well as free degenerate electrons and with increasing depth more and more protons of the iron nuclei are converted into neutrons, causing a rise in neutron-rich iron isotopes. After around 10 m the density starts to exceed $\rho \approx 4 \times 10^{14}\,\mathrm{kg/m^3}$, allowing free neutrons to exist. This region called the inner crust consists of a mixture of a free neutron fluid, neutron-rich nuclei and degenerate electrons. Through spontaneous pairing of degenerate neutrons, they form what is known as a superfluid. The combined neutron pairs are not subject to the Pauli exclusion principle anymore and can all exist in the lowest energy state, causing the superfluid to flow without resistance and

allowing whirls and vortices in the fluid to spin forever without energy loss. With densities reaching those inside regular nuclei they effectively dissolve into a fluid mixture of free neutrons, protons and electrons. Similar to the neutrons, the free protons start forming pairs, resulting in a fluid that not only does not have flow resistance but is also superconducting, having zero electrical resistance. The ratio of neutrons to protons to electrons is expected to settle at a limit of $8\,\mathrm{n} : 1\,\mathrm{p} : 1\,\mathrm{e}^-$, however, the properties at the center of a neutron star are still poorly understood, with possible spontaneous decay of free neutrons into protons and negatively charged pions or the appearance of sub-nuclear particles like free quarks [10].

This highlights the strange properties that arise due to the enormous gravitational pressure inside neutron stars. A typical neutron star with a mass of around $1.5\,M_\odot$ would be expected to have a mean density of $\rho_{\mathrm{ns}} \approx 6.64 \times 10^{17}\,\mathrm{kg/m^3}$, exceeding the typical density of an atomic nucleus, which is around $\rho_{\mathrm{nuc}} \approx 2.3 \times 10^{17}\,\mathrm{kg/m^3}$. On the surface of a neutron star with $R = 10\,\mathrm{km}$ one would feel a gravitational pull of $g = 1.86 \times 10^{12}\,\mathrm{m/s^2}$, which would accelerate a stationary object over the course of 1 m to an incredible speed of $1.93 \times 10^6\,\mathrm{m/s}$ [10].

Another outstanding property arises from the fact that all stars have some sort of rotation due to a non-zero net angular momentum during their formation. Having in mind that a neutron star evolves from stars that have enough mass to overcome the electron degeneracy pressure in their white dwarf state, one can assess how this rotation is transferred to the remaining neutron star during its formation. If for simplicity we assume that no mass is lost during the core collapse, meaning $M_{\mathrm{core}} = M_{\mathrm{wd}} = M_{\mathrm{ns}}$, we can estimate each star's moment of inertia to be of the form $I = CMR^2$ with mass M, radius R and a constant factor C that characterizes the mass distribution inside the star. If we apply the conservation of angular momentum to this simple model and assume that the factor C does not change much, we get the following [10].

$$I_i \cdot \omega_i = C_i \cdot M_i \cdot R_i^2 \cdot \omega_i = const \tag{2.2}$$

$$\Rightarrow \omega_{\mathrm{ns}} = \omega_{\mathrm{core}} \cdot \left(\frac{R_{\mathrm{core}}}{R_{\mathrm{ns}}}\right)^2 \tag{2.3}$$

Very basic estimates can show that the ratio of the radii between the progenitor star's core and the neutron star is in the scale of $R_{\mathrm{core}}/R_{\mathrm{ns}} \approx 500$. This allows us to approximate the rotational period P of a neutron star:

$$P_{\mathrm{ns}} = \left(\frac{R_{\mathrm{ns}}}{R_{\mathrm{core}}}\right)^2 P_{\mathrm{core}} \approx 4 \times 10^{-6} \cdot P_{\mathrm{core}} \tag{2.4}$$

Using the observed rotational period of the white dwarf Eridani B., which is about 1350 s, we calculate the neutron star's period to be around $5 \times 10^{-3}\,\mathrm{s}$. This shows that neutron stars are expected to rotate very rapidly "with rotation periods on the order of a few milliseconds" [10].

The collapse into a neutron star also shows a strong effect on the magnetic field present inside a star. Although its evolution during a collapse into a neutron star still remains unclear to a large extent, there are predictions which state that the magnetic flux through the surface of a neutron star's progenitor will be conserved during collapse. A rough estimation allows to approximate the magnetic field strengths that arise inside neutron stars based on observations of magnetic fields in white dwarfs and the earlier presented estimates for neutron star radii [10]. Conservation of the magnetic flux through the surface has the following consequences.

$$\int_S \vec{B} \cdot d\vec{A} \approx B_{\mathrm{wd}} \cdot 4\pi \cdot R_{\mathrm{wd}}^2 = B_{\mathrm{ns}} \cdot 4\pi \cdot R_{\mathrm{ns}}^2 \tag{2.5}$$

Using a typical white dwarf magnetic field of $B \approx 10\,\mathrm{T}$ and a typical radii ratio of $R_{\mathrm{wd}}/R_{\mathrm{ns}} \approx 500$ this yields:

$$\Rightarrow B_{\mathrm{ns}} \approx B_{\mathrm{wd}} \cdot \left(\frac{R_{\mathrm{wd}}}{R_{\mathrm{ns}}}\right)^2 = 10\,\mathrm{T} \cdot 500^2 = 2.5 \times 10^7\,\mathrm{T} \tag{2.6}$$

This gives a hint towards the high energies that magnetic fields developing in neutron stars can reach. In extreme cases, when the progenitor star's magnetic field is strong enough, they can also possibly exceed field strengths of $10^{10}\,\mathrm{T}$ [10]. Overall, the properties presented in this subsection highlight why neutron stars are highly interesting astronomical objects that offer a great opportunity for the study of high-energy physics and why they are possible candidates for the acceleration of high-energy cosmic-rays. In the remaining part of this section we will dive deeper into special types of neutron stars that are producing electromagnetic emission in a periodic manner: pulsars and X-ray binaries.

2.2 Pulsars

The first pulsar was discovered in 1967 by Joycelyn Bell-Burnell when studying radio signals coming from quasars. The first discovery of such a stable periodic signal first drew the researchers' thoughts to signals from extraterrestrial life, before they discovered a number of similarly behaved signals from all over the sky, which was hinting at a natural phenomenon [50]. One of the best studied sources of these radio pulses is located in the Crab nebula, a supernova remnant in the Taurus constellation, which shows a periodic emission with $P_{\mathrm{crab}} \approx 33\,\mathrm{ms}$ being emitted from a central object. In figure 2.2 the folded lightcurves of the Crab pulsar are shown for measurements from different instruments spanning over a broad energy range from $1.4\,\mathrm{GHz}$ (around $5.8 \times 10^{-6}\,\mathrm{eV}$) radio up to gamma rays above $25\,\mathrm{GeV}$. One can clearly see that there are periodic emission patterns present in each energy range. A lightcurve consists of event counts of a measurement coming from a chosen astrophysical source, storing information about how much emission was coming from the direction of that source over time. The phase folding of a lightcurve shows the evolution of emission intensity over the course of one rotation period of the analyzed object. The method will be explained in more detail in section 3.5.1.

The short periods of the discovered pulses in the range of a few milliseconds to seconds show that this emission is coming from a very compact source. The spatial extent of a region that emits pulses with $P \approx 1\,\mathrm{ms}$ can be roughly estimated by looking at the maximum difference in distance light can travel within this period.

$$\Delta t_\gamma \approx \frac{2R_{\mathrm{max}}}{c} \Leftrightarrow R_{\mathrm{max}} \approx 1.5 \times 10^5\,\mathrm{m} = 150\,\mathrm{km} \tag{2.7}$$

More advanced studies could detect an even finer timing structure within those pulses, which could be used to narrow down the spatial extent of the source objects even further, leading to the question of which objects are that compact and could produce such a powerful periodic emission. Although this discussion has not yet been completely settled, many signs support the idea that pulsars are *rapidly rotating neutron stars*. In the following, we will explore how the measured pulsar emission characteristics could be explained by this model and what other observations hint at that.

First of all, the fast rotation of a high-mass compact object and the huge angular momentum carried by that would result in a very stable rotation, showing precise clock-like spin periods. This goes well

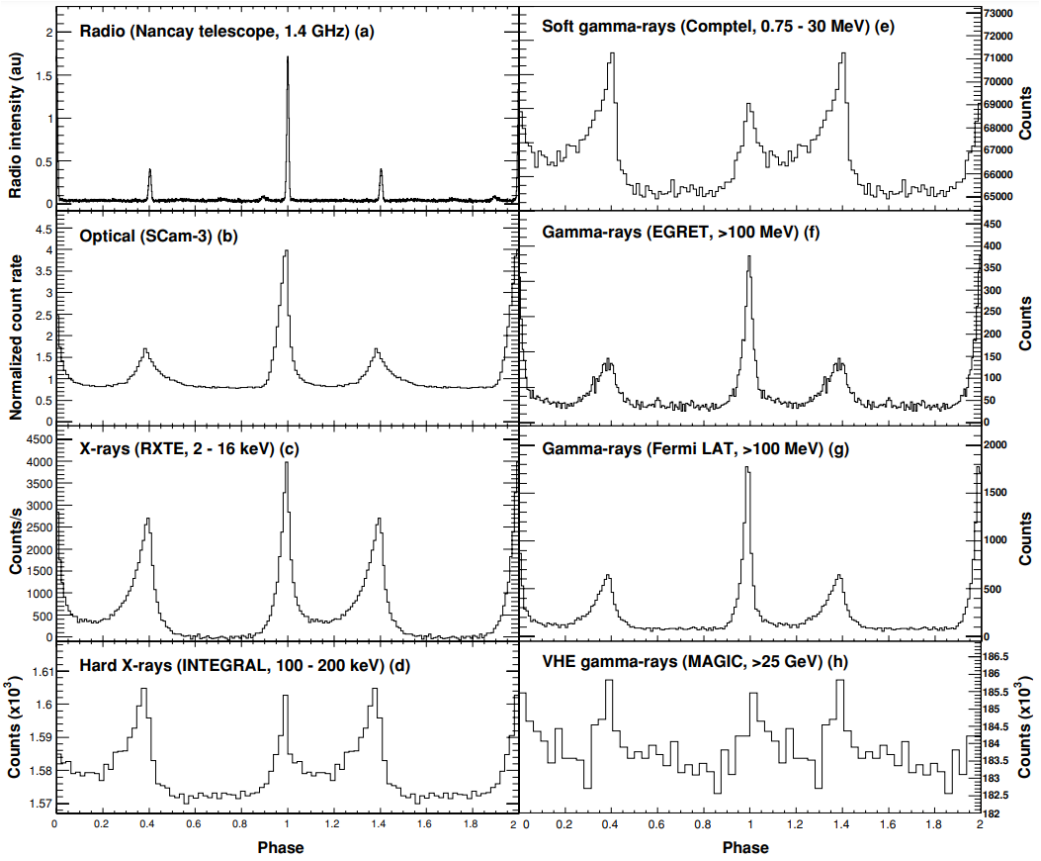

Figure 2.2: Folded lightcurves from the Crab pulsar in different energy ranges. Each signal was folded using the rotation period of 33 ms and centered with the peak in the 1.4 GHz radio emission at phase 0, with two cycles being shown. Composition done by [3]

along with the pulsation behavior of observed emission from pulsars. Also, the previously motivated spin periods of neutron stars forming from the core collapse of a progenitor star are of exactly the orders of magnitude that are observed for the emission periods in pulsars. Now, one could think that white dwarfs evolving from initially already quickly rotating progenitor stars might also be able to form such fast and stable rotations. However, one also needs to consider the effect that this fast rotation has on the matter of the rotating object itself. We can classically estimate the maximum angular velocity $\omega_{\max}$ of a rotating object with mass M and radius R, up to which gravity is still able to hold the object together:

$$\omega_{\max}^2 R = G\frac{M}{R^2} \tag{2.8}$$

Here, $G = 6.674 \times 10^{-11}\,\mathrm{m^3 kg^{-1} s^{-2}}$ is the gravitational constant. We can rewrite this to get the minimum orbital period $P_{\min}$:

$$P_{\min} = \frac{2\pi}{\omega_{\max}} = 2\pi\sqrt{\frac{R^3}{GM}} \tag{2.9}$$

Using the mass and radius of typical white dwarfs, with $R_{\mathrm{wd}} = 1M_\odot$ and $R_{\mathrm{wd}} = 0.01R_\odot$, this gives

a minimal rotation period of $P_{\mathrm{wd,min}} = 10\,\mathrm{s}$. For a typical neutron star with $M_{\mathrm{ns}} = 1.4 M_{\odot}$ and $R_{\mathrm{ns}} = 10\,\mathrm{km}$ on the other side, we get a minimal rotation period of $P_{\mathrm{ns,min}} = 4.6 \times 10^{-4}\,\mathrm{s} = 0.46\,\mathrm{ms}$. This shows that if the mechanisms behind periodic pulsar emission are connected to the rotation period of a compact object, it could only come from neutron stars, since white dwarfs could not reach these rotational velocities without disintegrating.

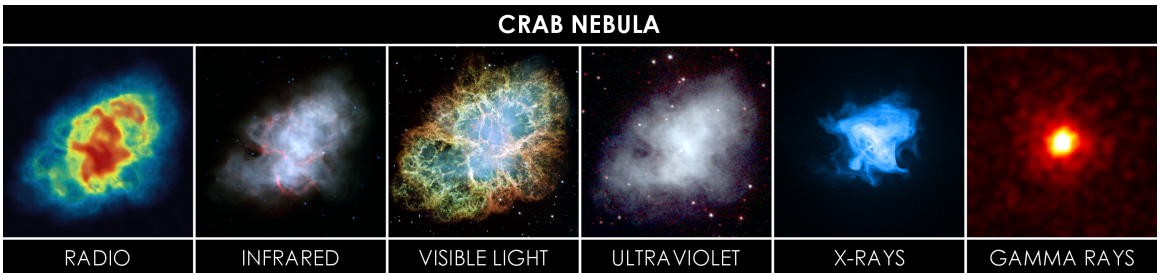

Figure 2.3: Crab nebula in multiple wavelengths: Radio *(Very Large Array)*, Infrared *(Spitzer)*, Visible *(Hubble)*, UV *(Swift)*, X-rays *(Chandra)* and Gamma-rays *(Fermi)*. Notice the clear visibility of the Crab pulsar with jets and the pulsar wind nebulae in the X-ray band. Image composition taken from [57]

Another fact that strengthens the hypothesis of neutron stars forming the objects we call pulsars is that many pulsars are detected to be located in the central regions of supernovae remnants, as is the case, for example, for the Vela and Crab pulsars. This suggests that they might be the final stage of the core-collapse supernovae, which is also backed by the observation that the fraction of pulsars belonging to a binary system is much lower than for the average star and the relative velocity in space is much higher. This could be explained by the core collapse not happening perfectly spherically symmetric, which would give the collapsed core a non-zero net momentum in some direction. This could cause the neutron star to be ejected from a binary system the progenitor star was possibly part of and would explain the pulsars' high relative velocities in space compared to other objects [10]. This phenomenon that causes many neutron stars to have a much higher velocity than their progenitor stars or other stars close by is called neutron star kick. Notice that while asymmetric collapse is the most natural explanation for these kicks, there are also various other mechanisms that are considered to be responsible. The lack of deep understanding of the involved physics allows for many ways of interpreting observations. Two other possibilities are related to asymmetric neutrino emission and the development of asymmetric jets. The first idea would be that one might expect acceleration from asymmetric neutrino emission because of the parity violating behavior of the weak interaction that results in different interaction probabilities depending on the orientation between a neutrino's momentum and the direction of the strong magnetic field that is present in neutron stars. The second idea would be that an off-centered dipole inside neutron stars would form asymmetric jets that gradually accelerate neutron stars in a certain direction over time, transferring rotational energy into acceleration through space [40].

Now that we motivated the currently favored model of pulsars being rapidly rotation neutron stars, we can have a look at the actual mechanisms that are causing the detected periodic emission. The emission model described in the following section forms the foundation on which models describing possible neutrino emission from pulsars are based on, so it is important to understand the basic

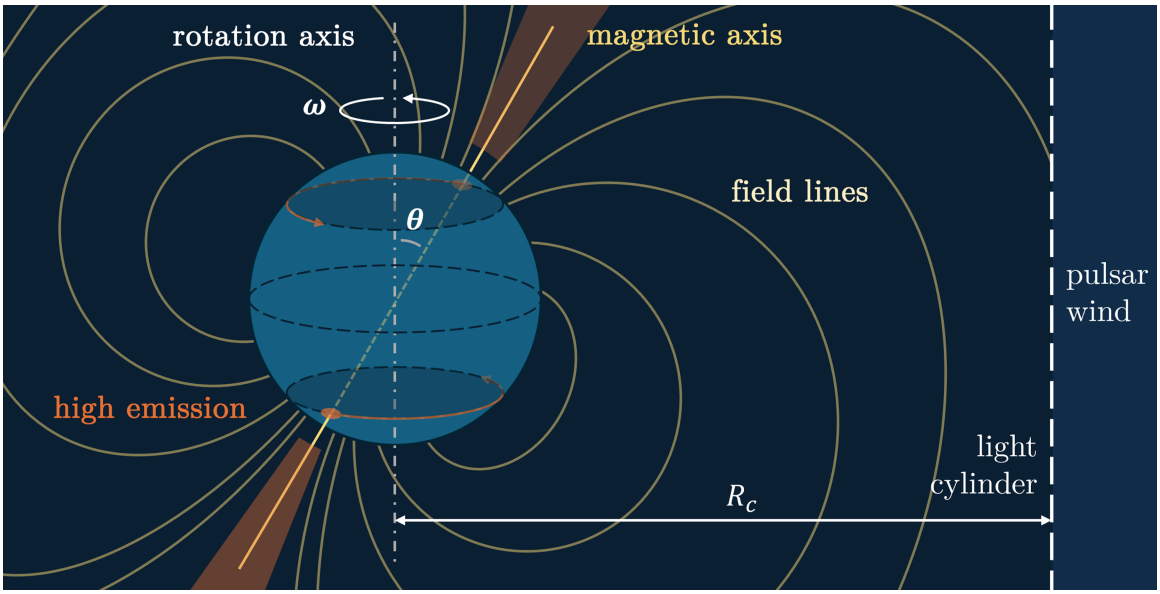

Figure 2.4: Schematic view of the pulsar lighthouse model: Rotation of the inclined magnetic axis and the high emission cones around and visualization of the magnetic field lines opening up when passing the light cylinder. Image made based on two visualizations by [10]

situation of how photon emission from those objects is thought to be taking place. Although there is still a lot of debate about detailed mechanisms by which these objects are emitting photon pulses over this wide energy range, a lot of observations and theoretical discourse support the theory that the magnetosphere rapidly co-rotating with the neutron star is playing a crucial role [10]. The magnetic field is in general not aligned with the axis of rotation, but the magnetic axis has some inclination to the rotation axis instead. This causes the magnetic axis to rotate along with the neutron star as shown in figure 2.4. The fast rotation of this strong dipole field generates a huge electromagnetic potential of the order of 10^{15} V for typical pulsar conditions. In the equatorial region this potential is shielded by the electrostatic field of the neutron star's charged particles. In the polar regions however, where the magnetic field lines penetrate the neutron star's surface, an intense electric field develops, which is capable of accelerating charged particles to high relativistic energies. The relativistic particles undergo cascades of pair production, forming a dense plasma above the polar regions. Besides the emission from this plasma, particles are also accelerated in a spiral around the magnetic field lines, emitting curvature and synchrotron radiation in the form of high-energy photons emitted in a narrow cone along the direction of movement, which can also re-interact with other particles emitted in the polar region, contributing to the pulsar's overall emission. As visualized in figure 2.4, charged particles following the rotation of the magnetic field lines coming from the polar regions would surpass the speed of light when reaching the light cylinder, where $\omega_{\text{Pulsar}} \cdot R_c = c$. This causes the field lines to open up and the particles following the magnetic field to be spun away, carrying the magnetic field in what is called a "pulsar wind", an ejection of charged particles accelerated to relativistic speeds [43]. All these emission effects are taking place in the regions above the magnetic poles and dominantly emit light or relativistic particles in a narrow cone around the magnetic axis. We can imagine that the magnetic axis and therefore the direction of high emission could by chance be pointing roughly along the line of sight towards Earth. The rotation of the

neutron star would cause this emission light cone to sweep over Earth once every rotation, resulting in the detected emission from this source to follow the characteristic pulsar profile as shown for the Crab Pulsar in figure 2.2. Because this sweeping of a light cone resembles the beacon from a lighthouse, this is also called the pulsar lighthouse model.

2.3 X-Ray Binaries

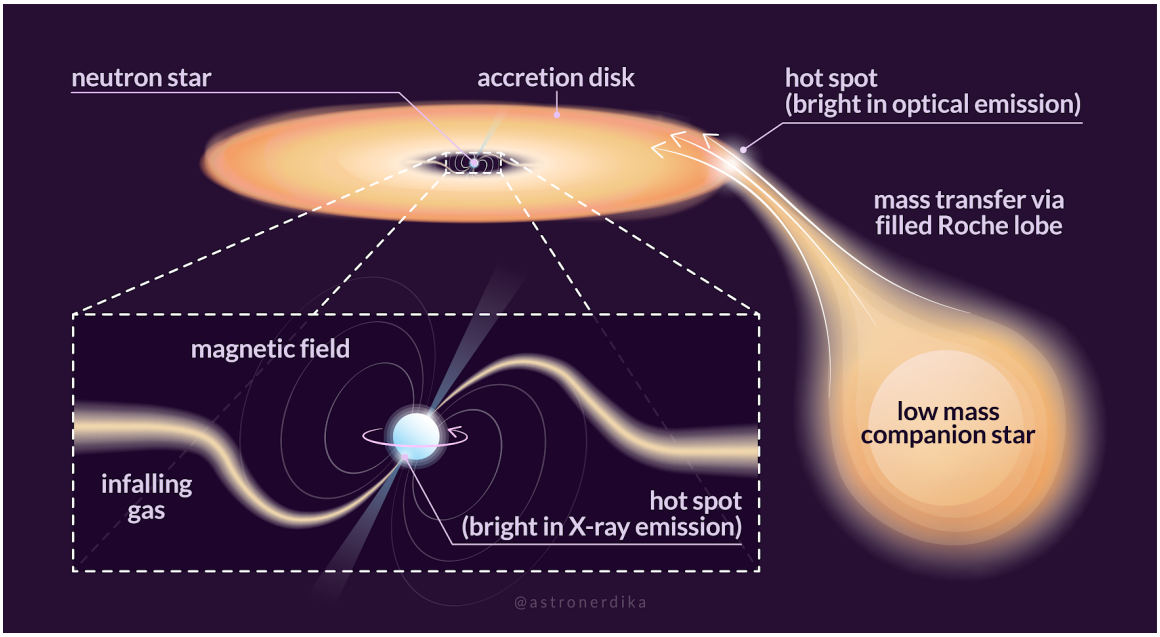

Figure 2.5: Sketch of an LMXB X-ray pulsar, kindly provided by [29]

Another special class of objects which are possibly able to produce periodic neutrino emission are the so-called X-ray binaries. These are close binary systems containing a neutron star and another stellar object in which the neutron star accretes matter from its companion star, causing very luminous emission in the X-ray band. The high luminosity in energetic X-rays makes them well suited for detection and the study of these systems' and their members' properties. Sco-1, the first X-ray source found outside of our solar system, which was discovered in 1962, is now known to be an X-ray binary system and, moreover, an X-ray pulsar. X-ray pulsars are special types of X-ray binaries, from which periodic emission is detected in the X-ray band, analogously to periodic signals from "normal" pulsars, which are mostly present in the radio band.

As is the case for classical pulsars, the periodic signal from X-ray pulsars we detect at Earth is based on the misalignment of the neutron star's magnetic field with its axis of rotation. However, in X-ray pulsars the emission is fueled by the companion star's matter falling onto the neutron star: for companion star masses with $M \lesssim 1M_{\odot}$ gas is pulled from the companion and forms an accretion disk up to a point around the neutron star, where the magnetic field is strong enough to channel the infalling matter towards the magnetic poles. For higher companion masses the mass transfer onto the neutron star happens mostly via the companions stellar winds. Regardless of how the material

found its way into the close influence of the neutron star's gravitation, it gets directed towards the magnetic poles, where the matter interacts with itself and ultimately with the neutron star and the nuclei and particles torn out of its surface, resulting in a hot plasma spot above each pole [10]. The different accretion situations dependent on the companion star's mass are categorized into high-mass X-ray binaries (HMXB) and low-mass X-ray binaries (LMXB). The process for the LMXB case is visualized in figure 2.5. Keep in mind that both objects are orbiting each other, also possibly in such a way that the cone of strong emission which is directed along the magnetic axis intersects the companion star or matter that is currently pulled towards the neutron star. The amount of accreted material needed to produce the observed very high luminosities in the X-rays is comparably low and can already be provided by stellar winds from the companion star reaching the influence of the neutron star and is not limited to systems where the neutron star is able to consistently pull away material of the companion [55]. The orbital motion of the binary system also has to be taken into account when analyzing the periodicity in the detected signal from a pulsar within a binary system. How this is applied in this analysis will be presented in section 3.5.3. Studying the deviations from the otherwise very stable signal emitted by the pulsar also allows to draw detailed information about the dynamics of the system if the stable pulse period is already known.

Note that the mechanisms by which radio and higher energetic emission of photons and charged particles in direction of the magnetic axis is produced in isolated pulsars are also at work in X-ray pulsars, but radio emission is suppressed by interactions with accreted matter and other effects, causing the detected radio emissions from X-ray pulsars to be less prominent than it is the case for ordinary pulsars [10]. Overall, the radiation of highly relativistic particles along the emission cone and the various possible interactions of high-energy protons that can produce neutrino emission make these objects very interesting candidates for the study of high-energy cosmic-ray and neutrino physics. In the following section a slightly more detailed view about possible neutrino production mechanisms resulting in a periodic flux of neutrinos from pulsars will be presented, followed by a summarized evaluation of the opportunities the study of such might present.

2.4 Neutrino Emission from Pulsars: State of Research

As described in section 1.4, neutrino emission is expected to arise from interactions of accelerated charged particles, prominently protons, with material or electromagnetic radiation in the pulsar environment. However, in addition to this general consensus, there is not much research investigating possible emission mechanisms in more detail. In the following, the results of some analyses dealing with possible neutrino emission from pulsars will be presented ([42],[41],[8], [2], [45],[58],[23]).

In their 2005 paper [42], Link and Burgio propose the acceleration of positive ions in young neutron stars that lead to the emission of beamed muon neutrinos through resonant scattering with x-rays emitted by the neutron star surface. Following the acceleration mechanisms of charged hadrons, the neutrino emission is expected to be directed along the pulsar's magnetic axis. The detection from such a source would show the same periodic behavior that can be observed in the measurements of electromagnetic emission. They predict an intense emission of neutrinos of $\sim 50\,\mathrm{TeV}$ energies that would make these objects one of the strongest neutrino sources within our galaxy, providing a high chance of detection. In 2006 [41], the authors published a corresponding paper including the prediction of count rates and flux spectra for neutrinos produced in this resonance in the Crab and Vela pulsar. The predicted spectra show a characteristic sharp rise due to the onset of the resonance

and then follow a power law with spectral index $\gamma = 2.0$ up to an upper energy cutoff, resulting in count rates of $10 - 100\,\mathrm{km}^{-2}\,\mathrm{yr}^{-1}$. The flux spectra for the Crab and Vela pulsar are shown in figure 2.6. We will later use these flux predictions to estimate the detection prospects of the current KM3NeT setup with respect to these flux spectra from Crab and Vela.

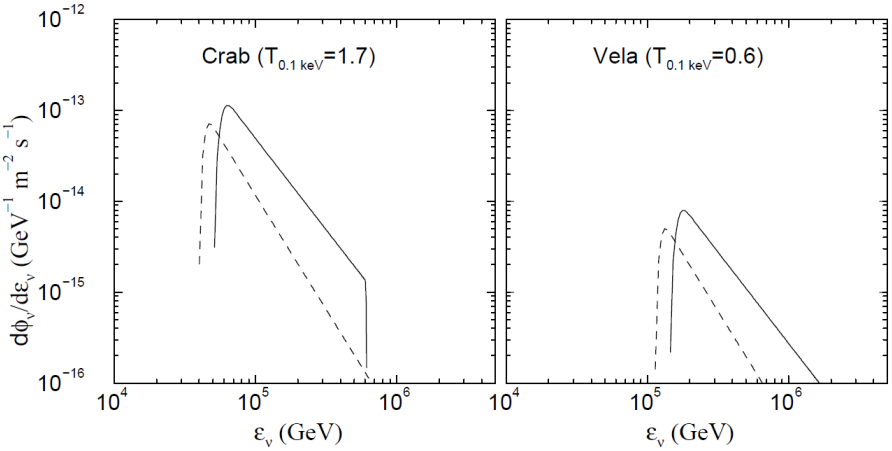

Figure 2.6: Predicted neutrino flux distribution per flavor for neutrinos from the Crab Pulsar (left) and Vela Pulsar (right) originating from resonant proton scattering with x-rays from surface of the companion star. Two cases of underlying proton acceleration are considered: Linear acceleration (solid line) and quadratic acceleration (dashed line). Taken from [41]

However, these flux predictions were criticized by Bhadra et al. in 2008 [8], for being strongly exaggerated due to wrong assumptions regarding the geometry of the hot spot above the magnetic poles, where the predicted resonance interactions are expected to take place. They propose new expected interaction rates, which are around four orders of magnitude lower than the ones predicted by Link and Burgio. The predicted detection rates are in the order of 1 event per km^2 in 100 years and would completely eradicate the detection possibility even with the newest generation of high-volume neutrino telescopes. The detection or non-detection of a periodic neutrino flux allows to evaluate the two models, if the sensitivity towards the detection of a periodic signal following the predicted flux is good enough.

In 2011 the IceCube Collaboration published a study on the search for periodic emission from various X-ray binaries based on around 2 years of observation from 2007 to 2009 [2]. The underlying analysis was a likelihood method, keeping the frequency for each source fixed at the one that is observed in photons and using the phase and duration of neutrino emission as free parameters. This showed an improvement in discovery potential compared to a time integrated search, in case the periodic emission is present about 20 % of the time. However, no evidence for periodic neutrino emission from the studied sources was found in the observed dataset. Notice, however, that this search was done using 22- and 40-string configurations of IceCube, leaving the option for a more sophisticated search using longer and more recent data.

In 2018, Mushtukov et al. [45] published their work, where they predict the emission of neutri-

nos in the low GeV range. They show that according to their models, the energy loss in certain ultra-luminous accretion states of X-ray pulsars is expected to be dominated by neutrino emission, similar to the situation in core collapse supernovae. This emission would also follow the periodic detection pattern seen in the X-rays. However, they state that the predicted neutrino flux from their example object ULX-1 NGC 5907 would still be too low for current neutrino detectors. In view of KM3NeT this might be a candidate for timing-based investigations with the single DOM response based "Supernova"-data [20] in the same way it was done by Eff and Gracia for ANTARES [25], [30].

Very recently, two works in the context of neutrino emission from pulsars have been published. In their paper published in June 2025, Xiao et al. [58] model the detection sensitivity towards neutrinos created in pp interactions of accelerated protons with pulsar winds and supernovae ejecta, which would be visible as neutrino pulsars. They furthermore investigate the prospects of analyzing pulsar characteristics such as the spin period or the magnetic field strengths of young pulsars. They suggest that with the new generation neutrino telescopes such as KM3NeT or IceCube-Gen2, not only the detection of these signals is possible, but one can furthermore expect to actually analyze source characteristics based on cosmic neutrino detection. This would be a milestone in the history of neutrino astronomy and physics in general. In August 2025 Ducci et al. [23] presented a work about the detection of neutrino emission from transient ultra-luminous X-ray pulsars. In contrary to Mushtukov et al. they describe another process of possible neutrino emission taking place during these states. They model the neutrino emission to arise from interactions of highly accelerated protons from the pulsar with protons in the accretion disk, which would also be visible as neutrino pulsar if the ejected proton beam is obscured by the accretion disk while sweeping over Earth. They propose that at high enough luminosities, the neutrino emission from transient X-ray sources might be detectable when they are close enough.

We can see that this is a promising field of study, where current developments in neutrino astronomy might enable many new and exciting discoveries in the near future. While there is still a lot of debate about how and at which rates neutrinos from compact objects might be produced, the study of these objects and the exploitation of possible periodic signals for an improved detection will surely provide numerous interesting research subjects for neutrino physicists.

3 Analysis Method

In this chapter, the data processing and statistical methods used in this analysis will be described. We will get to know all the processes needed to generate a time series of neutrino events associated with a given cosmic source, that can then be analyzed to search for possible periodic signals using the epoch folding method. Furthermore, it will be explained how the sensitivity study is conducted on the basis of the injection of simulated signals modeling the expected emission from pulsars and X-ray binaries.

3.1 Source Overview

Cherenkov neutrino detectors continuously measure the neutrino interaction events inside or close to the detector volume, independently of the neutrino's direction. This means that in theory we can investigate the neutrino flux coming from every source direction we want by only selecting events that are coming from where a source of choice is located at any given time. This analysis was built to be able to freely select the source by providing a simple source file, which stores information about the source coordinates, the source name, the pulsar frequency and potentially the orbital parameters of the binary system. Step by step this information is used to select events associated with our source (see section 3.4), applies the corresponding timing corrections (see section 3.5.3) and searches for the frequency in the selected data by applying the epoch folding (see section 3.5.1). To study the sensitivity of this analysis, two exemplary sources are used: the X-ray binary Vela X-1 ("vela") and the Crab Pulsar ("crab"). These sources are chosen because one can compare the results to the flux predictions done by [41] and also because they are in general two very well studied and bright pulsar sources. They are also differently orientated in the sky as seen from the KM3NeT detectors, which allows us to investigate how this could be used to also analyze sources that are mostly visible above the horizon with this frequency analysis. Table 3.1 shows the location, distance and pulse period for both sources.

Source	Right Ascension	Declination	Distance	Pulse Period
Vela Pulsar	135.5286 deg	−40.5547 deg	6600 ly	89 ms
Crab Pulsar	83.5125 deg	+22.0145 deg	6200 ly	33 ms

Table 3.1: Overview over the sources that are investigated in the sensitivity study. Information taken from [38] and [11]

3.2 Data Overview

Although no real data is analyzed to search for possible periodic signals, the whole workflow was still built to work with real KM3NeT data in the form it can be obtained from the official KM3NeT data storage units. Furthermore, the time shuffled data was used to serve as background in our sensitivity study. This aims at a realistic representation of the expected event distribution that is measured with the current detector setups. For the analysis we use data from the ARCA21 (21/230

planed detection units) and ORCA18 (18/115 planed detection units) detector configurations. For ORCA the `v9.0` and for ARCA the `v9.2` runs were used. Table 3.2 gives an overview about the runs used for the analysis and figure 3.1 shows the lightcurves of the background data sets for ORCA and ARCA selected with a maximum search cone angle of 30 deg around Vela and Crab.

Detector	First Run	Last Run	t_{min}	t_{max}	Number of Runs
ORCA	16521	18298	1682933409.1 s (2023-05-01)	1693526400.1 s (2023-09-01)	875
ARCA	15271	17662	1680663678.6 s (2023-04-05)	1694422674.5 s (2023-09-11)	1214

Table 3.2: Overview over the data used as background for the sensitivity study

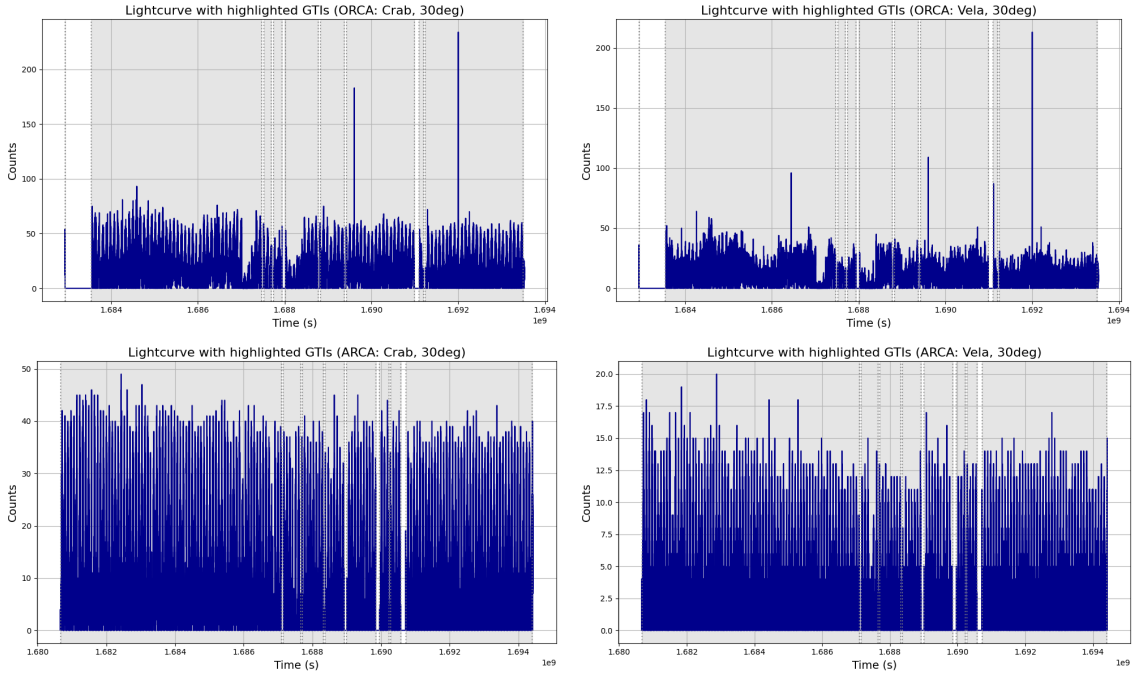

Figure 3.1: Lightcurves of the selected background sets for maximum search cone angle of 30 degrees for Crab (left) and Vela (right) with higlighted GTIs. Upper plots ORCA, lower plots ARCA

3.3 Preprocessing

Before we can allocate interaction events in the detector volume to neutrinos originating from a certain source and conduct a periodic timing analysis, a number of preprocessing steps have to be applied. These will be presented in more detail in the following section. In general, the goal is to

provide a timeseries that stores the events associated with the chosen source. The arrival times of all events included in this final set will be used as the underlying timeseries for the epoch folding analysis that will show whether a certain test frequency is present in the final timeseries or not. In order to create this, the KM3NeT files have to be blinded and the relevant information for this analysis has to be extracted and combined. The angular uncertainties of the reconstructions have to be calculated and the events need to be classified regarding their underlying interaction type (track/shower). This information is then used to decide which events are thought to be possibly originating from the source location and should be included into the timing analysis as will be explained in the next section.

3.3.1 Data Reduction and Blinding

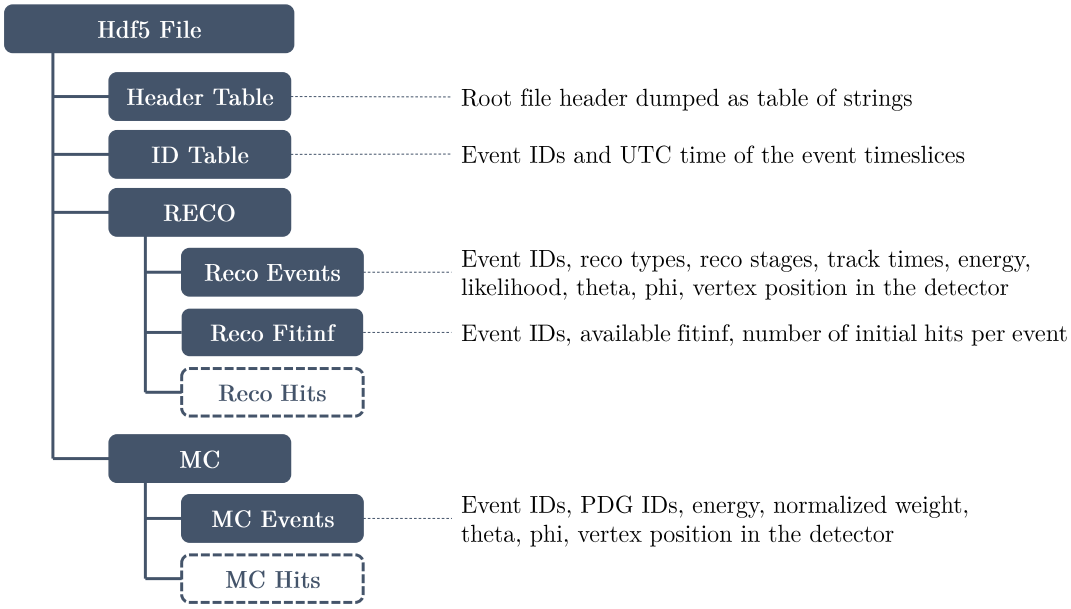

Figure 3.2: Overview of the contents stored after the data reduction. The individual tables are `astropy.tables.Table` objects. The dashed fields represent tables for storing hit information associated with each event, which might be added in the future.

The first step in the analysis is to convert the data files from the `root` based KM3NeT data format to a more astronomy-friendly high-level data format that is compatible with the widely used `astropy` library. More specifically, `astropy Table` objects are stored, which are well suited for usage in astronomical analyses, allowing for different time formats and coordinate systems to be easily accessed and converted. This is done using the designated `km3astro` python package, which deals with astronomy applications within KM3NeT. An i/o-module called `km3astro.io` was written for this work, which extracts high-level information from the km3net monte-carlo and data files to streamline the handling of multiple data files for astronomy purposes. The module contains functions to access

relevant information of the best track and shower reconstructions and to calculate some information that is often needed but not directly available from the root files [14].

The files are first loaded using the `km3io.offline.OfflineReader` and the best reconstructions are found based on the `km3io.tools` module's `best_jmuon` and `best_aashower` or `best_jshower` functions, which search for the best fit of each reconstruction type if they are available. `jmuon` and `jshower` denote the track and shower reconstructions from KM3NeT's `jpp` framework, whereas `aashower` is the shower reconstruction from the `aanet` framework. For each event, the best fit of each available reconstruction is found based on the corresponding fit likelihood. The spherical coordinates of the reconstructed neutrino direction as well as the reconstructed interaction time are calculated and stored, together with a unique id for each event that allows to keep track of it. An hdf5 file is created for each km3net file, which contains those tables as it is sketched in figure 3.2. The `km3astro.io.load_hdf_tables` function provides easy loading of those files.

In order not to influence the analysis workflow underlying this work by optimizing it based on what we can see in the data, the crucial information in the data is hidden or "blinded". This is done by randomly shuffling the reconstructed neutrino directions ϕ_{reco} and θ_{reco} as well as the reconstructed time t_{reco} within each run. This randomizes the data, so that the analysis would not show a periodic signal coming from a source, even if there was one present in the dataset.

3.3.2 Angular Error Estimation

In order to be able to tell whether an event is associated with a certain source or not, we need to know how well the reconstructed direction is expected to be. However, it is not possible to know with certainty what is the error regarding the reconstructed directions and energies of events in the real data, because we do not know what the true directions and energies of the detected events are. To bypass this inconvenience, we estimate the angular error of real events by using the angular error distribution from simulated events, where both the true and reconstructed directions are available. Because of this, the angular error is calculated for a large number of simulated events, which are then binned over the reconstructed energy of each event. This allows us to estimate the angular error for each event in the data files using its reconstructed energy. Because both KM3NeT detectors behave differently when it comes to reconstructing detected events due to their different detector geometry and also the reconstruction is done once under the premise of the event being a track-like interaction and once for a shower-like interaction, we will calculate the energy-dependent angular error estimate four times in total.

The angular error distributions shown in figures 3.3 and 3.4 are then used to calculate an angular error estimate for each event from the data files using a function that interpolates between the calculated mean angular errors and allows to calculate an error based on the reconstructed energy for each event. In section 3.4 we will see how this angular error estimate is used to decide whether an event is associated to the chosen source of interest and is kept for the timing analysis or not.

We can see that for the used setup of the ARCA detector there is a very strong difference in the angular resolution of the track and shower reconstructions. The `jmuon` reconstruction shows a very good resolution, with angular errors better than 2 degrees, approaching 0.01 degrees for higher energies. The `aashower` reconstruction on the other hand shows errors generally above 15

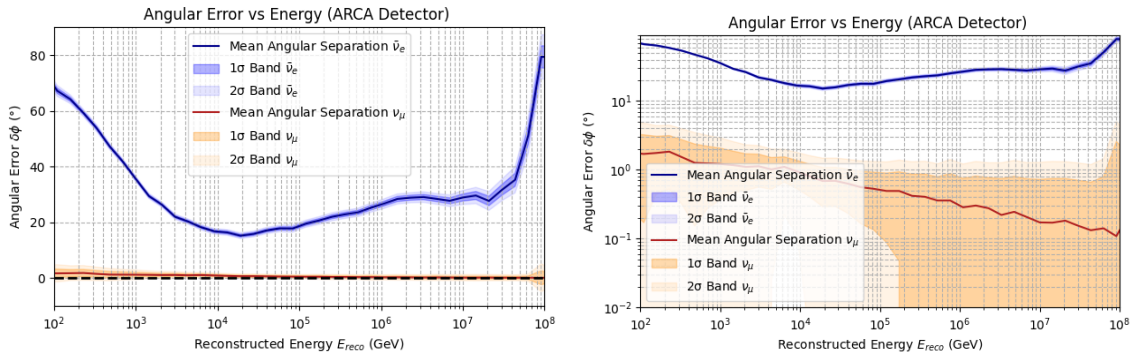

Figure 3.3: ARCA detector: Distribution of the angular error between MC true and reconstructed neutrino direction. Binned over the reconstructed energy, shown for the energy range from 100 GeV to 100 PeV. Track reconstruction using `jmuon` shown in orange (78556 events), shower reconstruction using `aashower` in blue (132676 events). Linear y-axis on the left and logarithmic on the right.

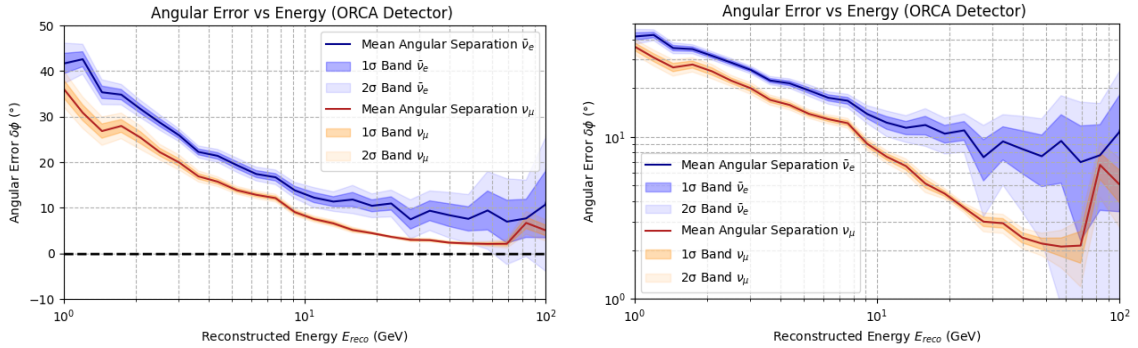

Figure 3.4: ORCA detector: Distribution of the angular error between MC true and reconstructed neutrino direction. Binned over the reconstructed energy, shown for the energy range from 1 GeV to 100 GeV. Track reconstruction using `jmuon` shown in orange (30768 events), shower reconstruction using `jshower` in blue (11175 events). Linear y-axis on the left and logarithmic on the right.

degrees, reaching errors above 60 degrees at the low and high end of ARCA's optimized energy range from 100 GeV to 100 PeV. This shows the remaining difficulties for point source analyses using shower-like events with ARCA. For the ORCA detector configuration, the difference between the track and shower reconstruction is a lot more subtle, with the `jshower` reconstruction having approximately a 5 degree higher angular error across ORCA's energy range from 1 GeV to 100 GeV. Both reconstructions show an angular error in the range of 40 degrees at the low end of the spectrum, gradually approaching 3 degrees or, respectively, 8 degrees towards the high energies. For higher energies outside ORCA's optimized energy range, the angular resolution gets much worse again.

3.3.3 Track/Shower Classification

As we have seen before, the KM3NeT reconstruction chain uses different reconstruction algorithms for the different event types *track* or *shower*. All triggered events are being processed with both algorithms, which results in most of the events having energy and direction solutions for both hypotheses. For some events only one algorithm works, as the detection pattern is differing too much from what would be expected under the assumption of a track or a shower interaction to meaningfully fit the corresponding reconstructions to the hits data. Now, if we have two working reconstructions for a given event, we have to decide which one to use. This means we have to decide whether the hit pattern associated with an event is more compatible with a track-like or shower-like signature. Therefore, we will use the `newhitfeatures` and `paramPID` frameworks that were developed by the KM3NeT group at ECAP. In combination, the packages allow for the training and application of a machine learning algorithm for parameter-based particle identification.

The `newhitfeatures` package is designed to prepare the KM3NeT files (both MC and data) for the following training or classification process by extracting important features for each event that serve as training parameters. After those features are extracted, the `paramPID` package can be used to train a classifier based on the MC files, which can then be applied to the data files. For each event this calculates a track-score, which gives the probability of the event being track instead of shower-like, meaning a track-score close to 0 would be a certain shower-like event, whereas a track-score close to 1 characterizes the event to be certainly track-like.

During the development of this thesis it was observed, that `paramPID` and `newhitfeatures` are not compatible with the latest versions of the data and MC files. In order to apply the described analysis correctly to real data this needed to be fixed first. To account for this in the sensitivity study, a fixed fraction of the modeled events is artificially misclassified before they are injected into the background set. Since the classification is not working, we randomly assign a track score between 0 and 1 to the detected events in the data set, simulating a detection accuracy of 50 %. To account for this randomness in the classification, the modeled events will also be randomly classified by processing half of the expected events from a certain interaction type with the "wrong" reconstruction.

The event classification will be used to decide which reconstructed information will be used for the further analysis. If both reconstructions are present for an event, the best-fit track reconstruction is used if the event's track score is above the threshold of 0.5, otherwise the best-fit shower reconstruction is used. If only one reconstruction is available, this will be used. This means, that after the reconstruction we have one single event set containing all the information we need: Reconstructed energy, reconstructed direction, reconstructed interaction time and the fit parameters of the corresponding reconstruction, such as the fit likelihood or the number of hits for each event.

3.4 Event Selection

Having the data converted with `km3astro.io`, the angular uncertainty calculated from the MC files and the track/shower classification applied using `paramPID`, the data selection can be applied. This will determine which events will be used for the epoch folding analysis. First, the events associated with a chosen source are found and then data quality cuts are applied to reduce background influences.

3.4.1 Source Correlation

To select the events that are included in our analysis, we need to identify whether they might be coming from the source or not. This is done by estimating the angular uncertainty for each event based on its reconstructed energy and reconstruction type as explained in section 3.3.2. We can calculate the angular distance to the source and compare it with the angular error for the corresponding energy. Based on this comparison we can filter out events that have a high probability of not coming from the source. In order to not include too many events with high angular error and therefore randomly reconstructed directions, we will set a maximum allowed distance to the source. We can later have a look at how the sensitivity of our analysis is affected by changes in the maximum selection angle and we can also check the classical selection case, where all events within a certain distance around the source are used. The following equation defines the selection cone that is used for a chosen source.

$$\alpha_{\text{select}}(E_{\text{reco}}) = \sqrt{\min\left[(\Delta\varphi_{\text{reco}}(E_{\text{reco}}))^2, (\Delta\varphi_{\text{max}}))^2\right] + (\Delta\varphi_{\text{source}})^2} \tag{3.1}$$

The errors regarding the source location are generally very low. ESA's Hipparcos space astrometry catalogue for example has an angular uncertainty regarding an object's coordinates of $\sigma_\alpha = 0.77\,\text{mas}$ and $\sigma_\alpha = 0.77\,\text{mas}$ [48]. These uncertainties regarding the source position are in the order of 2×10^{-7} degrees, which is so much smaller than our angular reconstruction uncertainties, that they can safely be ignored.

3.4.2 Quality Cuts

The last step before applying the timing analysis are the data quality cuts, which have the general goal of reducing the influence of background data to minimize the signal to noise ratio and to get rid of badly reconstructed events. The first low level noise reduction is done by applying the following cut criteria, following the general approach in neutrino astronomy with KM3NeT [24].

- Likelihood: `lik > 50`
- Number of Hits: `n_hits > 20`
- Energy: `E_reco > 0`

This eliminates noise events that are not really coming from a neutrino interaction and also badly reconstructed events. Further cuts are then used to reduce unwanted events, with the most important one being the zenith angle cut, which omits events based on their direction in the local detector frame. The main reason why this is done is to reduce the high atmospheric muon contamination. One often constrains the analysis towards events coming from below the horizon, because muons get absorbed when propagating through the Earth and therefore one can expect to completely cut them out by looking only at upgoing events. We will investigate later how the choice of a zenith threshold allows us to increase the sensitivity of our data.

3.5 Timing Analysis

In this section, we will describe the algorithms and statistical methods used in our timing analysis. The epoch folding algorithm on which the periodicity search in this analysis is based will be presented. The concept of good time intervals gets introduced and the timing correction that is necessary when dealing with periodic emission coming from cosmic objects will be explained.

3.5.1 Epoch Folding

Epoch folding is one of many algorithms for searching periodicities in time series data and can be used for sets of event detection times (as it is the case in KM3NeT) as well as lightcurve data that stores detection rates per time bin. It is widely used in pulsar astronomy and most of the depictions of pulse measurements, like the one in shown in figure 2.2, are based on this algorithm. In general, the concept of epoch folding is quite simple and probably best understood when looking at the illustration in figure 3.5. A timeseries dataset is split into intervals of the same length and all intervals are added up, summing the events from every interval for a given relative time bin inside the intervals. Because these relative time bins each correspond to a phase of a pulsation if it is found, they are also referred to as phase bins. If the width of the interval does not correspond to the period of any periodic elements in the dataset, this will simply sum up random data in all phase bins, resulting in a flat distribution of summed counts throughout the interval phase. However, if the period of a actually present frequency is used as the interval width, this causes the emission arising from this to line up in the same phase bin in each interval. This results in a strong peak in certain phase bins in the summed phase histogram. For each histogram, a χ^2-test against the background hypothesis is performed, which yields the highest results in the case where the chosen interval width lines up the best with the signal period. To better fit this to the use case, one rather defines test frequencies and calculates the χ^2 against a background hypothesis for each interval width that corresponds to this frequency and then looks at the χ^2 distribution. If a frequency is present, this appears as a peak in the χ^2 distribution at the corresponding test frequency [9].

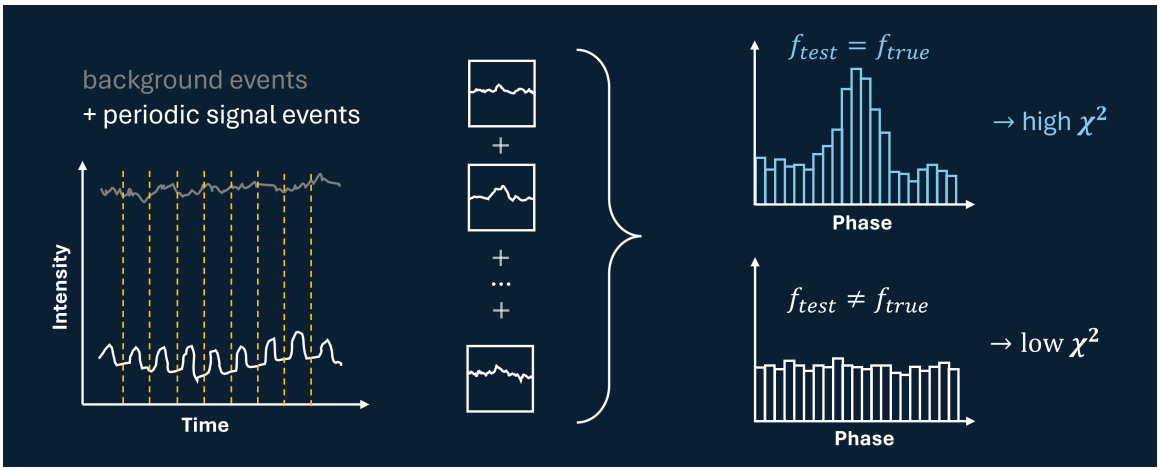

Figure 3.5: Illustration of the epoch folding algorithm. For each histogram a χ^2-test is performed, to check the result of the current interval choice against the background hypothesis of a flat spectrum. If a periodicity is present in the data this yields high χ^2 values when using interval widths close to the period of the signal. Illustration made based on the examples with real data shown in [54].

Mathematically speaking, the epoch folding operation is the following. The dataset is cut into intervals of length P_{test} and for each of the N phase bin the number of events x_j from each interval contributing to the corresponding bin is added. For a given bin i this yields a normalized number

of event counts for this bin H_i.

$$H_i = c_i \sum_{j=0}^{M} x_j \text{ with } x_j = \begin{cases} 1, & i/N < \varphi < (i+1)/N \\ 0, & \text{otherwise} \end{cases} \tag{3.2}$$

Where $\varphi = (t \mod P_{\text{test}})/P_{\text{test}}$ is the relative interval phase of an event and c_i a normalization factor, taking into account the length of the test periods and the total exposure within the given phase bin. For a given test period, each bin can be tested against the expected background distribution and a χ^2 test can be performed to evaluate how strongly the folding result deviates from the null hypothesis [9].

$$\chi^2 = \sum_{i=0}^{n-1} \frac{(H_i - \langle H \rangle)^2}{\sigma_i^2} \tag{3.3}$$

Here, $\langle H \rangle$ is the averaged profile, which corresponds to the background expectation, H_i the normalized event count for the i-th bin from above and σ^2 is the standard deviation of the corresponding pulse histogram, based on a random distribution. The higher χ^2, the more the background hypothesis is violated for a chosen test period. To evaluate the significance of this violation in a quantitative way, the so called p-Value will be used. This value is a measure for the probability of seeing a χ^2_{obs} under the premise of the null hypothesis H_0 being true. This means that the smaller this value is, the higher the probability of the measured χ^2_{obs} to actually arise from a certain signal and is not just a statistical fluctuation [61]. Following the general consensus within the field of particle physics will use the threshold p-Value of $p = 2.87 \times 10^{-7}$, which corresponds to a 5σ detection of the signal. The χ^2 threshold that corresponds to this p-Value can be calculated based on the degrees of freedom in the final χ^2 search, which is given as the number of bins in the folded pulse profiles minus one (d.o.f. = nbins − 1). For our analysis with 32 bins, we use a threshold of $\chi^2_{\text{threshold}} \approx 87.4$.

Figure 3.6 shows the resulting phase histograms for two different modeled $\kappa = 5$ MVMD signals, once with a low baseline offset ($b = 1$) and a high baseline offset ($b = 100$). While the detection is much clearer in the low background case, we are still able to detect the frequency in the modeled set also for $b = 100$. The MVMD distribution will be presented in more detail in section 3.6.6. Figure 3.7 shows the χ^2 distributions around the true frequency for the two models.

To apply this folding operation in practice, we can use the pulsar search utility provided by the `stingray` package. It allows us to easily run the previously described calculations for any time series dataset and a chosen test frequency. Multiple trial frequencies around the test frequency in question are checked, the χ^2 test is performed and the results for each frequency are stored. The maximum χ^2 value corresponding to the most present frequency gives a measure of how significantly this frequency was detected in the data [36].

3.5.2 Good Time Intervals

A common problem when analyzing time series data is the presence of periods in the dataset, where the detector was working not properly and the data is either not at all or wrongly recorded. These gaps in the valid dataset pose problems for other frequency analysis algorithms, such as the fast Fourier transform (FFT), but can very easily be dealt with in the case of epoch folding. This can be done in a very straightforward way by providing the so-called good time intervals (GTIs) to the `stingray` epoch folding search. As the name suggests, the GTIs store information about the timing

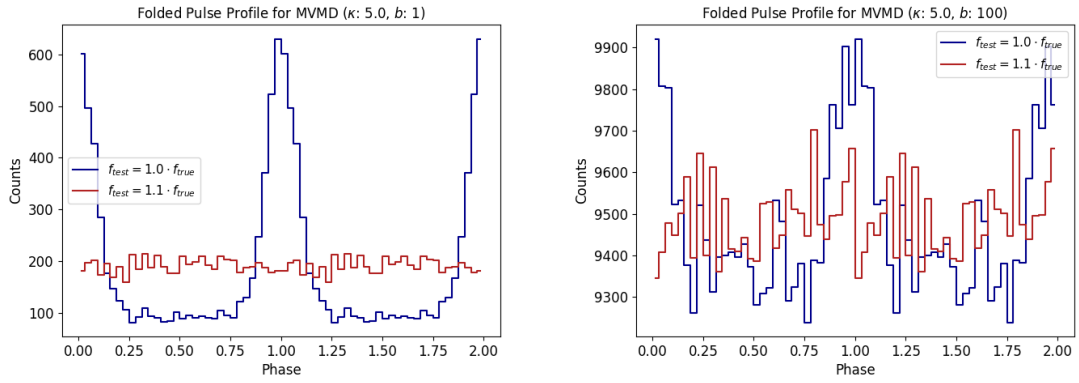

Figure 3.6: Folded pulse profiles for two pulse models using a a MVMD pulse model with different baseline offsets. The offset can be interpreted as nonperiodic background to the periodic signal.

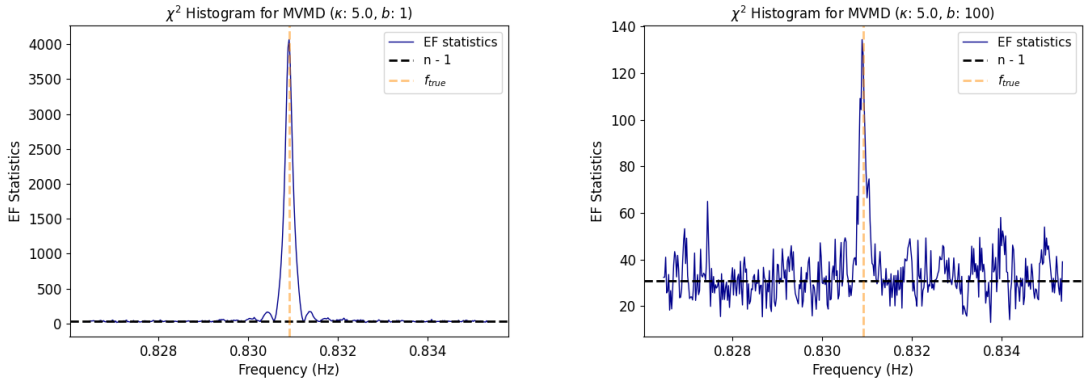

Figure 3.7: χ^2 histograms for the two pulse models shown in figure 3.6.

intervals in which the detector was working correctly and uninterrupted valid data was taken. This is implemented in the analysis chain for this work by checking each input file and combining this information during the preprocessing. This ensures that no artifacts in the epoch folding search arise from possible data gaps. The data overview in figure 3.1 shows the respective GTIs that were used for both sets.

3.5.3 Timing Correction

An important step in pulsar timing analyses deals with relating the observed time of arrival of a signal to the actual time of emission at the pulsar. More importantly for the analysis presented in this work is the correction of possible deviations from a true periodic signal produced at a pulsar that arises in the observed arrival times due to the movement of the Earth with respect to a source. As we learned in the previous subsection, the epoch folding algorithm used for the timing analysis in this work is designed to simply detect the presence of a roughly known periodic signal in a time

series dataset. While one could imagine that for signals with pulse periods of a few milliseconds, the movement of the Earth is too small in these time periods, the effect still comes into play when looking at data spanning over a large enough time scale. Due to the low detection rates of cosmic neutrinos, analyzing datasets over a long time scale is essential and therefore also the correction of the arrival times plays an important role for a successful detection of periodic neutrino signals from cosmic sources.

This so-called barycentric correction is applied by transforming the measured arrival times to the theoretical times one would expect at the barycenter of the solar system for a chosen source. The barycenter is the gravitational center of the solar system, around which the objects in the solar system revolve. By analyzing the expected arrival times at the barycenter instead of at Earth, the true periodicity present in a signal is not altered from arrival time shifts due to the Earth's movement. In the case of X-ray binaries, effects coming from the movement of the pulsar in the binary system have to also be taken into account in a similar manner. These corrections were already implemented for a study with ANTARES data [39]. These implementations were included into the workflow and are in principle ready to be applied to the KM3NeT epoch folding analysis as well. Since no real data is analyzed regarding the existence of periodic signals in this work, these corrections will not be applied, because the periodic timing model does not include the modeling of distortions in the expected arrival times according to the movement of the Earth.

3.6 Sensitivity Study

A main part of this work deals with estimating the sensitivity of KM3NeT to periodic neutrino signals emitted by selected sources with the timing analysis approach just presented. The general idea is to inject simulated signals into the blinded data set which are supposed to mimic the expected detected and reconstructed events resulting from a certain physical flux emitted by that source and then apply the timing analysis to the new set. In order to evaluate the performance of the analysis as a function of the astrophysical neutrino flux, we have to precisely model how many events and in which energy distribution we expect to be detected for any given situation. The response to the energy reconstruction is simulated and the expected origins of the events will be modeled based on the energy and particle type according to the previously presented angular resolutions. Finally the periodic timing of the signal is simulated and the signal and background sets are merged. The processing steps for the signal modeling can roughly be divided into the following steps:

1. Calculate effective detector area $A_{\text{eff}}(E, \theta)$ for each flavor
2. Model physical flux expected at the detector $\Phi_\nu(E, \theta, \phi)$ for each flavor
3. Calculate overall expected event detection $N(E)$ for the given A_{eff}-Φ_ν combination
4. Model energy reconstruction response $E \rightarrow E_{\text{reco}}$
5. Simulate event origin θ_ν , $\phi_\nu = \theta_{\text{source}} + \delta(E)$, $\phi_{\text{source}} + \delta(E)$
6. Model timing information
7. Inject into the background set

We will now have a detailed look at each part of this analysis chain.

3.6.1 Calculating the Effective Area

The first crucial step in simulating expected neutrino events is the estimation of the detector's effective area, which gives the connection between the present flux and the expected event detection. The average effective area A_{eff} for a certain bin of energy dE and solid angle $d\Omega$ is defined as:

$$A_{\text{eff}} = \frac{N}{\int_{\text{bin}} \Phi(E) dE \, d\Omega} \tag{3.4}$$

This is the number of detected events N over the integrated flux $\Phi(E)$ for a given energy and solid angle bin. In KM3NeT, we can calculate the effective area for a detector configuration based on the corresponding Monte Carlo simulation runs by accessing the weights that are produced for each event during the simulation. These event weights correspond to the event rate per unit flux and are provided from the neutrino generator (in our case: gSeaGen) to allow for easy rescaling of the simulated neutrino events to any given flux. The event rate normalization 1/n _gen_events is stored together with each event weight w, allowing to combine simulations from multiple runs and different flavors. Using this information, we can calculate the effective area from the simulated events for a given energy and zenith angle bin as follows:

$$A_{\text{eff}} = \frac{(1-\gamma)}{d\omega \, dE} \cdot \sum_i \frac{w_i E_i^{-\gamma}}{n_{\text{gen\_run}}} \tag{3.5}$$

The spectral index γ characterizes the steepness of the flux spectrum, $dE = E_{\text{k+1}}^{1-\gamma} - E_{\text{k}}^{1-\gamma}$ the width of the corresponding energy bin and $d\omega$ the width of the corresponding zenith angle bin, defined as $d\omega = 2\pi \cdot (\cos\theta_{\text{i+1}} - \cos\theta_{\text{i}})$. This comes from the binning in terms of $\cos\theta$ instead of θ directly, which is done to distribute events regarding their arrival directions in a more realistic way. In figure 3.8 we can see the 1D effective areas for ORCA (energy range $1 - 10^2$ GeV) and ARCA (energy range $10^2 - 10^8$ GeV) for each particle type.

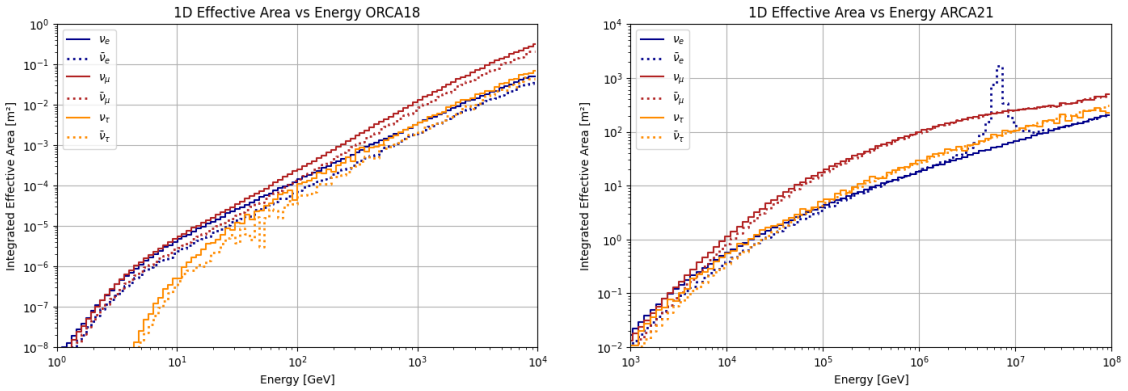

Figure 3.8: 1D effective areas over neutrino energy for each particle type for ORCA (left) and ARCA (right). The 1D area over energy shows the mean effective area per energy bin from the calculated 2D area used for the calculation of expected neutrino events

The strong peak in the $\bar{\nu}_{\text{e}}$ detection rate at 6.3 PeV is due to the Glashow-resonance, an enlarged cross section for $\bar{\nu}_{\text{e}} - \text{e}^-$ interactions caused by the formation of a W^- boson. Generally, the highest

detection response is expected to arise from the ν_μ and $\bar{\nu}_\mu$ flux for energies above 10^2 GeV, which highlights the importance of muon neutrinos and antineutrinos for detecting high-energy neutrinos with KM3NeT. While the effective area over energy bins is a good way to show the general detector response in a fast and comparable way, the actual calculation of the expected detected events is done based on the 2D effective area, where we also distinguish the events based on the zenith direction of the detected neutrinos. Since we are simulating the response to a point-like source, this allows us to model the emission situation more precisely. Figure 3.9 shows the 2D effective area binned over energy and direction for ORCA and ARCA for ν_e, $\bar{\nu}_\mathrm{e}$, ν_μ and $\bar{\nu}_\mu$.

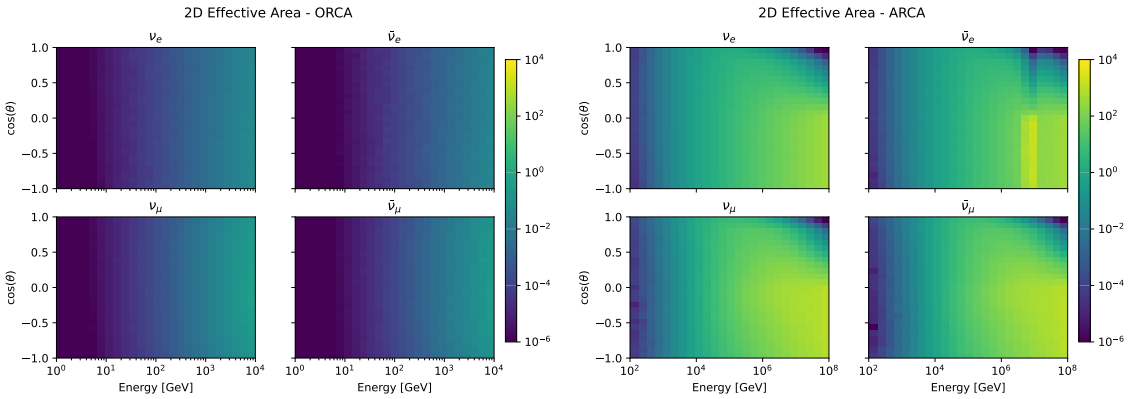

Figure 3.9: 2D effective area of ORCA and ARCA calculated from `mcv9.0` monte carlo files, plotted for the same colorbar. ORCA: $1 - 10^4$ GeV, ARCA: $10^2 - 10^8$ GeV, 25 energy bins each

We see that the 2D effective areas for ORCA do not show any notable features but simply rise with higher energies more or less uniformly spread over the angular range. For ARCA on the other hand, we see a strong angular dependence for high-energy neutrinos, where upgoing neutrinos that already traversed earth show a much lower amount of detected events from the same flux, due to a higher chance of neutrino-nucleus interactions already happening before a neutrino reaches the detection volume. In the range of the Glashow resonance, we also expect to detect less events from upgoing electron antineutrinos, since the higher interaction probability during the traversion of Earth changes the expected surviving flux in the detector. Notice, that the new simulation runs of ARCA21 are done with `mcv9.0`, which shows some changes in the effective area compared to older versions. In figure 3.10 you can see the effective areas for ν_μ and $\bar{\nu}_\mathrm{e}$ calculated based on runs from `mcv9.0` and `mcv8.1`, showing the most notable differences between both versions.

3.6.2 Modeling Physical Flux

The physical flux present at Earth originating from a possible periodic neutrino emitter will be modeled in two different ways. The first one will be a classic power law flux for a point-like source, where the energy is normalized to a certain reference energy E_0. This is done to fix the flux at this energy to the flux normalization ($\Phi(E_0) = \Phi_0$), which can be helpful when modeling more detailed flux distributions in some given energy range.

$$\Phi_{\mathrm{classic}}(E) = \Phi_0 \cdot \left(\frac{E}{E_0}\right)^{-\gamma} \tag{3.6}$$

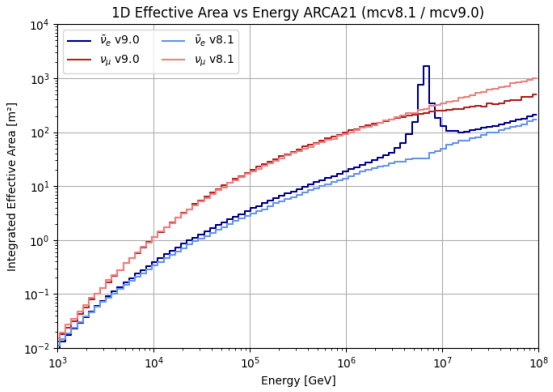

Figure 3.10: 1D effective areas over neutrino energy for each particle type for ARCA21 `mcv8.1` and `mcv9.0`

The second flux model corresponds to the same power-law spectrum, but with a hard energy range restriction such that it vanishes outside $[E_{\min}, E_{\max}]$:

$$\Phi_{\text{bounded}}(E) = \begin{cases} \Phi_{\text{classic}}(E), & E_{\min} \leq E \leq E_{\max} \\ 0, & \text{otherwise} \end{cases} \tag{3.7}$$

Note that the units of the flux normalization and therefore also the calculated flux are $[\text{GeV}^{-1}\,\text{m}^{-2}\,\text{s}^{-1}]$, which makes it easy to use for our case of GeV energies and our effective area in m^2. To improve the readability this unit is partly not written when specifying some flux normalizations used in the analysis especially in image captions or titles. However, you can assume the flux to always be in these units if not otherwise specified.

Classic Power Law Flux

The classic unbounded power-law flux is used as a measure for comparison, to put our result into a broader perspective for other astrophysicists. Power laws are a common feature in high-energy astrophysics arising naturally from a number of acceleration and interaction mechanisms, making it a universally used baseline model for simulating high-energy particle fluxes. In addition to that, the detector response to such a generic and featureless flux distribution allows us to isolate the effects that are introduced from the sharp energy-cutoff features in the bounded model. For the classic power law flux a reference energy of $E_0 = 1\,\text{GeV}$ is used. The reason for this is to have a more intuitive understanding of how the flux changes with the variation of Φ_0 and γ. In this way, the flux at the low boundary of the energy range KM3NeT is sensitive to is defined by the flux normalization and with a higher spectral index we expect a steeper fall off relative to lower gammas. Two examples of this distribution from $1\,\text{GeV}$ to $1 \times 10^8\,\text{GeV}$ are shown in figure 3.11.

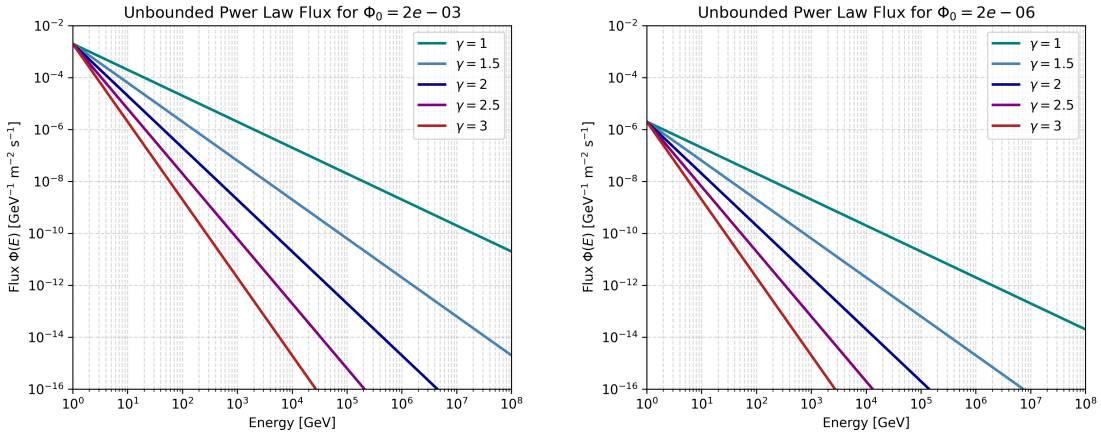

Figure 3.11: Modeled unbounded power law flux with $E_0 = 1\,\mathrm{GeV}$ for different spectral indices γ. *Left:* $\Phi_0 = 2 \times 10^{-3}\,\mathrm{GeV}^{-1}\,\mathrm{m}^{-2}\,\mathrm{s}^{-1}$ *Right:* $\Phi_0 = 2 \times 10^{-6}\,\mathrm{GeV}^{-1}\,\mathrm{m}^{-2}\,\mathrm{s}^{-1}$

Bounded Power Law Flux

The bounded power-law flux is motivated by the work of [41], which predicts the periodic emission of high-energy neutrinos from a well defined energy interval. As we learned in section 2.4, this is due to an energy threshold necessary to be overcome for the underlying neutrino production mechanisms and a high-energy cut-off due to either interaction kinematics or limitation in proton acceleration. In order to test the sensitivity of KM3NeT to this predicted flux, we will investigate the responses to different flux intensities of the bounded power-law type. We will model the bounded flux in a way that the shape corresponds to the two flux distributions expected from the Crab and Vela Pulsar presented in [41] and use fixed boundary values for each source. We will then vary the flux normalization Φ_0 and the spectral index γ to investigate how the sensitivity of our detectors depends on these two parameters. The lower boundary will be used as the reference energy ($E_0 = E_{\mathrm{min}}$), allowing us to conveniently use the flux at the low boundary as normalization.

Using a custom reference energy fixes this flux at E_0 for a given Φ_0 and by changing the spectral index γ we can control the steepness of the spectrum. In figure 3.12 the modeled flux with different spectral indices for two different flux normalizations is shown.

To model the actual flux predictions from [41], we can try to recreate the distributions from figure 2.6 by drawing some lines and interpolating from the tick marks. This is done in a conservative way by using the maximum of the predicted spectra as the lower energy boundary, not including the predicted steep tail at energies below that. The parameters shown in table 3.3 are used to remodel the predicted emission from Vela and Crab, which are shown in figure 3.13. Notice how the simple bounded flux does not include the parts of the predicted spectrum at energies lower than where the flux peaks. This means that this flux model notoriously underestimates the prediction to a non-negligible extent and allows for only a very rough estimate of how sensitive ARCA would be to a flux that follows the one predicted by [41]. Nevertheless, this will be interesting to get an overall picture about the future prospects of neutrino astronomy with ARCA and can evaluate whether the

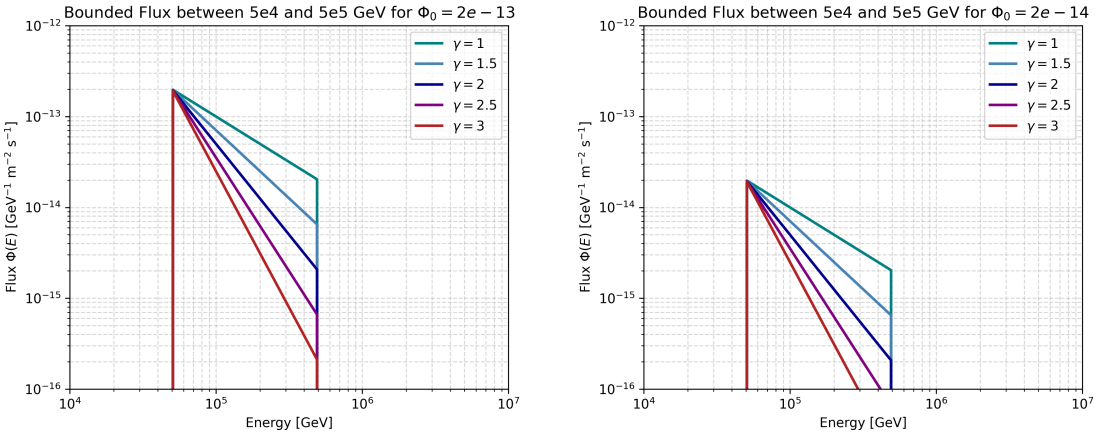

Figure 3.12: Modeled bounded power law flux with $E_0 = E_{\text{min}} = 5 \times 10^4\,\text{GeV}$ and $E_{\text{max}} = 5 \times 105\,\text{GeV}$ for different spectral indices γ. *Left:* $\Phi_0 = 2 \times 10^{-13}\,\text{GeV}^{-1}\,\text{m}^{-2}\,\text{s}^{-1}$ *Right:* $\Phi_0 = 2 \times 10^{-14}\,\text{GeV}^{-1}\,\text{m}^{-2}\,\text{s}^{-1}$

predictions can be tested with KM3NeT in the near future or not.

		E_{min} (GeV)	E_{max} (GeV)	Φ_0 ($\text{Gev}^{-1}\,\text{m}^{-2}\,\text{s}^{-1}$)	γ
Vela	linear origin	2×10^5	2×10^6	8×10^{-15}	2
	quadratic origin	1.3×10^5	2×10^6	5×10^{-15}	2.5
Crab	linear origin	7×10^4	6×10^5	1×10^{-13}	2
	quadratic origin	5×10^4	6×10^5	7×10^{-14}	2.5

Table 3.3: Parameters used to remodel the flux predictions from [41]

3.6.3 Calculating Detected Event Spectrum

Now that we calculated the effective area and have the flux model ready, we can use equation 3.4 to calculate the number of expected events for each flavor by simply folding the point source flux $\Phi(dE)$ with the effective detector area $A_{\text{eff}}(dE, d\Omega)$. This means that the fluxes shown in the following section are the arrival fluxes per flavor for an isotropic flavor distribution, which means the total flux of neutrinos corresponding to the detected events would be $\Phi_{\nu,\text{tot}} = 6 \times \Phi_{\nu,\text{flavor}}$. The number of events is calculated based on this folding operation and the overall exposure time. The length of this is defined by the active time of the detector in the respective analysis time window, which can simply be provided by the GTIs corresponding to the chosen background set.

The 2D effective area allows us to take into account that we are limiting our dataset to some cone around our chosen astrophysical source location and the zenith angle of this location changes over the course of one day due to the rotation of the Earth. Depending on where the source is located, it sweeps through a well defined zenith angle interval over the course of one day. We can simulate this

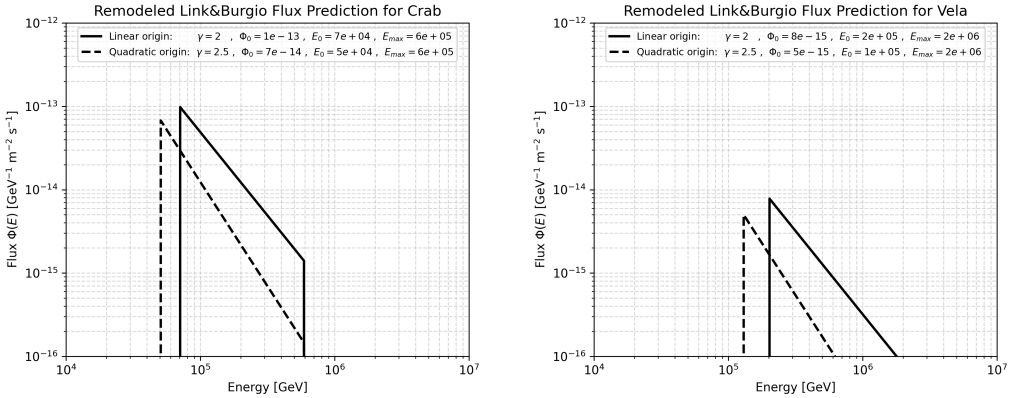

Figure 3.13: Prediction of the photohadronic neutrino emission from the Crab and Vela Pulsars remodeled after the calculated fluxes from [41] following figure 2.6

movement over the course of our analysis time window using the `astropy` software package to calculate the time dependent position and transform this into the local coordinate frame of the detector. We can then find the expected number of detected events that arises from this combination of flux spectrum, source position and effective area. In order to see the source choice's influence on the expected detected events for each tested flux model, we will have a look at the modeled responses for a flux coming from Vela and from Crab.

Classic Power Law Flux

The figures 3.14, 3.15, 3.18 and 3.19 all show the expected detected events per energy bin for each different flavor for the given input flux. The flux is shown as a purple dashed line and is plotted on a secondary y-axis on the right to make the differences between different fluxes more clearly visible in the figures. While the scaling of the flux axis is held constant, the primary y-axis showing the number of detected events is custom scaled for each case, to also be able to nicely see the internal distribution in the cases where not so many detected events are expected. The number of expected events is shown for each particle type, antineutrinos are plotted as dotted lines. Besides that, the total expected flux for track-like (ν_μ and $\bar{\nu}_\mu$) and shower-like (ν_e, $\bar{\nu}_\mathrm{e}$, ν_τ and $\bar{\nu}_\tau$) interactions is shown, which will be treated differently according to their reconstruction types in some of the following steps. Note that these distributions show actual samples of events that follow the expected spectra, so they can slightly vary with each simulation. We will first have a look at two example situations for the unbounded flux. The following plots show the detected events as expected for a point flux from Vela. The upper plots in figure 3.14 shows the situation for a harder spectrum for $\Phi_0 = 10^{-2}\,\mathrm{GeV}^{-1}\,\mathrm{m}^{-2}\,\mathrm{s}^{-1}$ and $\gamma = 1.7$. Due to ORCA's much smaller volume and therefore effective area, there are generally much less events expected from a hard spectrum which is most likely present in the high-energy neutrino range. We can still simulate the response of ORCA to other power law fluxes with greater absolute values of the spectral index just to get an idea of how our simulation responds to such inputs. The lower plots show the expected distribution for $\Phi_0 = 100\,\mathrm{GeV}^{-1}\,\mathrm{m}^{-2}\,\mathrm{s}^{-1}$ and $\gamma = 3.0$.

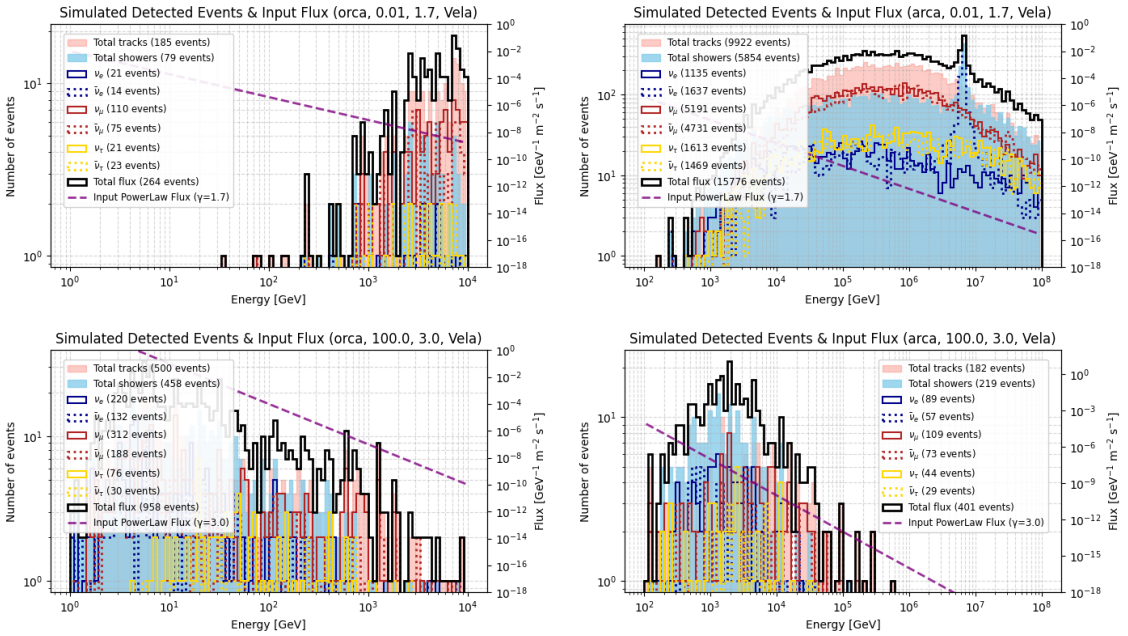

Figure 3.14: Expected distribution of detected events for a classic power law point flux from Vela with $E_0 = 1\,\text{GeV}$. Upper plots $\Phi_0 = 10^{-2}$ and $\gamma = 1.7$. Lower plots $\Phi_0 = 10^2$ and $\gamma = 3.0$. ORCA (1-10^4 GeV) on the left, ARCA (10^2-10^8 GeV) on the right.

One can see, that for our example situation with a low spectral index the number of detected events in ARCA is quite high with 15776 overall events over a time of 150 days, which would correspond to the detection rate of roughly 100 events per day. This flux model is obviously extremely unrealistic and is only shown to better see the distribution of individual flavors. To get a better feeling of how the distribution of detected events is expected to respond to changes in the input flux defined in equation 3.6, figure 3.15 shows this for a few selected parameters.

Not surprisingly, a softer spectrum, i.e. with a higher γ, leads to an overall reduced detection but most prominently causes fewer high-energy events compared to a flux with a harder spectrum. We see that for a spectral index of $\gamma = 2.0$ we can expect that the flux normalization above which ARCA starts detecting events is much lower than for ORCA. At the lower end of flux intensity where ARCA starts to become sensitive and starts to collect a sufficient amount of events to analyze, there won't be any, or only very little detected events arising in ORCA from the same flux. This shows that the decision of whether to include ORCA data into the analysis of cosmic neutrinos depends a lot on the investigated spectrum. Since the most important parameter for our analysis is simply the number of expected events, we can also have look at how that is expected to change for our modeled flux over the Φ_0 and γ parameter space, which is shown in figure 3.16.

For better comparison, both distributions are plotted above each other in a semitransparent way, to be able to directly see how the responses are in relation to each other. One can clearly see, that a classic power law flux with $E_0 = 1\,\text{GeV}$ causes a generally higher detection response for ARCA up

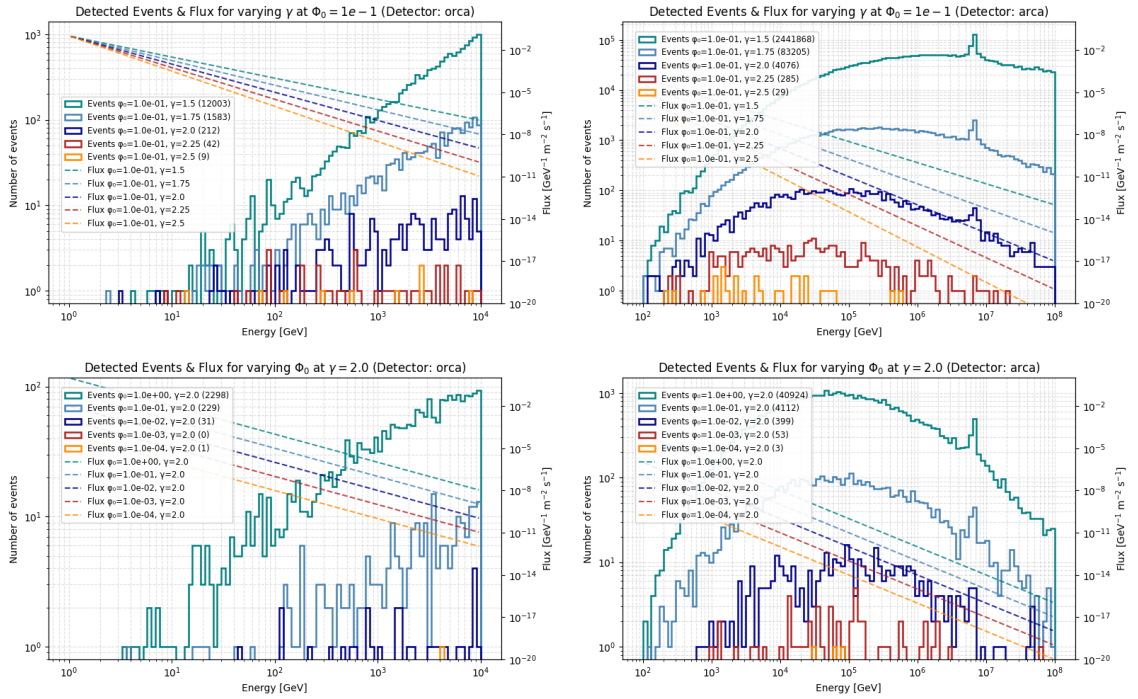

Figure 3.15: Expected distribution of overall detected events for a classic power law flux with $E_0 = 1\,\text{GeV}$ For varying γ (upper plots) and varying Φ_0 (lower plots). ORCA (1-10^4 GeV) on the left, ARCA (10^2-10^8 GeV) on the right.

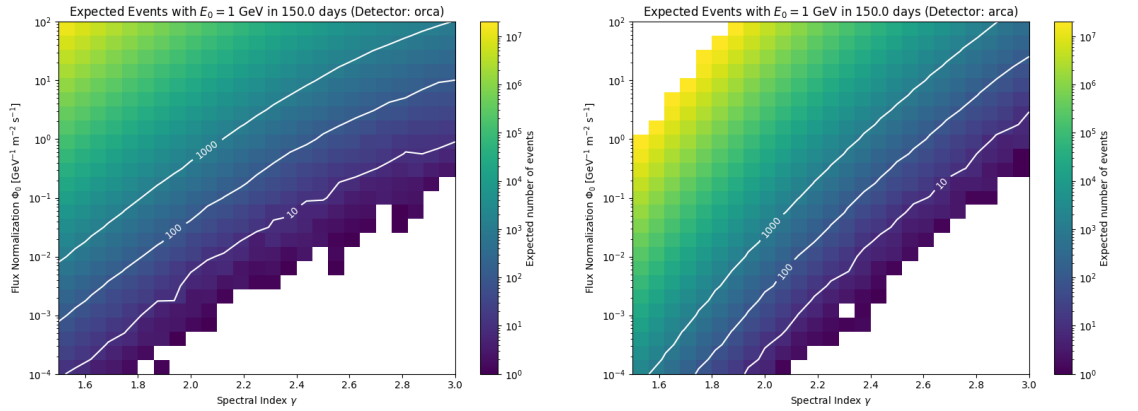

Figure 3.16: Expected number of overall detected events for a classic power law flux with $E_0 = 1\,\text{GeV}$ for different Φ_0 and γ. ORCA (1-10^4 GeV) on the left, ARCA (10^2-10^8 GeV) on the right.

to a spectral index of $\gamma_{\text{threshold}} \approx 2.8$. Even softer spectra lead to more events being expected to be detected in ORCA than in ARCA. This figure already provides an indication of the direction that

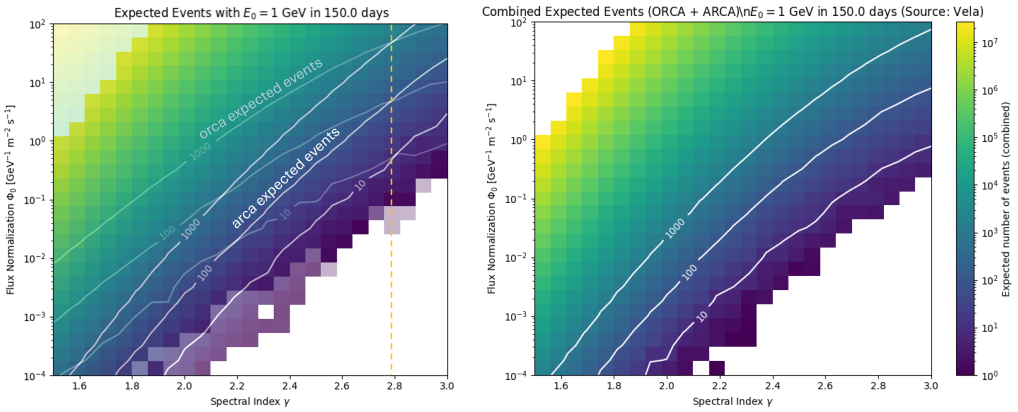

Figure 3.17: Left: Overlayed detection response heatmaps for a classic power law flux with $E_0 = 1\,\text{GeV}$ for different Φ_0 and γ from ORCA and ARCA. The individual plots are shown in figure 3.16. Right: Detection response for both detectors (total events)

the sensitivity study will take. Since the quality of the detection of a periodic signal will in the end of course depend on how many signal events are detected, this already shows the rough shape of the sensitivity distribution.

Bounded Power Law Flux

Having the classical power law covered, we can now have a look at the expected responses to a bounded power law flux. Due to the flux having a low energy boundary in the TeV regime, we will only have a look at ARCA for this flux model. The distributions are created analogously as in the case above, only the input flux model has been changed. We will look at the expected flux for both sources Vela and Crab using the corresponding predicted energy boundaries shown in table 3.3 and the corresponding source position evolution, which is relevant for the 2D effective area. Figure 3.18 show the expected event distributions for a high and a low flux normalization.

One can see how the same flux definition causes fewer detected events when the boundaries are shifted to higher energies. For a constant effective area the $E^{-\gamma}$ dependence of the flux would lead to a much higher number of detected events with lower energies. This is somewhat counteracted by the enlargement of the effective area with higher energy but still dominates, showing a higher number of detected events with high energies. We will now see how the expected event detection for our bounded flux model reacts to changes in spectral index and flux normalization in the same way as for the unbounded flux. The example plots are shown in figure 3.19. Having the flux normalized to a higher energy this time, the change in spectral index can lead to the situation at low γ where a higher detection rate is expected with higher energies. This effect is expected to be stronger for the Crab flux, which makes sense when looking at how the relative change in the effective area is slightly decreasing with higher energies in this regime and how the effective area depends on the zenith angle of the source. The Crab Nebula is mostly seen above the horizon ($\cos\theta < 0$) from ARCA's perspective and therefore the interaction is less dampened from matter interactions in the

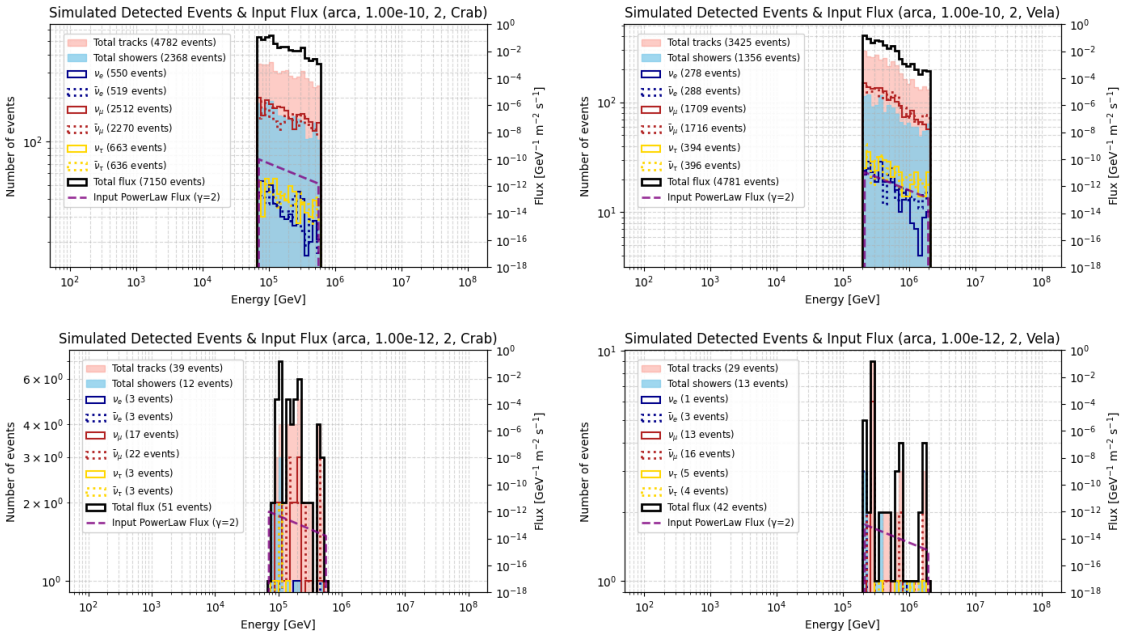

Figure 3.18: Expected number of detected events per flavor for a bounded power law flux with $\Phi_0 = 10^{-10}$ (at $E_0 = 7 \times 10^4\,\text{GeV}$) and $\gamma = 2.0$ for Crab ($E_{\text{min}} = E_0 = 7 \times 10^4\,\text{GeV}$ and $E_{\text{max}} = 6 \times 10^5\,\text{GeV}$, left) and Vela ($E_{\text{min}} = 2 \times 10^5\,\text{GeV}$ and $E_{\text{max}} = 2 \times 10^6\,\text{GeV}$, right). Upper plots $\Phi_0 = 10^{-10}$ and $\gamma = 2.0$, lower plots $\Phi_0 = 10^{-12}$ and $\gamma = 2.0$. Detector: ARCA.

Earth as opposed to Vela, which starts to have a subtle influence around $1e6\,\text{GeV}$ as can be seen in the 2D effective area plot for ARCA in figure 3.9.

It is important to keep in mind that this only helps us gaining a better understanding of how changes in the input flux cause different numbers and distributions of detected events and does not tell us anything about how sensitive we are to the detection of this flux and how this might be separated from the present background. The fluxes used for Vela and Crab are both normalized to the respective lower energy flux boundary, setting $E_0 = E_{\text{min}}$ (see: equation 3.7). Therefore, a chosen Φ_0 does not represent the same flux for both sources here. These plots help us however, to get a feeling for how changes in Φ_o and γ influence our expected detections and therefore also give us some insight on the degree to which this analysis depends on those parameters. Similar to the unbounded case, we calculate the numbers of detected events for a grid of Φ_0 and γ distributions to get a larger picture. One can see that for both sources the influence of the spectral index is rather low, especially between the two possible predicted proton acceleration scenarios which cause the neutrino spectrum to follow either $\gamma = 2.0$ or $\gamma = 2.5$.

This shows how the detector is expected to respond to changes in Φ_0 and γ for a power law flux bound within each source's E_{min} and E_{max} when the flux is normalized to the corresponding low boundary energy. Overall we can say that throughout each modeled flux, we get around 2-3 times

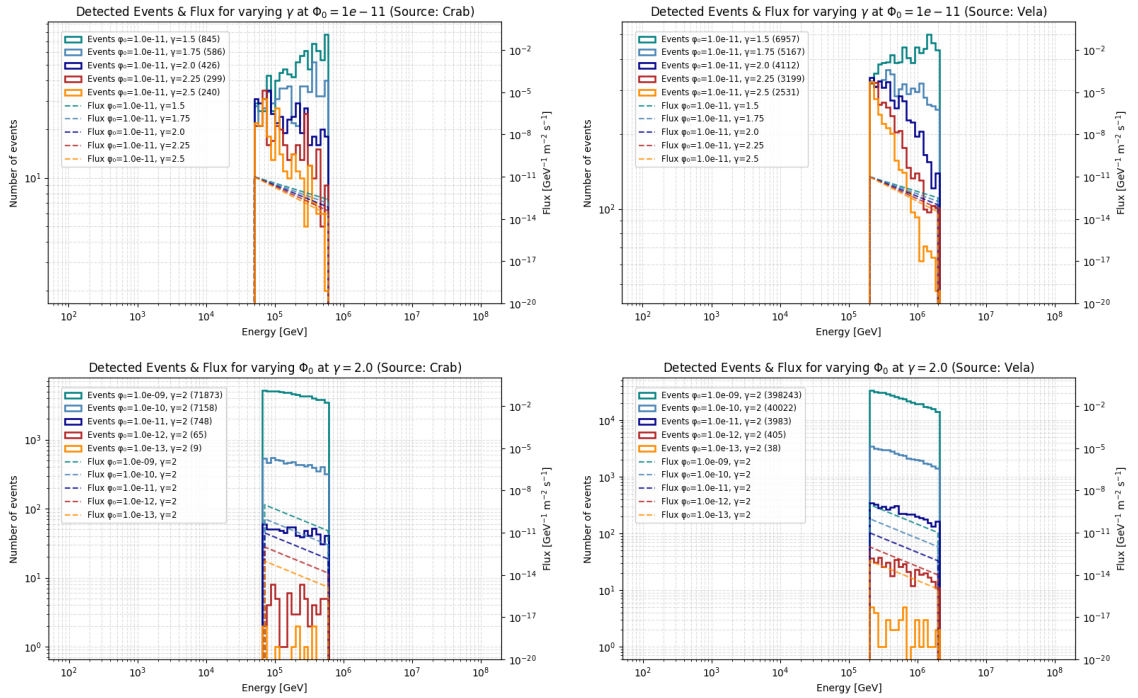

Figure 3.19: Expected distribution of overall detected events for a bounded power law flux from Crab ($E_{\text{min}} = E_0 = 7 \times 10^4\,\text{GeV}$ and $E_{\text{max}} = 6 \times 10^5\,\text{GeV}$, left) and Vela ($E_0 = E_{\text{min}} = 2 \times 10^5\,\text{GeV}$ and $E_{\text{max}} = 2 \times 10^6\,\text{GeV}$, right). Upper plots for varying γ, lower plots for varying Φ_0. Detector: ARCA

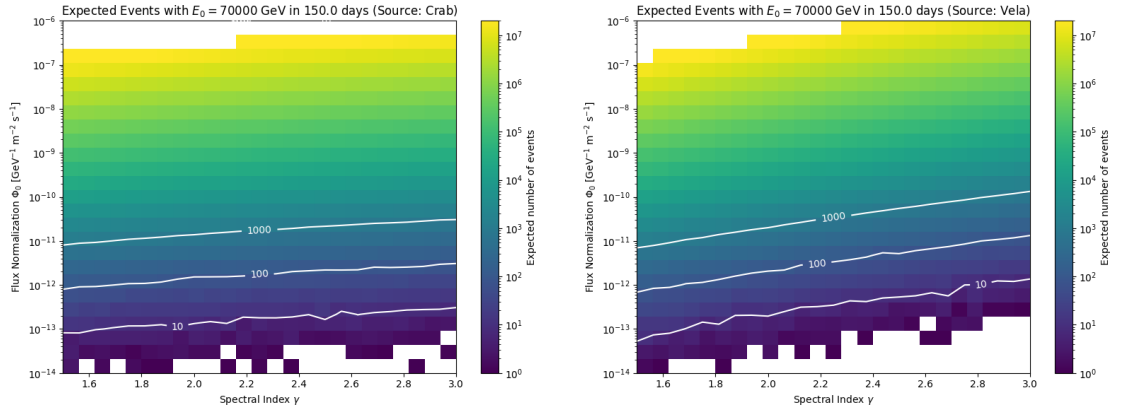

Figure 3.20: Expected number of overall detected events for a bounded power law flux from Crab ($E_{\text{min}} = E_0 = 7 \times 10^4\,\text{GeV}$ and $E_{\text{max}} = 6 \times 10^5\,\text{GeV}$, left) and Vela ($E_0 = E_{\text{min}} = 2 \times 10^5\,\text{GeV}$ and $E_{\text{max}} = 2 \times 10^6\,\text{GeV}$, right)

more muon track interactions than shower interactions. However, this strongly depends on the flux normalization and can in principle be reversed in some situations as shown in figure 3.14. We have now built the foundation for simulating the presence of a pulsed signal in our dataset by determining the distribution of expected detected events per neutrino flavor coming from different sources for each detector. Spoiler alert: Calculating the response to the modeled fluxes shown in table 3.3, which resemble the actually predicted spectrum, we expect less than 10 events from each source over 150 days with the ARCA21 setup. For the case of quadratic proton acceleration, we expect one event or less. Nevertheless, we can try to give some estimates about how the analysis of periodic neutrino emission with KM3NeT is expected to react to higher rates and find out how far away we are from detecting the predicted fluxes under the premise of a known periodic signal.

3.6.4 Simulating Energy Reconstruction Response

The modeling of the detection response makes it possible to predict the true energy spectrum of neutrino interactions from a defined flux. We can make use of this to be able to assign some energy or directional dependent selection cuts to get rid of unwanted background events. When looking at real data however, we have only access to the reconstructed energies and directions and do not know the true energy or direction this neutrino was actually having. In section 3.3.2 we were already dealing with the directional uncertainty by calculating the mean angular error for a given particle type and detector based on an event's reconstructed energy. To account for the uncertainty regarding the true energy, we will model the energy reconstruction response based on the MC files by looking at the distribution of $(E_{\text{true}}, E_{\text{reco}})$-pairs for a very large amount of simulated events. The events are normalized, along each E_{true} bin to account for the fact that we are trying to mimic the energy smearing in the reconstruction process by simulating the expected probability distribution of reconstructed energies for a given true energy. This is why the probability density function (PDF) has to integrate to 1 over each bin. We can then sample an E_{reco} from a given E_{true} based on the detector and the reconstruction type by using the respective PDF for this energy bin for sampling. The reconstruction response depends on the type of the reconstruction (shower/track) and the detector (orca/arca). We will have a look at the 2D (E_{reco},E_{true}) distributions as well as the PDF for a given true energy of 10 GeV in the case of ORCA (figure 3.21 and $1e5$ GeV for ARCA (figure 3.22).

Looking at the reconstruction from ORCA we notice that the 2D distributions show some strange artifacts, which are more visible in the shower reconstruction. This shows that the reconstruction of events with $E_{\text{true}} \gtrsim 10$ GeV partly causes the reconstructed energies to accumulate not only near the actual true energy but also at around 10 GeV. Below 10 GeV the energy resolution gets much better, but still seems to slightly underestimate the true energy. We have to think a bit about what this means for our analysis if our injected signal's reconstructed energy is deviating too much from the original one. The lower reconstructed energy would for once cause a higher angular resolution to be assigned to the corresponding event (see figure 3.4 and therefore possibly falling out of our selection cone and not making it into the final dataset. Furthermore, this would change our results if the reconstructed energy falls below our threshold energy when applying the data cuts and will also be omitted. In general, we can say that this artifact does only influence the result of our analysis only slightly and in a conservative way, meaning that reconstructing lower energies causes rather an underestimation of injected events and therefore does not artificially increase our expected sensitivity. In sight of the expected events estimated for both detectors as shown in figure 3.16, we will not be concerned any further with this, since the influence on our actual sensitivity of the detector is very small. This also highlights ORCA's specialization on energies between 1 and 100 GeV and shows that

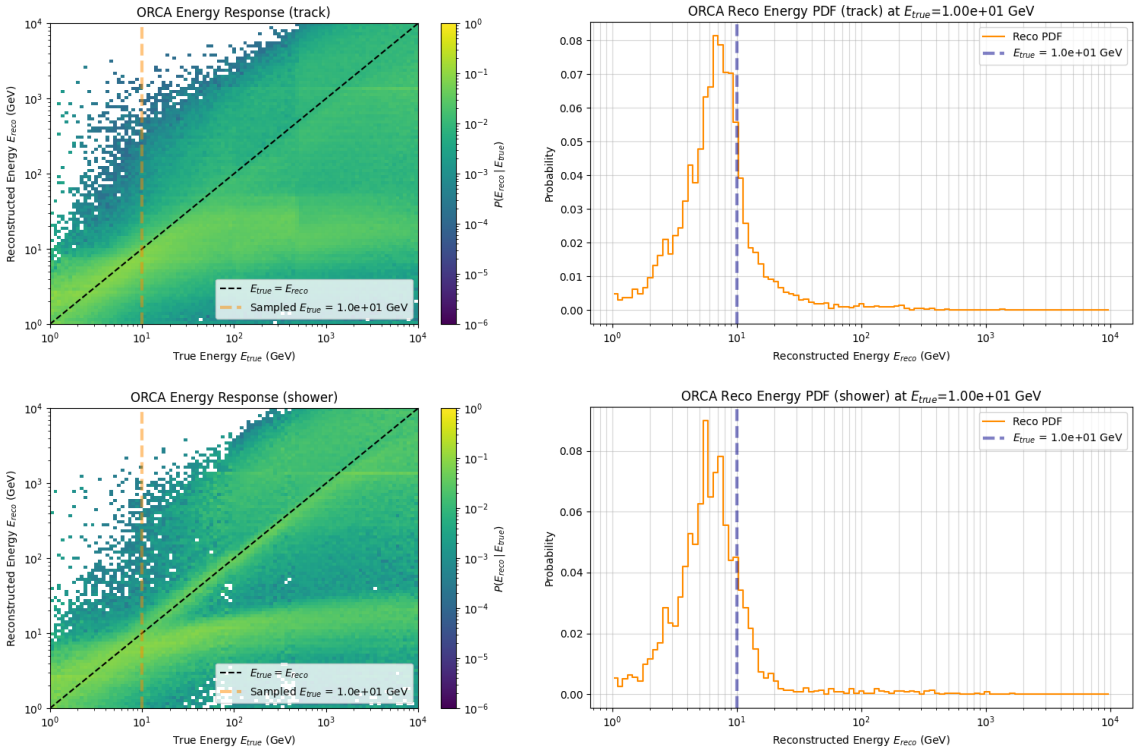

Figure 3.21: Energy reconstruction responses for track (upper plots) and shower (lower plots) reconstructions from Monte Carlo simulations. The right plots show the probability distribution function for the expected E_{reco} for the chosen $E_{\text{true}} = 10\,\text{GeV}$. Detector: ORCA

it was not designed to deal with the detection of higher energy neutrinos. The higher energy events still interact and are detected but the reconstruction algorithm is only working nicely at low energies.

The ARCA distributions in figure 3.22 show that the energy reconstruction is working better in this case: The maximum within each bin is expected around $E_{\text{reco}} = E_{\text{true}}$. The energy resolution is still quite broad, having misreconstructions deviating over multiple orders of magnitude from the true value. While also too high energies are reconstructed, both algorithms favor lower energy results as well. The shower reconstruction shows a more defined PDF, having the overall better energy resolution. This is partly due to the fact that in most shower events all the energy is deposited inside the detector volume whereas muons can have propagated for a relatively long distance before entering the detector volume or can also be produced inside and then leave the volume.

We can now use these energy responses to model the expected reconstructed energy for the simulated detected events arising from a certain flux. Figure 3.23 shows how the energy reconstruction sampling responds to the true energy distribution expected from a classic power law flux with $E_0 = 1\,\text{GeV}$, $\Phi_0 = 1\,\text{GeV}^{-1}\,\text{m}^{-2}\,\text{s}^{-1}$ and $\gamma = 2.0$ for each detector and reconstruction type. The ARCA events

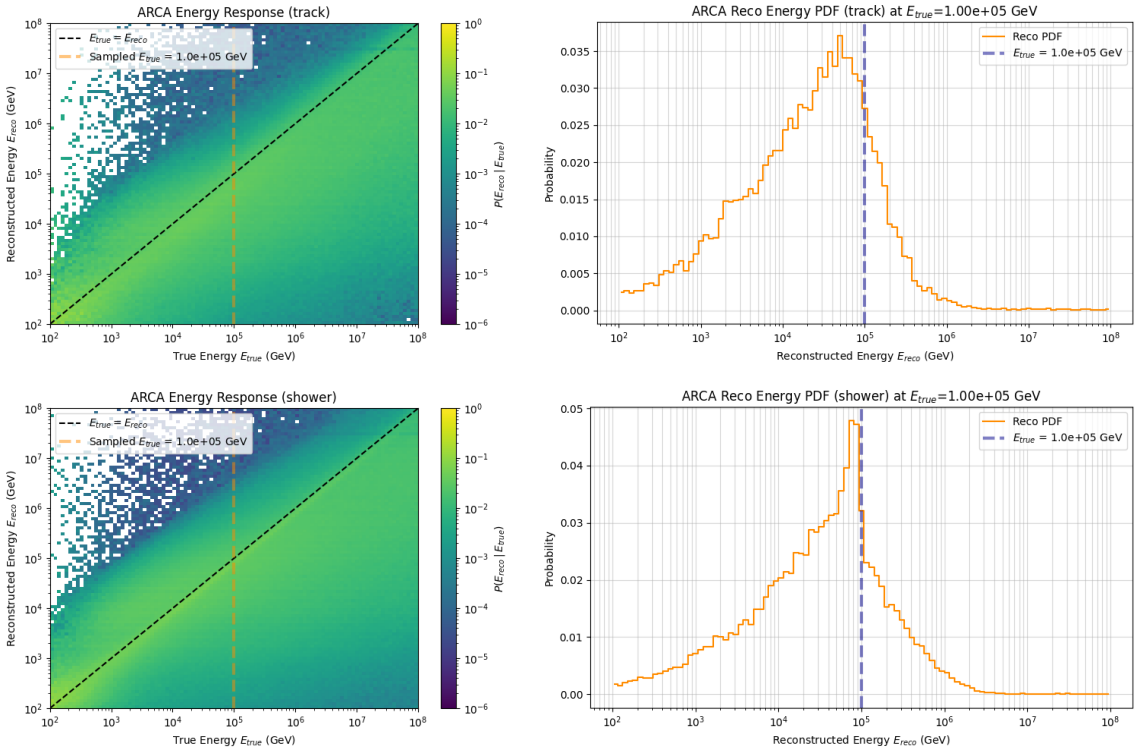

Figure 3.22: Energy reconstruction responses for track (upper plots) and shower (lower plots) reconstructions from Monte Carlo simulations. The right plots show the probability distribution function for the expected E_{reco} for the chosen $E_{\text{true}} = 1e5\,\text{GeV}$. Detector: ARCA

are shifte to lower energies, especially for the track reconstructions. For the shower energies we see that the peak arising from the Glashow resonance in $\bar{\nu}_e$ is nearly invisible afterwards. The broad peak of the shower spectrum is still present at roughly the same position after the reconstruction, however there are in total more low and less high-energy events being reconstructed than actually present here as well. It is good to keep in mind how the reconstruction affects the initially expected neutrino spectrum when applying energy cuts or performing other energy dependent operations. For ORCA we see how the artifact in our reconstructions causes the high-energy detections expected from its effected area to be wrongly reconstructed to much lower energies and the spectrum is generally wrongly reconstructed.

3.6.5 Modeling Event Origin

To simulate how the reconstructed directions of the detected events is expected to be received when the flux is coming from a point source, we will use the angular error estimation based on the reconstructed energy. For each signal time, we calculate where the chosen source is currently located in the detector local frame. The chosen signal origin for the injected event is simply done by calculating

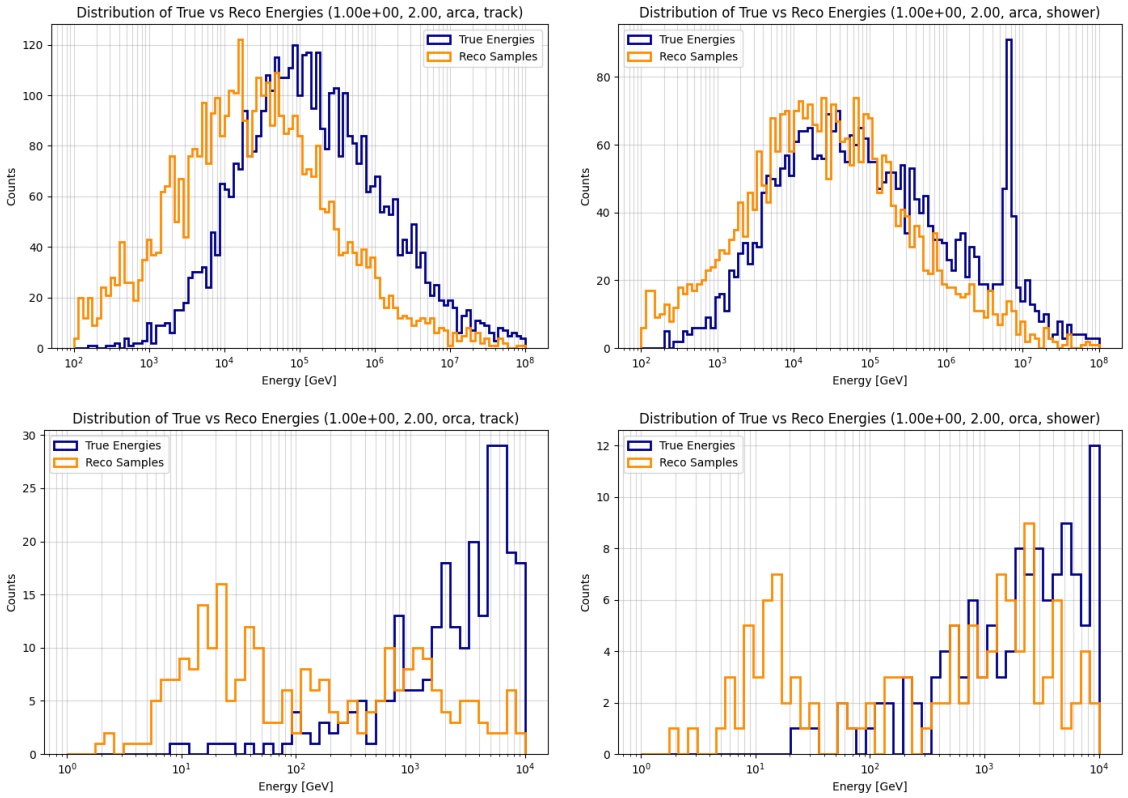

Figure 3.23: Changes in the energy spectrum before and after the reconstruction sampling for an unbounded power law flux with $E_0 = 1\,\text{GeV}$, $\Phi_0 = 1$ and $\gamma = 2.0$. Shower and track reconstructions applied to the respective expected detected event spectrum. Upper plots ARCA (10^2-$10^8\,\text{GeV}$), lower plots ORCA (1-$10^4\,\text{GeV}$).

the true θ and φ (detector frame) for the corresponding source coordinates. These values are then modified by adding $\delta\varphi$ and moving the event origin in a random direction. The scale of this offset is drawn from a normal distribution centered around the angular error for the event's reconstructed energy. This means that for example track events in ARCA will be simulated to be detected arriving very closely from the source direction, whereas the origins of shower events will be simulated within a large cone around the source. After this step, the same maximum angle cut is applied as for the creation of the background set to make both sets compatible as if they were originating from the same selection of data associated with a source.

Figure 3.24 shows the simulated source directions of the reconstructed events in the frame of the respective detector. This uses the sampled reconstructed energies shown in figure 3.23 and the angular error estimates shown in figures 3.3 and 3.4 for each event based on the energy and the reconstruction type. These examples here demonstrate how we are expecting the reconstructed event origin arising from a point flux from Vela and Crab with $E_0 = 1\,\text{GeV}$, $\Phi_0 = 1\,\text{GeV}^{-1}\,\text{m}^{-2}\,\text{s}^{-1}$ and $\gamma = 2.0$ to be distributed over a 150 days timeframe. For ARCA rack reconstructions are expected

to clearly map out their origin pointing straight to the source with a very high angular precision. Shower events might also be reconstructed quite further away from where they were initially coming from. The ORCA events are generally sampled with much less precision as one can see. The origin of this lies in the fact that the directional reconstructions for ORCA data are not suited for these high-energy events we are looking at here, which does not allow for the correct reconstruction of the neutrino direction anymore. Above $E_{\text{reco}} = 10^2\,\text{GeV}$ the angular error rises very quickly and then events are reconstructed with random orientations. Besides how the events are distributed with respect to the so source, we can also see a difference in the expected source path itself, arising from the higher latitude of ORCA. For completeness, figure 3.25 shows the expected reconstructed event directions for a more realistic flux at ARCA. Notice that with a well working classification one would expect a much higher fraction of the dominant ν_μ and $\bar{\nu}_\mu$ flux to be reconstructed with high angular accuracy, which would result in the expected event origins to be more confined to the source path and less spread around. This would of course also enable a smaller selection region around the source in order to increase the signal to noise ratio.

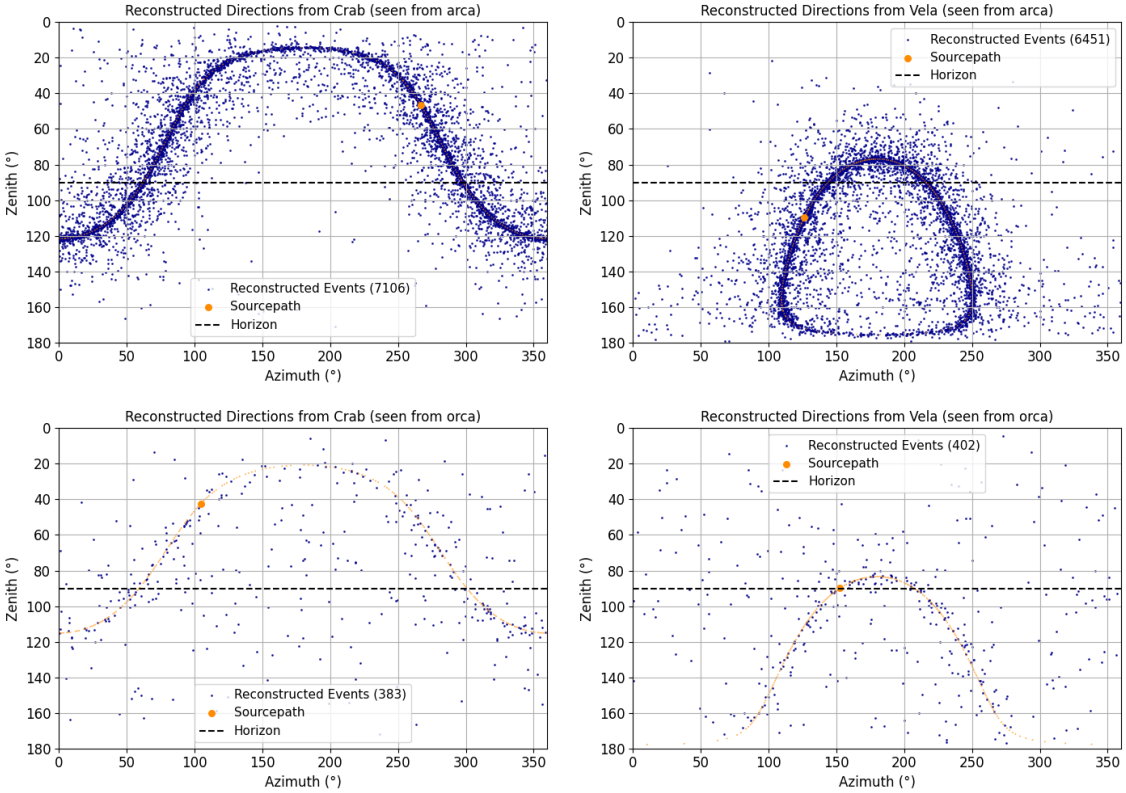

Figure 3.24: Modeled event origins for an unbounded power law flux with $E_0 = 1\,\text{GeV}$, $\Phi_0 = 1$ and $\gamma = 2.0$ from Crab (left) and Vela (right). Upper plots ARCA (10^2-$10^8\,\text{GeV}$), lower plots ORCA (1-$10^4\,\text{GeV}$).

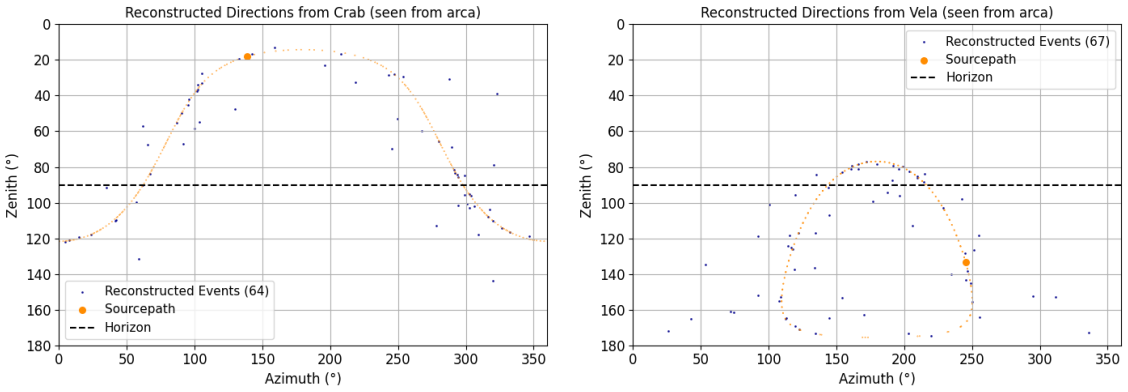

Figure 3.25: Modeled event origins for an unbounded power law flux with $E_0 = 1\,\text{GeV}$, $\Phi_0 = 10^{-2}$ and $\gamma = 2.0$ from Crab (left) and Vela (right). ARCA (10^2-$10^8\,\text{GeV}$)

3.6.6 Modeling Periodic Timing

The important part that will be used to characterize the sensitivity of the epoch folding analysis is modeling the event arrival times that are expected for a pulsar signal. The general approach is to define some lightcurve that represents an emission intensity over time and to then sample single event arrival times expected from this signal using stingray's event simulator function. The first step is to define a base function that describes the evolution of the expected count rate over time. We will use a modified von Mises distribution (MVMD) to simulate the signal pulses, which is well suited for modeling pulsar data, especially in radio and X-ray, where the emission shows much sharper peaks and is less noisy compared to measurements with higher energy photons, as can be seen from the pulse profiles shown in figure 2.2. The function we use is described as follows:

$$f(t, f_p, \kappa) = a \frac{\exp\left(\kappa \cdot \cos\left(2\pi f_p t + \phi\right)\right) - \exp\left(-\kappa\right)}{I_0(\kappa) - \exp\left(-\kappa\right)} + b \tag{3.8}$$

where t is the time, f_p the pulse frequency, κ the shape parameter, ϕ the phase offset, a the scaling parameter to which each pulse integrates to, b the baseline offset and $I_0(\kappa)$ the modified Bessel function of κ of 0-th order. Figure 3.26 shows how the pulseshape changes with a varying shape parameter κ and baseline offset b. The shape parameter describes how sharp the emission is concentrated around each pulse center. A low κ means that the pulse is spread out and deviates more from an ideally pulsed signal, whereas a high κ defines a very sharp pulse after every pulse period. The influence of the baseline b is of course simply an overall offset of the relative intensity. Notice, that also in this case the overall area remains constant, so that two different curves correspond to the same emission when being used to define the expected countrate over time. One can see how the baseline offset reduces drastically how much of our signal will actually be modeled with a periodic timing instead of just randomly, which therefore is expected to have a strong effect on our sensitivity regarding the detection of this signal by epoch folding.

Figure 3.27 shows some examples for modeled event times for two different shape parameters and two different event densities. Each plot shows the sampled event arrival times as gray vertical lines that arise from the underlying MVMD shown in blue. The orange curves show the binned lightcurves of

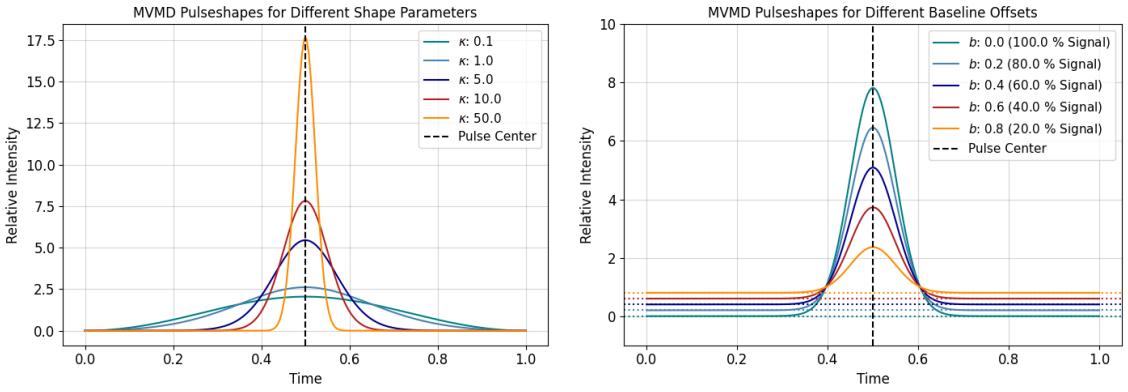

Figure 3.26: MVMD plotted over one pulse period for different shape parameter κ (left) and baseline offset b (right). The ratios in the right plot show the integrated signal area as expected for no baseline offset over the total integrated area, which estimates how much or this signal will be produced in a pulsed way.

the sampled events. We see how for a higher κ the simulated times are more sharply bound around the pulse centers. The baseline is set to zero, which results in no expected events between individual peaks for sharp pulses. The lower figures show how the event times were expected for an overall much smaller amount of simulated events. Note that the actual height of the underlying MVMD is of no importance for our analysis because we just use it to simulate the overall expected timing distribution and then sample as many events as we are expecting to arise from our respective flux model from this distribution.

In our analysis we have the following situation. The actual Pulsar emission has periods in the range of milliseconds, the number of detected events is very low and we are therefore looking at a sufficiently long timescale. For our sensitivity study, this means that we need to model a low number of event times over a long time, very accurately following the periodic emission happening at subsecond scale. To keep this computationally at a reasonable level, this is done as follows:

1. Generate base lightcurve with very high timing resolution spanning over n_p periods for a given frequency f_p
2. Calculate how often n_{tot} this base interval fits in the overall analysis time window T_{analysis}
3. Sample random base event time t_b from base lightcurve and sample random integer i in $[0,n_{\text{tot}}]$
4. Sample random event time $t = t_b + i \cdot n/f_p$

This ensures that all events follow nicely the simulated periodic timing without having to create a huge high resolution array to sample from. We can now think about which parameters to use for modeling the periodic emission expected to be present in the neutrino emission.

From the underlying physics we expect the neutrinos from pulsars to be formed from high-energy cosmic rays that are accelerated along the pulsar's magnetic axes. The neutrinos form a beam co-rotating with the beam of light and protons, which sweeps over earth and leads to the detection of a

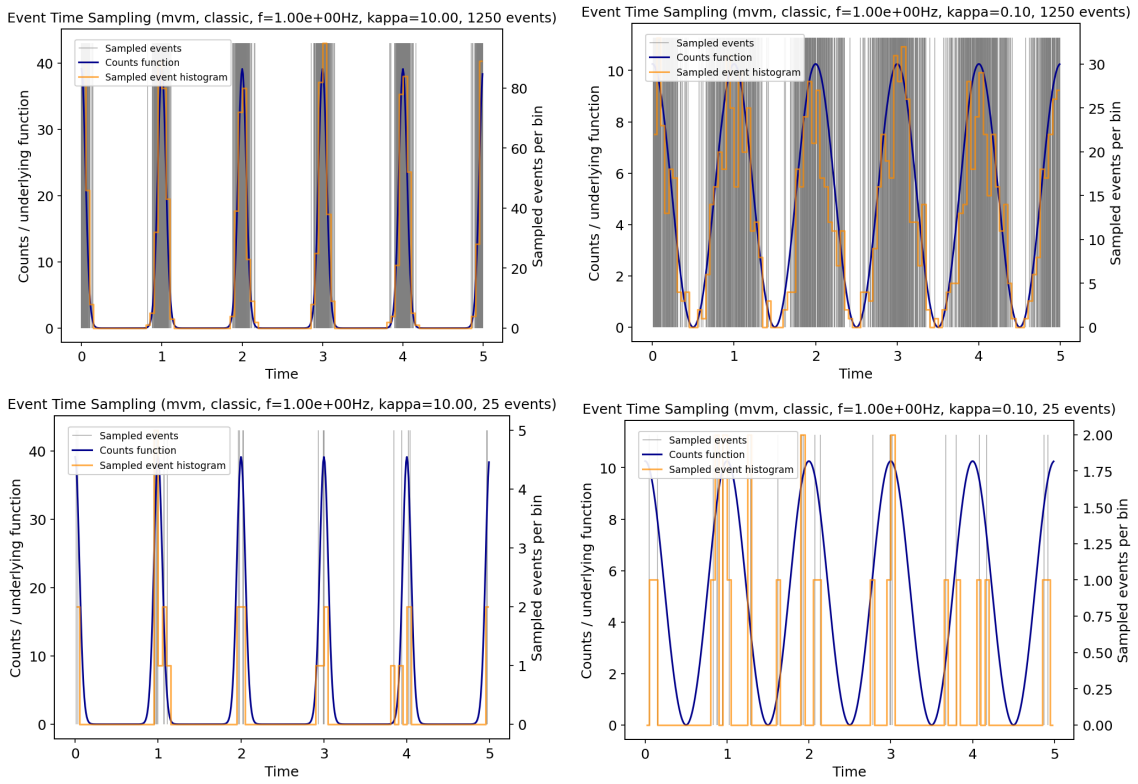

Figure 3.27: Example time sampling for a sharp pulse ($\kappa = 10$) and a broader pulse ($\kappa = 0.1$) for the case of 2500 and 50 events sampled within this time frame of 5 pulse periods.

periodic emission pattern. Since the neutrinos are expected to be produced in close proximity to the compact object and no form of broadening through scattering or magnetic deflection is taking place, the pulse shapes are expected to show very narrow peaks, comparable to the patterns detected in the radio band. To make sure that the analysis is not relying on perfectly sharp peaks and to keep it more conservative and still enable some pulse variation that might arise from different neutrino production locations and possible errors from the uncertainty about where the neutrino interaction took place in the detector environment, a form factor of $\kappa = 5.0$ is used to model the pulsar timing. Investigations on the variation of κ showed a negligible influence of the peak shape on the sensitivity if it is kept within a physically reasonable range above $\kappa \approx 2$, which can already be considered extremely broad for the expected neutrino timing. The frequency on which the timing modeling is based and around which the epoch folding search will be applied is chosen based on the pulse period of the chosen source object, which in our case is either Vela ($P_{\text{vela}} \approx 98\,\text{ms}$, $f_{\text{vela}} \approx 11.2\,\text{Hz}$) or Crab ($P_{\text{crab}} \approx 33\,\text{ms}$, $f_{\text{crab}} \approx 30.3\,\text{Hz}$).

3.6.7 Remarks on Error Estimation

The periodic timing analysis and the corresponding sensitivity study are subject to a number of simplifications and uncertainties. In the following, we will try to estimate the largest influences

regarding the resulting sensitivity distributions. One has to differentiate between statistical uncertainties arising from random sampling operations in the course of the analysis and systematic errors that are inherent to the detector, our analysis method and our simulation choices.

To minimize the statistical uncertainties in the sensitivity study, the whole analysis chain from the sampling of detected events up to the epoch folding can be run for numerous iterations and the maximum χ^2 value from the epoch folding can be averaged over multiple runs belonging to the same flux definition. Figure 3.28 shows the resulting mean maximum χ^2 and the corresponding error. We see that this forms a normal distribution at high iteration numbers. However, this is quite computationally demanding to run each parameter combination for 100 times, which is why 10 iterations were chosen for the results presented here.

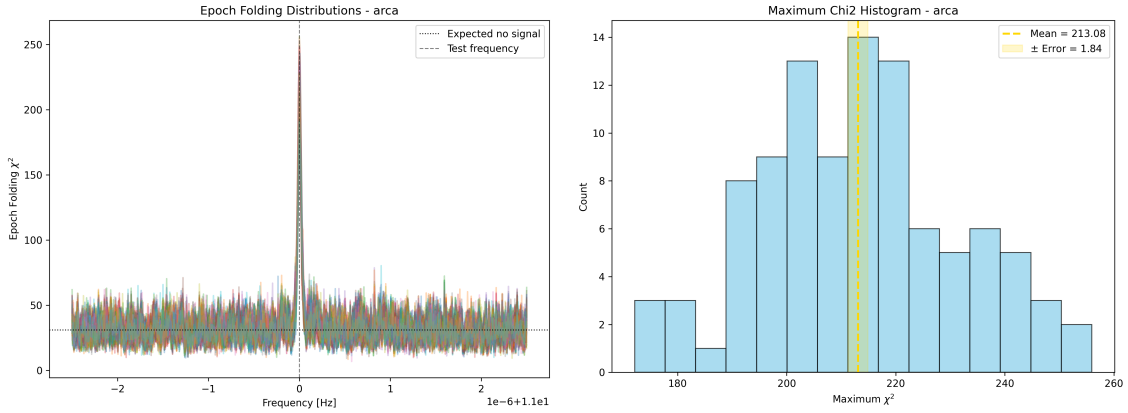

Figure 3.28: Results of the epoch folding search for 100 iterations for the same flux definition. The left plot shows and overlay of the final χ^2 distributions and the right plot shows a histogram of the maximum values together with the mean value and the error on the mean.

We will see that the statistical uncertainties are quite small in comparison to the changes in sensitivity that arise from different flux definitions and in the broad view spanning over spectral indices from 1.5 to 3.0. This also supports our choice of using less iterations to achieve lower computation times. While we get smoother distributions, no real gain in knowledge arises from using 100 iterations instead of running it just once. However, this might be of importance when having a more refined look at certain fluxes.

The systematic errors on the other hand are very hard to quantify, due to the large number of different processing steps and methods that are combined in this analysis. Nevertheless, we will now try to give an overview about the possible influences. A high source of uncertainty is the modeling of the periodic timing, which is done in a very simple approach by simulating the neutrino emission in a way that resembles the sharp emission peaks in the radio band. The variation of pulse shapes, especially pulse broadening, can lead to much lower detection sensitivities. However, we argue that the emission of neutrinos will be strongly confined to a certain pulse period (when the emission beam sweeps over Earth) and is not subject to other interactions. Therefore, the pulses are in theory expected

to be very sharp. Furthermore, errors arise from the event selection process, especially at energies where we have a high uncertainty regarding the angular resolution of the reconstruction, which is even further increased by the random classification of the event types, causing the analysis to use the wrong reconstruction results for half of the events. This also leads to a wrong estimation of the angular resolution and therefore causes errors in the event selection process for the background set and when sampling the expected reconstructed directions. However, since we would generally expect more track than shower events in reality, this random classification has a rather dampening effect on our sensitivity. This is because track events are much better suited for a point source analysis due to the low angular error and we could expect improved results with a properly working classification.

While the timing difference arising from the different reconstruction types is in principle very small, it is still necessary to think about the possible differences in detection time that arise from the different situations. For showers, the relative uncertainty regarding the time is extremely low. The nanosecond precision of the DOMs and the small local volume of light distribution enables a highly accurate depiction of the actual interaction time. For tracks this is more complicated because muons created in neutrino-nucleus interactions can travel a long distance before entering the detector volume. A rough approximation can show that the uncertainty regarding the arrival time arising from this is still low enough to not be of importance for the analysis of pulsars with millisecond periods. For the analysis of periodic emission we are interested in the arrival times of neutrinos in our detector. We can therefore look at a neutrino creating a muon upstream the line of flight, which then travels far enough that its Cherenkov light is detected and compare this to the situation where the same neutrino interacts just at the detector boundary from where the muon is then propagating through it. The nearly massless neutrinos travel approximately at the speed of light c, whereas muons are slightly slower, traveling with $v_\mu(E_\mu)$:

$$v_\mu = c\sqrt{1 - \left(\frac{m_\mu c^2}{E_\mu}\right)^2} \tag{3.9}$$

With the muon mass $m_\mu = 105.7\,\mathrm{MeV}$ we can estimate the difference in perceived arrival time for a muon produced at a distance d from the detector.

$$\Delta t_{\mathrm{arrival}} = \frac{d}{v_\mu} - \frac{d}{c} \tag{3.10}$$

For example, a muon produced 1 km away from the detector causes a timing delay of around 20 ns for 1 GeV muons. This difference drastically reduces for higher energies and can generally be ignored in the analysis of millisecond pulsar timing. In summary we can say that while this analysis can provide an estimation of KM3NeT's sensitivity towards the detection of the modeled pulsar signals, one should of course still keep in mind that systematic effects might possibly shift the sensitivities and the discovery potential to some extent.

4 Results

In this chapter the results of the sensitivity study are presented. Starting with the classic power law flux, the threshold flux normalization $\Phi_0^{\text{threshold}}$ for each spectral index γ, for which the epoch folding χ^2 test reveals a 5σ detection of a periodic signal if it were present in the signal. The effect of zenith angle cuts and maximum opening angle of the search cone, as well as different source locations are evaluated. Afterwards, the same investigations are conducted for the bounded flux case, which represents the flux predictions from [41]. We will see how the ARCA21 and ORCA18 setups perform in the context of this analysis and we will try to estimate how the sensitivity can be expected for longer analysis times.

4.1 Classic Power Law Flux

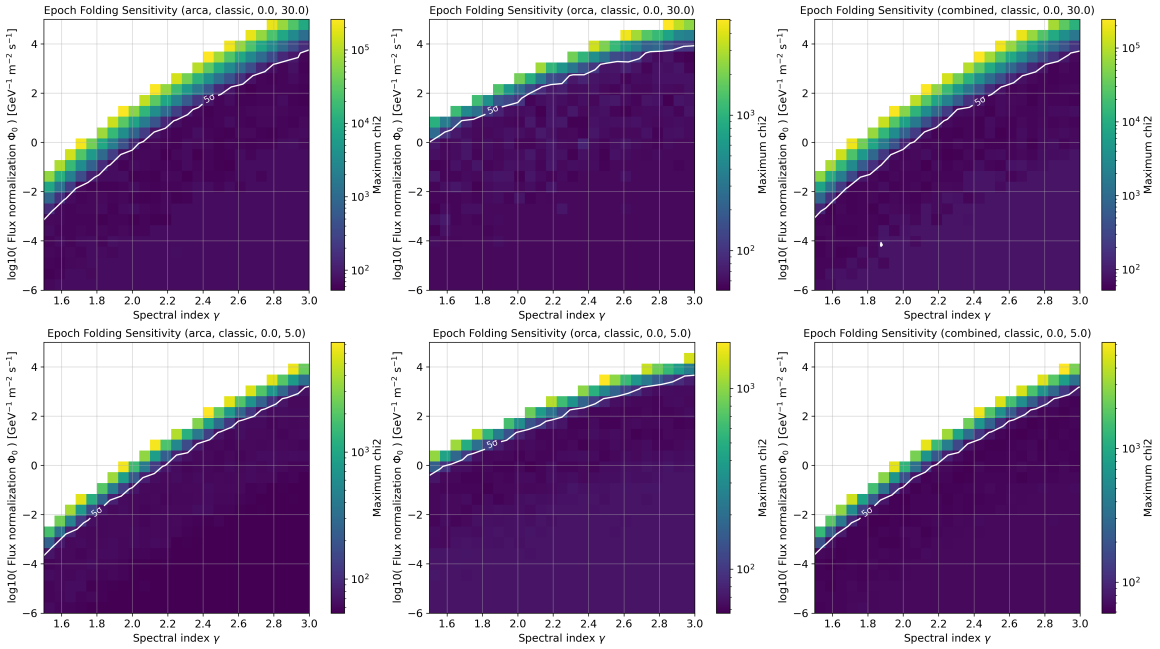

Figure 4.1: Epoch folding sensitivity for a classic power law flux from Vela with 0 deg zenith cut, 30 deg maximum search cone angle (top), 5 deg maximum search cone angle (bottom). ARCA (left), ORCA (middle) and Combined (right).

The sensitivity plots in this section show the χ^2 value of the epoch folding search applied to a dataset with an injected periodic signal according to the corresponding flux defined by the spectral index γ and the flux normalization Φ_0. The sensitivity is defined as the minimal flux which would lead to a 5σ detection of a periodic signal with the epoch folding analysis. In these plots, this is shown as the white contour, which shows for each γ the corresponding $\Phi_{0,\text{min}}$ where this is the case. A flux of periodic emission with the corresponding pulsar frequency that is located above this white line is

expected to be significantly detected by this analysis.

Figure 4.1 shows the sensitivity plots for a classic power law flux coming from Vela for two different maximum search cone opening angles. No zenith cut was applied. One can see how the general shape follows the predicted expected events distributions shown in figures 3.16 and 3.17. Including the ORCA detections into the ARCA analysis is seemingly not causing any improvement in epoch folding sensitivity for the modeled fluxes. One the one hand this is of course expected because of the huge difference in detected events between both detectors, so this only contributes to a few percent of the signal events. On the other hand it is still remarkable that this has so little influence on the sensitivity, because for the fluxes at which ARCA starts to significantly detect periodic signals, no events at all are expected to be detected by ORCA, which means that including ORCA data means simply adding more background. In figure 4.2 the 5σ contours for the different detectors are overlaid.

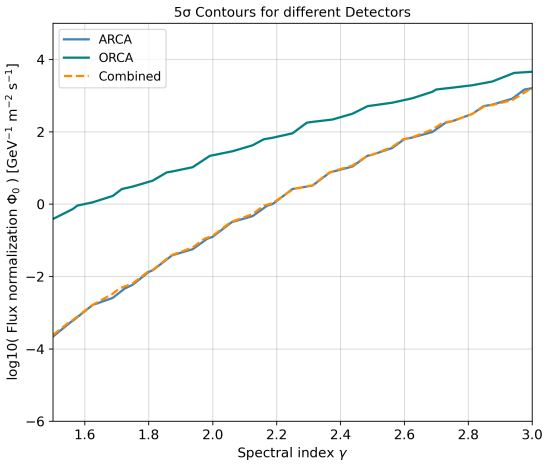

Figure 4.2: 5σ contours for different detectors for a classic power law flux from Vela without zenith cut and 5 deg opening angle.

One can furthermore see, that the sensitivity is better for the narrower selection cone, shifting the sensitivity curve to lower Φ_o. The confinement to events coming from closer around the source leads to a much lower background influence in the data set. While there are also events being lost, which are reconstructed with a high angular uncertainty, we can still expect all the correctly reconstructed track events from ARCA to be lying inside the selection cone due to the very good angular resolution. Since there are overall more ν_μ and $\bar{\nu}_\mu$ expected to be detected due to the higher effective area, this leads to an improvement in the signal to noise ratio in our analyzed timeseries and therefore the quality of the detection increases in such a way that a 5σ certainty about the detection of a signal is possible already at lower Φ_0. In figure 4.3 the resulting 5σ contours for different maximum opening angles are shown together for the combined case, to better show the differences in sensitivity.

We can now have a look at the influence of zenith angle cuts on our timing analysis. Therefore, we compare the sensitivities for different choices of minimum zenith angles. A zenith angle of 0 means that the neutrino is going straight downwards through our detector, whereas a zenith angle of 180

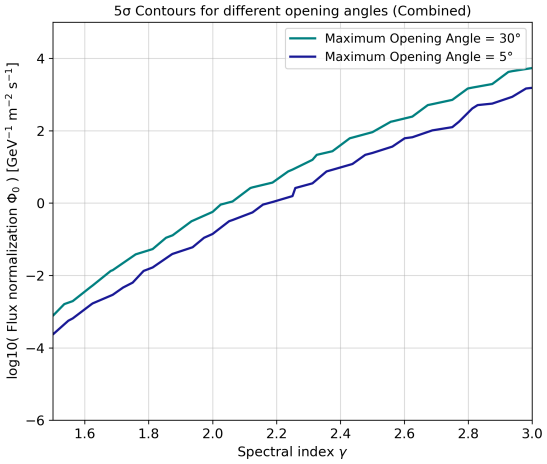

Figure 4.3: 5σ contours for different maximum opening angles for a classic power law flux from Vela without zenith cut.

degrees means the neutrino is straight upgoing. Cutting out all events with zenith angles below 90 degrees allows to get rid of the big amount of atmospheric muon events which pose the highest non-neutrino background in our detector. Depending on the chosen source, this can however lead to a big part of data events being removed as well, as one can see when looking at figure 3.24. It is not straightforward to tell whether the reduction in background events exceeds the loss of signal data in terms of the positive effects on the epoch folding sensitivity, because this depends a lot on the source's position and the signal intensity. Figure 4.4 shows the sensitivity for a flux from Vela with a maximum opening angle of 30 deg and 90 deg zenith cut.

One can see that this also increases the sensitivity compared to the situation without zenith cut.

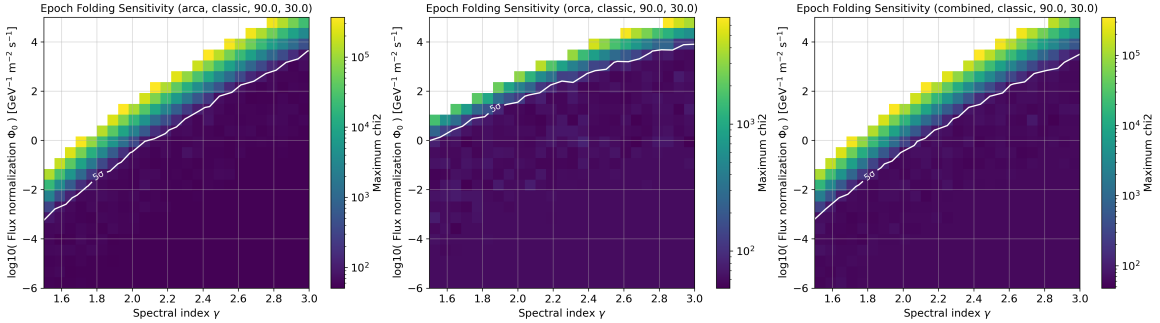

Figure 4.4: Epoch folding sensitivity for a classic power law flux from Vela with 90 deg zenith cut and 30 deg maximum search cone angle. ARCA (left), ORCA (middle) and Combined (right).

To get a better view of this improvement, figure 4.5 shows a comparison between 0 and 90 deg zenith cuts for an opening angle of 30 deg. Overall, the confinement to a smaller search cone has more influence on the sensitivity for the modeled classical power law flux coming from Vela. As mentioned before, this can however not be generalized to all situations but only characterizes how our sensitivity

for a detection of a periodic signal from Vela changes for our current detector setup. Having a better classification and angular resolution also changes the situation again, probably favoring an even narrower selection cone for increased signal to noise ratio while still including enough events for the frequency search to work.

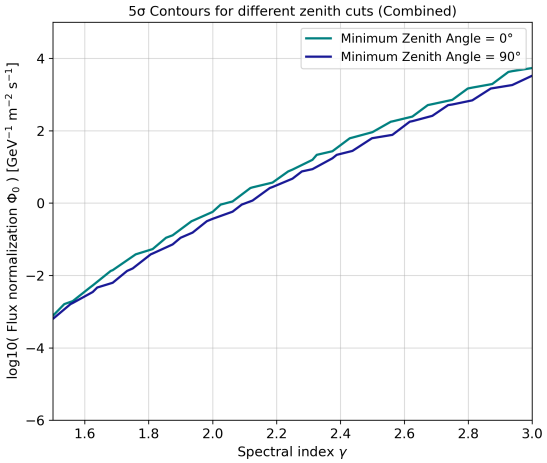

Figure 4.5: 5σ contours for different zenith cuts for a classic power law flux from Vela with 30 deg maximum opening angle.

From this sensitivity distribution, we can exemplarily take the situations at $\gamma = 2.0$, which simplifies the comparison to other results, which are often given in terms of $E^2\Phi_\nu$ instead. If the same reference energy (in our case $E_0 = 1\,\mathrm{GeV}$ is used, the flux normalization Φ_0 from this work is directly comparable to the corresponding $E^2\Phi_\nu$ representation of the differential flux. The analysis estimates a sensitivity of $\Phi_0 \approx 10^{-1}\,\mathrm{GeV}^{-1}\,\mathrm{m}^{-2}\,\mathrm{s}^{-1}$ for $E_0 = 1\,\mathrm{GeV}$ and $\gamma = 2.0$ for a 150 days period of data coming from Vela. We can compare this to the result of a recent study that reports a sensitivity of around $E^2\Phi_{\bar{\nu}_\mu+\nu_\mu} \approx 2 \times 10^{-8}\,\mathrm{GeV}\,\mathrm{cm}^{-2}\,\mathrm{s}^{-2}$ using a joined analysis of ARCA6-8-19-21 [60]. While it is not obvious from the publication, what reference energy was used for these models, we will assume $E_0 = 1\,\mathrm{TeV}$, according to the results from [13]. We can transfer this to our single flavor flux comparable to our result: $E^2\Phi_\nu = 1 \times 10^{-4}\,\mathrm{GeV}\,\mathrm{cm}^{-2}\,\mathrm{s}^{-2}$ which corresponds to a flux normalization of $\Phi_0 = 1 \times 10^2\,\mathrm{GeV}^{-1}\,\mathrm{cm}^{-2}\,\mathrm{s}^{-2}$ at $E_0 = 1\,\mathrm{GeV}$ and $\gamma = 2.0$. This shows, that the exploitation of a possible periodicity would improve the detection sensitivity for such point sources by three orders of magnitude. Transforming our result to a reference energy of 1 TeV and in the units used in most published results yields the following threshold flux for a 5σ detection of a periodic signal:

$$E^2\Phi_\nu(E_0 = 1\,\mathrm{TeV}) \approx 10^{-11}\,\mathrm{GeV}\,\mathrm{cm}^{-2}\,\mathrm{s}^{-1} \tag{4.1}$$

4.2 Crab and Vela Pulsar Predictions

In this section, the results using the bounded power law flux will be presented. The energy boundaries are taken from the predictions of [41] for the linear proton acceleration case. We will first have a look at the expected sensitivity using a 90 deg zenith angle threshold for Crab and Vela for two different maximum opening angles of the search cone. Figures 4.6 and 4.7 show the results for 30 deg

and 5 deg. Note that for the different sources, the same flux normalization does not represent the same flux, because the flux is normalized at the low energy boundary in each case (see section 3.6.2). For each source, the results have to be set in relation to the respective flux normalization estimated for the corresponding model in table 3.3. For the linear acceleration case investigated here, the predictions would be $\Phi_0^{\mathrm{crab,lin}} = 1 \times 10^{-13}\,\mathrm{GeV}^{-1}\,\mathrm{m}^{-2}\,\mathrm{s}^{-1}$ and $\Phi_0^{\mathrm{vela,lin}} = 8 \times 10^{-15}\,\mathrm{GeV}^{-1}\,\mathrm{m}^{-2}\,\mathrm{s}^{-1}$ at $\gamma = 2.0$.

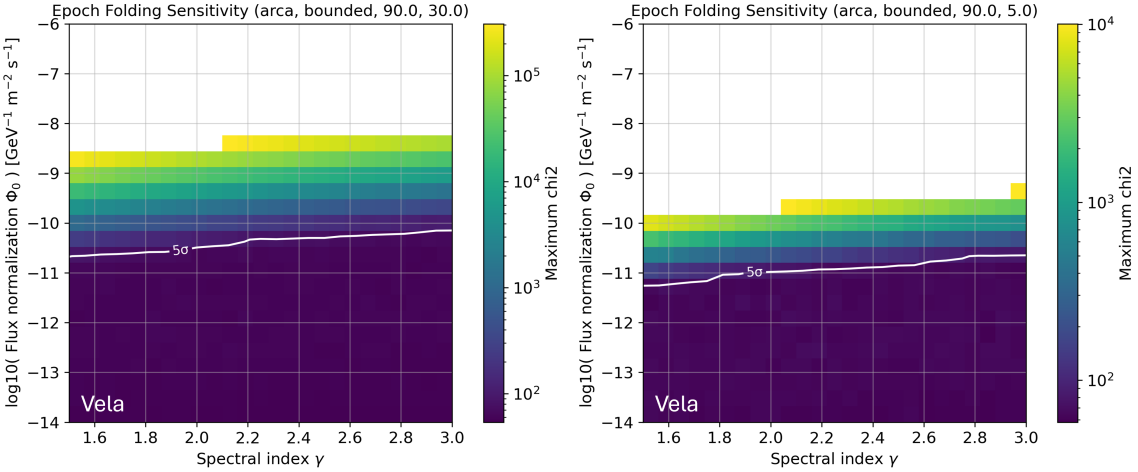

Figure 4.6: Epoch folding sensitivity for a bounded power law flux from Vela at ARCA with 90 deg zenith cut, 30 deg maximum search cone angle (left), 5 deg maximum search cone angle (right). Energy boundaries according to table 3.3

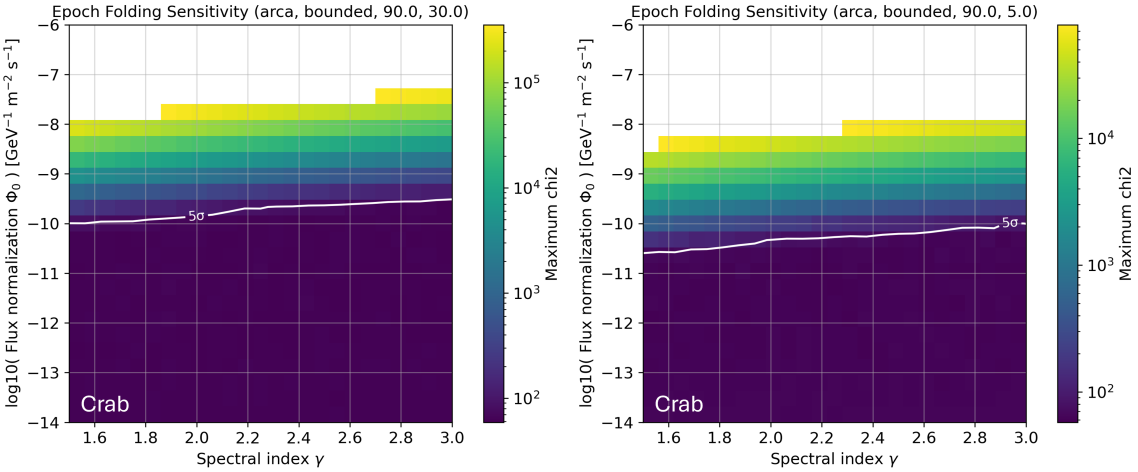

Figure 4.7: Epoch folding sensitivity for a bounded power law flux from Crab at ARCA with 90 deg zenith cut, 30 deg maximum search cone angle (left), 5 deg maximum search cone angle (right). Energy boundaries according to table 3.3

One can see that the influence arising from the spectral index is much lower than for the un-

bounded flux, which is expected simply from the way the flux models are defined. Analogously to the unbounded flux, we can see an improvement in sensitivity when choosing a lower maximum search cone angle, which lowers the flux normalization to still enable a 5σ detection down to $\Phi_0^{5\sigma,\mathrm{crab}} \approx 4 \times 10^{-11}\,\mathrm{GeV}^{-1}\,\mathrm{m}^{-2}\,\mathrm{s}^{-1}$ for Crab and $\Phi_0^{5\sigma,\mathrm{vela}} \approx 1 \times 10^{-11}\,\mathrm{GeV}^{-1}\,\mathrm{m}^{-2}\,\mathrm{s}^{-1}$. For the Crab nebula this means that the flux needed to be present in order to detect a periodic signal in the emission needed to be around 400 times the one that is predicted, whereas for Vela the minimum flux for the epoch folding analysis is about 1250 times the predicted one.

In order to estimate how the sensitivity is expected to develop when including more data, we can create subsets from our 150 day dataset and examine how this changes the epoch folding statistics. Each subset is created from the same timeseries, where the signal has already been injected. This means that all subsets have roughly the same signal to noise ratio, which allows us to extrapolate our current analysis. In figure 4.8 we see the resulting mean maximum χ^2 over the subset length in linear and double logarithmic scale. One can see how the epoch folding increases exponentially with

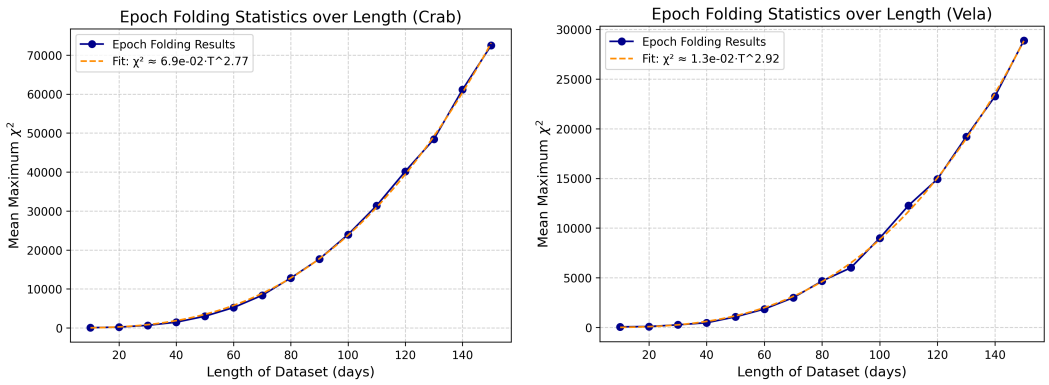

Figure 4.8: Epoch folding results for subsets of different lengths from Vela and Crab.

the length of the dataset for a given signal to noise ratio. This means that we can roughly scale our findings to longer observation times in order to estimate how this changes the sensitivity. The plots indicate that the expected epoch folding statistics follow roughly a powerlaw with $\chi^2 \propto T^\beta$, which is fitted to the data points. We see that the evolution differs for the chosen sources, which can probably be traced back to the different effective areas regarding detections of neutrinos originating from the two different positions in the sky. The following dependencies on the dataset length could be estimated:

$$\chi^2_{\mathrm{vela}} \approx 6.9 \times 10^{-2} \cdot L_{\mathrm{obs}}^{2.72} \tag{4.2}$$

$$\chi^2_{\mathrm{crab}} \approx 1.3 \times 10^{-2} \cdot L_{\mathrm{obs}}^{2.92} \tag{4.3}$$

We can now use the correlation between epoch folding statistics and length to estimate how long we needed to observe both sources in order to achieve a sensitivity that is low enough so that we would expect to detect the predicted neutrino flux if it is emitted periodically along with the pulsar's rotational period. We calculate the time that is needed to achieve a high enough sensitivity to detect each source based on the corresponding predicted $\chi^2(L_{\mathrm{obs}})$ evolution. Furthermore, we need to consider how the measured maximum χ^2 is expected to depend on the signal flux Φ_{pulse}. We can follow the assumption for the search of a periodic signal in a background dominated situation from [56], which is that the detection power scales with the squared signal amplitude. Since the flux of

detected events is proportional to the signal amplitude, we can assume that:

$$\chi^2 \propto \Phi^2_{\text{pulse}} \tag{4.4}$$

The flux Φ_{test} used to calculate the $\chi^2(L_{\text{obs}})$ evolution was sufficiently high to have a smooth evolution of data points to fit to. We know the exponential by which the χ^2 depends on the data set length L_{obs}, but we are now interested in how this actually scales for our predicted flux Φ_{pred}. To scale our result to an arbitrary flux, we can make use of the $\chi^2 \propto \Phi^2$ proportionality:

$$\chi^2(\Phi, L) = K \cdot L^{\alpha} \cdot \left(\frac{\Phi}{\Phi_{\text{test}}}\right)^2 \tag{4.5}$$

We have previously found the flux normalizations that lead to a 5σ detection over 150 days, meaning the corresponding $\chi^2(\Phi_{\text{th}}, L = 150\,\text{d}) = \chi^2_{\text{th}} = 87.3$ and can calculate the factor K_{th} for the detection threshold:

$$K_{\text{th}} = \frac{\chi^2_{\text{th}}}{(150\,\text{d})^{\alpha}} \cdot \left(\frac{\Phi_{\text{test}}}{\Phi_{\text{th}}}\right)^2 \tag{4.6}$$

Using this proportionality factor, we can state a simple estimation for the expected χ^2 over L_{obs} for an arbitrary flux.

$$\chi^2_{\text{th}} = K_{\text{th}} \cdot L^{\alpha}_{\text{th}} \cdot \left(\frac{\Phi_{\text{pred}}}{\Phi_{\text{test}}}\right)^2 = \chi^2_{\text{th}} \cdot \left(\frac{L_{\text{th}}}{150\,\text{d}}\right)^{\alpha} \cdot \left(\frac{\Phi_{\text{pred}}}{\Phi_{\text{test}}}\right)^2 \tag{4.7}$$

$$\Leftrightarrow L_{\text{th}} = 150\,\text{d} \cdot \left(\frac{\Phi_{\text{th}}}{\Phi_{\text{pred}}}\right)^{2/\alpha} = 150\,\text{d} \cdot R^{2/\alpha} \tag{4.8}$$

For our chosen sources we can now use the ratios between threshold sensitivity flux and predicted flux and the corresponding spectral index α we can estimate the threshold lengths L_{th} after which the predicted fluxes could be detected.

$$L_{\text{th,crab}} \approx 150\,\text{d} \cdot 400^{2/2.92} = 9085\,\text{d} \approx 25\,\text{y} \tag{4.9}$$

$$L_{\text{th,vela}} \approx 150\,\text{d} \cdot 1250^{2/2.77} = 25830\,\text{d} \approx 71\,\text{y} \tag{4.10}$$

This shows that the detection of the predicted signals via epoch folding is not really feasible with the used detector setup ARCA21. In the last section we will now try to summarize the main results of this work and try to give some thoughts on what this means for the future search for periodic cosmic neutrino sources with KM3NeT.

5 Summary and Outlook

This work can serve as a pathfinder to show that periodic neutrino emission from pulsars and X-ray binaries might provide a valuable insight into the extreme physics that is expected to take place in the close environment of these objects. In theory, the exceptional characteristics of neutrinos make it possible to probe these objects with striking precision, possibly revealing information about individual mechanisms that are possibly confined to a certain rotational phase. Aside from using neutrinos as probes to better understand the physics of pulsars, those objects are promising candidates for very high energy neutrino emission, due to their compactness, high rotational energy and the extreme environmental conditions that promote the high acceleration of hadrons and subsequent production of neutrinos. Detecting these neutrinos that reach energies exceeding those of our most advanced particle accelerators on Earth can offer a great opportunity to deepen the understanding about processes at the highest energy scales.

An analysis framework was developed that enables us to search for a possible periodic signal emitted by an arbitrarily chosen source object in the reconstructed data from both of KM3NeT's detectors. The frequency search is based on the epoch folding algorithm, a robust and efficient analysis method that is well established in pulsar astronomy. The phase folding can in theory provide a strong increase in background reduction and detection sensitivity for a signal that is periodically emitted. This works best for signals that are confined to a very narrow phase interval, which is expected to be the case in neutrino emission from pulsars.

Various preprocessing steps were implemented in the analysis chain, with the goal to extract the high level data from the KM3NeT data files and to create a timeseries of neutrino arrival times that are associated with the chosen source. A high level extraction module was built, to convert the KM3NeT data to a more astronomy friendly *astropy* oriented table-based format, which was integrated into the km3astro package. For both detectors ORCA and ARCA and for each reconstruction type (track/shower) the angular reconstruction uncertainty per reconstructed energy is calculated to be able to estimate each detected event's angular error and to connect the event selection process to this value, in order to exclude events with a high certainty of not originating from the chosen source. Furthermore, a track/shower classification based on paramPID was included, which was however only working correctly with older simulations and caused problems with the Monte-Carlo datasets in versions 9.0 and 9.2 that were used in this work. After the event selection process, data quality cuts and a timing correction are applied. This corrects the deviations in a periodic signal that arise from shifts in arrival times due to the movement of the Earth with respect to the selected source. The resulting series of arrival times is then analyzed via phase folding, using test frequencies around the known pulsation frequency that is observed in the electromagnetic emission.

To evaluate the sensitivity of this method, an existing periodic signal emission from a chosen source and the corresponding expected detector response was modeled. This allows us to study the behavior of the epoch folding analysis and to set upper limits on periodic neutrino fluxes. Two different types of fluxes were investigated: a classical power law flux $\Phi(E_\nu) = \Phi_0 \cdot E_\nu^{-\gamma}$ and a bounded power law flux, which is simply a power law flux that is only present between two energy boundaries E_{min} and E_{max}. The bounded flux model is used to evaluate the sensitivity to the detection of the fluxes from

the Crab and Vela pulsars as predicted by [41]. Generally, the inclusion of detections from ORCA did not show any significant improvement in the case of the investigated flux models. We find that the sensitivity to a generic power law flux is drastically improved compared to a time integrated point source analysis. However, simplifications and uncertainties in the modeling of the detector response have to be kept in mind and this result is to be taken with care. The investigations of the predicted bounded power law fluxes from Crab and Vela show that with the used ARCA21 setup, the search for cosmic neutrino sources seems not promising and an estimated observation time of 25 years for Crab and 71 years for Vela is needed to achieve a 5σ detection of predicted fluxes. This becomes even more critical when considering that these flux predictions might be strongly overestimated.

Nevertheless, this draws a somewhat promising picture of future research opportunities, once the KM3NeT detectors are completed. It is suggested that this analysis is redone when construction of ARCA has further progressed and more events, better angular and energy resolutions and more reliable event classification can be expected. Especially the results regarding the sensitivity to the predicted flux from Crab indicate a possibly interesting subject of analysis for IceCube. With its high effective area, suitable sky coverage for Crab and the long duration of ongoing measurements, IceCube might be able to detect the fluxes, if they are emitted periodically and with the predicted spectrum. A non-detection might shed new light onto how realistic these predictions are. Overall, the search for periodic neutrino emission is highly interesting and might provide a promising method for extracting cosmic neutrino detections from the huge atmospheric neutrino and even muon background. The ongoing construction of KM3NeT and the planned IceCube-Gen2 extension will further improve sensitivities and lift neutrino astronomy to new levels. The approach of combining multiple detectors and possibly including low-energy analyses that use single DOM responses could furthermore help to draw the bigger picture of possible periodic neutrino signals, paving the way to a promising future for neutrino astronomy.

Bibliography

[1] R. Abbasi et al. "Characterization of the astrophysical diffuse neutrino flux using starting track events in IceCube". In: *Physical Review D* 110.2 (July 2024). ISSN: 2470-0029. DOI: 10.1103/physrevd.110.022001. URL: http://dx.doi.org/10.1103/PhysRevD.110.022001.

[2] R. Abbasi et al. "Searches for periodic neutrino emission from binary systems with 22 and 40 strings of IceCube". In: *Astrophys. J.* 748 (2012), p. 118. DOI: 10.1088/0004-637X/748/2/118. arXiv: 1108.3023 [astro-ph.HE].

[3] Abdo Abdo et al. "Fermi Large Area Telescope Observations of the Crab Pulsar And Nebula". In: *The Astrophysical Journal* 708 (Dec. 2009), p. 1254. DOI: 10.1088/0004-637X/708/2/1254.

[4] M. Agostini et al. "Comprehensive measurement of pp-chain solar neutrinos". In: *Nature* 562.7728 (Oct. 1, 2018), pp. 505–510. ISSN: 1476-4687. DOI: 10.1038/s41586-018-0624-y. URL: https://doi.org/10.1038/s41586-018-0624-y.

[5] Gisela Anton. "Neutrino Telescopes". In: *Probing Particle Physics with Neutrino Telescopes*. WORLD SCIENTIFIC, Jan. 2020, 11–32. ISBN: 9789813275027. DOI: 10.1142/9789813275027_0002. URL: http://dx.doi.org/10.1142/9789813275027_0002.

[6] W. Baade and F. Zwicky. "Cosmic Rays from Super-Novae". In: *Proceedings of the National Academy of Sciences* 20.5 (1934), pp. 259–263. DOI: 10.1073/pnas.20.5.259. eprint: https://www.pnas.org/doi/pdf/10.1073/pnas.20.5.259. URL: https://www.pnas.org/doi/abs/10.1073/pnas.20.5.259.

[7] A. Bettini. "A Brief History of Neutrino". In: *The State of the Art of Neutrino Physics*. 2018. Chap. Chapter 1, pp. 1–36. DOI: 10.1142/9789813226098_0001. eprint: https://www.worldscientific.com/doi/pdf/10.1142/9789813226098_0001. URL: https://www.worldscientific.com/doi/abs/10.1142/9789813226098_0001.

[8] A. Bhadra and R. K. Dey. "TeV neutrinos and gamma-rays from pulsars". In: *Monthly Notices of the Royal Astronomical Society* 395.3 (May 2009), 1371–1375. ISSN: 1365-2966. DOI: 10.1111/j.1365-2966.2008.14345.x. URL: http://dx.doi.org/10.1111/j.1365-2966.2008.14345.x.

[9] Matthias Bissinger. "Observations of Be X-ray Binaries: Spin Period and Spectral Evolution". PhD thesis. Friedrich-Alexander-Universität Erlangen-Nürnberg, 2016.

[10] Bradley W. Carroll and Dale A. Ostlie. *An Introduction to Modern Astrophysics*. Ed. by San Francisco: Pearson Addison-Wesley. 2nd (International). 2007.

[11] Gaia collaboration. *Gaia DR3 Part 1. Main source*. DOI: https://doi.org/10.26093/cds/vizier.1355.

[12] The KM3NeT Collaboration. "Astronomy potential of KM3NeT/ARCA". In: *The European Physical Journal C* 84 (Sept. 2024). DOI: 10.1140/epjc/s10052-024-13137-2.

[13] The KM3NeT Collaboration. "Differential Sensitivity of the KM3NeT/ARCA detector to a diffuse neutrino flux and to point-like source emission: Exploring the case of the Starburst Galaxies". In: *Astroparticle Physics* 162 (2024), p. 102990. ISSN: 0927-6505. DOI: https://doi.org/10.1016/j.astropartphys.2024.102990. URL: https://www.sciencedirect.com/science/article/pii/S0927650524000677.

[14] The KM3NeT Collaboration. *km3astro*. https://git.km3net.de/km3py/km3astro. 2025.

[15] The KM3NeT Collaboration. *KM3NeT: Astroparticle physics with ARCA*. https://www.km3net.org/research/physics/astronomy-with-arca. Accessed: 2025-08-20. 2025.

[16] The KM3NeT Collaboration. *KM3NeT: Member Institutes*. https://www.km3net.org/about-km3net/collaboration/members. Accessed: 2025-08-20. 2025.

[17] The KM3NeT Collaboration. *KM3NeT: Particle physics with ORCA*. https://www.km3net.org/research/physics/particle-physics-with-orca. Accessed: 2025-08-20. 2025.
[18] The KM3NeT Collaboration. "Letter of intent for KM3NeT 2.0". In: *Journal of Physics G: Nuclear and Particle Physics* 43.8 (2016), p. 084001. DOI: 10.1088/0954-3899/43/8/084001.
[19] The KM3NeT Collaboration. "Observation of an ultra-high-energy cosmic neutrino with KM3NeT". In: *Nature* 638.8050 (2025). [Erratum: Nature 640, E3 (2025)], pp. 376–382. DOI: 10.1038/s41586-024-08543-1.
[20] The KM3NeT Collaboration. "The KM3NeT potential for the next core-collapse supernova observation with neutrinos: KM3NeT Collaboration". In: *The European Physical Journal C* 81.5 (May 2021). ISSN: 1434-6052. DOI: 10.1140/epjc/s10052-021-09187-5. URL: http://dx.doi.org/10.1140/epjc/s10052-021-09187-5.
[21] Wikipedia-User Cush. *Image of the Standard Model of Elementary Particles and Gravity*. https://en.m.wikipedia.org/wiki/File:Standard_Model_of_Elementary_Particles_and_Gravity.svg. Public domain. Accessed on 2025-07-24. 2023.
[22] Wolfgang Demtröder. *Experimentalphysik 4: Kern-, Teilchen- und Astrophysik*. 4th ed. Springer Berlin, Heidelberg, 2017. ISBN: 978-3-642-21476-9. DOI: 10.1007/978-3-642-21476-9. URL: https://link.springer.com/book/10.1007/978-3-642-21476-9.
[23] L. Ducci et al. *Ultra-luminous X-ray pulsars as sources of TeV neutrinos*. 2025. arXiv: 2508.10487 [astro-ph.HE]. URL: https://arxiv.org/abs/2508.10487.
[24] Thijs van Eeden. "Neutrino Astronomy with KM3NeT/ARCA". PhD thesis. University of Amsterdam, 2024.
[25] Maximilian Eff. "Search for low-energy periodic neutrino sources with ANTARES". MA thesis. Friedrich-Alexander-Universität Erlangen-Nürnberg, 2023.
[26] Anatoli Fedynitch et al. *Calculation of conventional and prompt lepton fluxes at very high energy*. 2015. arXiv: 1503.00544 [hep-ph]. URL: https://arxiv.org/abs/1503.00544.
[27] E. Fermi. "Versuch einer Theorie der beta-Strahlung. I." In: *Zeitrschrift für Physik* 88 (1934), pp. 161–177. DOI: 10.1007/BF01351864.
[28] J. A. Formaggio and G. P. Zeller. "From eV to EeV: Neutrino cross sections across energy scales". In: *Rev. Mod. Phys.* 84 (3 2012), pp. 1307–1341. DOI: 10.1103/RevModPhys.84.1307. URL: https://link.aps.org/doi/10.1103/RevModPhys.84.1307.
[29] Shanika Galaudage. *Astrophysics Image*. Personal collection of Shanika Galaudage. Image available via Google Photos. 2025. URL: https://photos.app.goo.gl/ogRAno3DMe4hWXq29 (visited on 08/18/2025).
[30] Rodrigo Gracia Ruiz and Maximilian Eff. "Search for periodic low energy neutrino sources with the ANTARES telescope". In: *PoS* ICRC2023 (2023), p. 1011. DOI: 10.22323/1.444.1011.
[31] Claus Grupen. *Astroparticle Physics*. Undergraduate Texts in Physics. Springer, 2020. ISBN: 978-3-030-27341-5, 978-3-030-27339-2. DOI: 10.1007/978-3-030-27339-2.
[32] Steffen Hallmann. "Sensitivity to atmospheric tau-neutrino appearance and all-flavour search for neutrinos from the Fermi Bubbles with the deep-sea telescopes KM3NeT/ORCA and ANTARES". PhD thesis. Friedrich-Alexander-Universität Erlangen-Nürnberg, 2021.
[33] F. Halzen. "High-Energy Astrophysical Neutrinos". In: *The State of the Art of Neutrino Physics*. 2018. Chap. Chapter 9, pp. 325–390. DOI: 10.1142/9789813226098_0009. eprint: https://www.worldscientific.com/doi/pdf/10.1142/9789813226098_0009. URL: https://www.worldscientific.com/doi/abs/10.1142/9789813226098_0009.
[34] Francis Halzen and Ali Kheirandish. "Chapter 5: IceCube and High-Energy Cosmic Neutrinos". In: *The Encyclopedia of Cosmology*. Ed. by Giovanni G. Fazi. 2023, pp. 107–235. DOI: 10.1142/9789811282645_0005. arXiv: 2202.00694 [astro-ph.HE].

[35] M. Honda et al. "Calculation of atmospheric neutrino flux using the interaction model calibrated with atmospheric muon data". In: *Phys. Rev. D* 75 (4 2007), p. 043006. DOI: 10.1103/PhysRevD.75.043006. URL: https://link.aps.org/doi/10.1103/PhysRevD.75.043006.

[36] Daniela Huppenkothen et al. "Stingray: A Modern Python Library for Spectral Timing". In: *The Astrophysical Journal* 881.1 (2019), p. 39. DOI: 10.3847/1538-4357/ab258d. URL: https://dx.doi.org/10.3847/1538-4357/ab258d.

[37] John David Jackson. *Classical electrodynamics*. 3rd ed. New York, NY: Wiley, 1999. ISBN: 9780471309321. URL: http://cdsweb.cern.ch/record/490457.

[38] Peter A. Jenke. *Vela X-1*. 2025. URL: https://gammaray.nsstc.nasa.gov/gbm/science/pulsars/lightcurves/velax1.html (visited on 08/26/2025).

[39] Katharina Jurk. *Research Project: Periodic Low Energy Neutrino Search in a High Energy Neutrino Detector*. 2024. URL: https://ecap.nat.fau.de/wp-content/uploads/2024/05/2024-04_KatharinaJurk_RP_PeriodicNeutrinoSources.pdf.

[40] Dong Lai. "Physics of Neutron Star Kicks". In: *Stellar Astrophysics*. Springer Netherlands, 2000, 127–136. ISBN: 9789401008785. DOI: 10.1007/978-94-010-0878-5_15. URL: http://dx.doi.org/10.1007/978-94-010-0878-5_15.

[41] Bennett Link and Fiorella Burgio. "Flux predictions of high-energy neutrinos from pulsars: High-energy neutrinos from pulsars". In: *Monthly Notices of the Royal Astronomical Society* 371.1 (Aug. 2006), 375–379. ISSN: 1365-2966. DOI: 10.1111/j.1365-2966.2006.10665.x. URL: http://dx.doi.org/10.1111/j.1365-2966.2006.10665.x.

[42] Bennett Link and Fiorella Burgio. "TeV μ Neutrinos from Young Neutron Stars". In: *Phys. Rev. Lett.* 94 (18 2005), p. 181101. DOI: 10.1103/PhysRevLett.94.181101. URL: https://link.aps.org/doi/10.1103/PhysRevLett.94.181101.

[43] Andrew Lyne, Francis Graham-Smith, and Benjamin Stappers. *Pulsar Astronomy*. 5th ed. Cambridge Astrophysics. Cambridge University Press, 2022.

[44] Robert Mann. *An Introduction to Particle Physics and the Standard Model*. CRC Press, 2010. ISBN: 978-1-4200-8300-2. DOI: 10.1201/9781420083002.

[45] Alexander A. Mushtukov et al. "Ultraluminous X-ray sources as neutrino pulsars". In: 476.3 (May 2018), pp. 2867–2873. DOI: 10.1093/mnras/sty379. arXiv: 1801.04810 [astro-ph.HE].

[46] Lothar Oberauer and Judith Oberauer. *Neutrinophysik: Grundlagen, Experimente und aktuelle Forschung*. Jan. 2019. ISBN: 978-3-662-59334-9. DOI: 10.1007/978-3-662-59335-6.

[47] K. Okumura. "Atmospheric Neutrinos". In: *The State of the Art of Neutrino Physics*. 2018. Chap. Chapter 5, pp. 211–235. DOI: 10.1142/9789813226098_0005. eprint: https://www.worldscientific.com/doi/pdf/10.1142/9789813226098_0005. URL: https://www.worldscientific.com/doi/abs/10.1142/9789813226098_0005.

[48] M. A. C. Perryman et al. "The HIPPARCOS Catalogue". In: 323 (July 1997), pp. L49–L52.

[49] E. Richard et al. "Measurements of the atmospheric neutrino flux by Super-Kamiokande: Energy spectra, geomagnetic effects, and solar modulation". In: *Phys. Rev. D* 94 (5 2016), p. 052001. DOI: 10.1103/PhysRevD.94.052001. URL: https://link.aps.org/doi/10.1103/PhysRevD.94.052001.

[50] Jürgen Schaffner-Bielich. *White Dwarfs*. Cambridge University Press, 2020. DOI: 10.1017/9781316848357.

[51] K. Scholberg. "Neutrinos from Supernovae and Other Astrophysical Sources". In: *The State of the Art of Neutrino Physics*. 2018. Chap. Chapter 8, pp. 299–324. DOI: 10.1142/9789813226098_0008. eprint: https://www.worldscientific.com/doi/pdf/10.1142/9789813226098_0008. URL: https://www.worldscientific.com/doi/abs/10.1142/9789813226098_0008.

[52] A. Y. Smirnov. "Solar Neutrinos and Matter Effects". In: *The State of the Art of Neutrino Physics*. 2018. Chap. Chapter 4, pp. 149–209. DOI: 10.1142/9789813226098_0004. eprint:

https://www.worldscientific.com/doi/pdf/10.1142/9789813226098_0004. URL: https://www.worldscientific.com/doi/abs/10.1142/9789813226098_0004.

[53] Maurizio Spurio. *Probes of Multimessenger Astrophysics. Charged cosmic rays, neutrinos, γ-rays and gravitational waves*. Astronomy and Astrophysics Library. Springer, 2018. ISBN: 978-3-319-96853-7, 978-3-319-96854-4. DOI: 10.1007/978-3-319-96854-4.

[54] *Timing analysis*. https://imagine.gsfc.nasa.gov/science/toolbox/timing2.html. Imagine the Universe! Astronomer's Toolbox – Timing analysis. NASA Goddard Space Flight Center. 2025. URL: https://imagine.gsfc.nasa.gov/science/toolbox/timing2.html.

[55] Albrecht Unsoeld and Bodo Baschek. "The new cosmos : an introduction to astronomy and astrophysics". In: *The new cosmos : an introduction to astronomy and astrophysics, 5th ed. Berlin: Springer, 2001, xiv, 557 p. Translated by William D. Brewer, ISBN 3540678778* (Jan. 2001).

[56] Anthony D. Whalen. *Detection of Signals in Noise, 2nd Edition*. San Diego: Academic Press, 1995. ISBN: 978-0127462756.

[57] Creative Commons Wikipedia. *Crab Nebula in Multiple Wavelengths*. https://commons.wikimedia.org/wiki/File:Crab_Nebula_in_Multiple_Wavelengths.png. Composite created by Huntster. Licensed under CC BY-SA 3.0. Accessed on 2025-07-07. 2015.

[58] Zi-Zhuo Xiao, Gang Guo, and Tuohuniyazi Tuniyazi. *Exploring the properties of newborn pulsars with high-energy neutrinos*. 2025. arXiv: 2507.16551 [astro-ph.HE]. URL: https://arxiv.org/abs/2507.16551.

[59] Nicolas Yunes, M. Coleman Miller, and Kent Yagi. "Gravitational-wave and X-ray probes of the neutron star equation of state". In: *Nature Rev. Phys.* 4.4 (2022), pp. 237–246. DOI: 10.1038/s42254-022-00420-y. arXiv: 2202.04117 [gr-qc].

[60] Sandra Zavatarelli et al. "The search for point-like neutrino sources with ANTARES and KM3NeT-ARCA telescopes". In: *EPJ Web of Conferences* 319 (Mar. 2025). DOI: 10.1051/epjconf/202531906010.

[61] Wenjun Zhang. "p-value based statistical significance tests: Concepts, misuses, critiques, solutions and beyond". In: 12 (May 2022), pp. 80–122.

[62] Kai Zuber. "Neutrino Physics". In: Taylor Francis, 2020. ISBN: 9781351764582, 9781315195612, 9781032242200, 9781138718890. DOI: 10.1201/9781315195612. URL: https://directory.doabooks.org/handle/20.500.12854/79366.

Eigenständigkeitserklärung

Hiermit bestätige ich, dass ich diese Arbeit selbstständig und nur unter Verwendung der angegebenen Hilfsmittel angefertigt habe.

Erlangen den 28.08.2025

Hannes Warnhofer